INVESTIGATION OF A SEGMENTED PLANE SOLAR ENERGY CONCENTRATOR

A THESIS

Presented to

The Faculty of the Division of Graduate Studies and Research

By

Allan Michael Lindsey

In Partial Fulfillment

of the Requirements for the Degree

Master of Science in Mechanical Engineering

Georgia Institute of Technology

August, 1974

INVESTIGATION OF A SEGMENTED PLANE SOLAR ENERGY CONCENTRATOR

Approved:

P. V. Desai, Chairman

P. V. Kadaba

S. Hanagud

Date approved by Chairman: 7/11/74

ACKNOWLEDGMENTS

I am extremely grateful to my advisor, Dr. P. V. Desai, whose interest and positive attitude have been extremely valuable in the accomplishment of this work. I am also grateful to Dr. P. V. Kadaba, a member of the thesis committee, for his frequent encouragement and helpful suggestions; and to Dr. S. Hanagud, also a member of the thesis committee, for his interest and valuable comments.

I wish to thank each member of the technical and secretarial staff of the School of Mechanical Engineering for their willingness to help whenever needed. Special thanks are offered to Messrs. L. A. Cavalli, A. C. Josey, and George Halstead, for their patience, interest, and valuable assistance in fabricating much of the experimental apparatus; and to Messrs. Cliff Bannister, Gene Clopton, Jerry Tinkham, and Donald Cabe and the student assistants for their ready assistance on numerous occasions.

I am indebted to William C. Johnston of the Warren Dual Jet Division of Kysor Industrial Corporation for his helpful suggestions and valuable support.

Finally, I am most grateful to my family for their support in this and every undertaking; and to Nereida, whose love and encouragement have accompanied me in my every effort.

TABLE OF CONTENTS

Chapter Page

LIST OF TABLES

Table | Page

LIST OF ILLUSTRATIONS

Figure Page

Figure Page

NOMENCLATURE*

θ	angle between the vertical normal and a component of a solar flux line perpendicular to the east-west axis (see page 76)
β	solar altitude
α_s	south solar azimuth
$\dot{m}$	mass flowrate of heat transfer fluid
A_c	total concentrator surface area, including the area between segments
C_p	specific heat of heat transfer fluid
G	geometric ratio (see page 38)
I_D	direct radiation intensity
I_{DN}	direct normal radiation intensity
O_r	optical ratio (see page 38)
$\dot{Q}_{in}$	energy input to system ($I_D \times A_c$)
$\dot{Q}_{out}$	energy output of system $[\dot{m} \cdot C_p (T_o - T_i)]$
R	reflective ratio (see page 38)
T_a	ambient temperature
T_i	inlet temperature of heat transfer fluid
T_o	outlet temperature of heat transfer fluid
ΔT	$(T_o - T_a)$

*Symbols not listed are defined in the particular section in which they occur.

SUMMARY

The segmented plane solar energy concentrator design utilizes an array of long flat reflective segments, the centerlines of which are parallel and lie in a common plane. Initially, the concentrator is focused by orienting each segment so that all incident solar energy is reflected onto a common linear receiver. Thereafter, tracking is accomplished by equally rotating all segments by an amount proportional to the change in the sun's position. The simple surface geometry, and the fact that the concentrator does not have to rotate about its focal line are primary advantages of the segmented plane design.

The purpose of this work is to establish a quantitative evaluation of a segmented plane concentrator to determine the applicability of the working principle, and to gain insight into the design of all solar energy conversion devices. This objective is accomplished by constructing a segmented plane concentrator with twenty five square feet of primary surface area, and by testing it with various receiver configurations by heating a fluid under conditions typical of practical applications.

This work demonstrates that it is feasible to economically fabricate a segmented plane concentrator that will efficiently concentrate incident solar radiation. It

is also shown that of the various receivers tested in the range of temperatures suitable for applications such as residential heating, the receiver composed of a copper pipe coated with a carbon black paint and surrounded by a clear acrylic tube performs most efficiently.

The procedure developed for analyzing the data of this work makes it possible to predict the performance of the experimental concentrator-receiver systems at any time of the day throughout the year for various fluid and ambient temperatures. This study also provides a convenient means for estimating values of direct normal solar radiation intensity for Atlanta, Georgia, on clear days.

CHAPTER I

INTRODUCTION

The Need for Energy Research

It is understandable that man first chose wood, fossil fuels, and hydroelectric potential to meet his energy requirements since these resources were available in large quantities, were easily utilized, and were reasonably accessible. As more and more energy was consumed, however, these resources became far less accessible, even though adequate quantities still existed. To further complicate matters, the demand for energy resources grew dramatically. Because of the diminishing accessibility of these initial energy resources, and the ever-increasing demand for energy, by the middle of the twentieth century it was obvious that additional sources of energy had to be identified and utilized if future energy demands were to be met.

Though the search for additional energy sources is underway, ultimately, fossil fuels must be completely replaced as an energy resource. One of the main reasons is well expressed by a statement published in 1969 by the Committee on Resources and Man[1] based on their study of the ultimate world production of energy from natural gas liquids, natural gas, crude oil, tar sands, oil shale, and coal. They

state:

> Since the earth's deposits of fossil fuels are finite in amount and non-renewable during periods of less than millions of years, it follows that energy from this source can be obtained for only a limited period of time. It is estimated that the earth's coal supplies are sufficient to serve as a major source of industrial energy for two or three (more) centuries. The corresponding period for petroleum, both because of its smaller initial supply and because of its more rapid rate of consumption, is only 70-80 years.

Further, we cannot afford to consume all available petroleum as a fuel because vital substances such as plastics, synthetic rubber, lubricants, and various chemicals are all derived from petroleum. Therefore, fossil fuels must be replaced as an energy source well before they are completely exhausted.

So far, numerous sources of energy potential have been recognized. The more prominent among these are: energy from nuclear reactions, energy from the sun, energy from the heat contained within the earth called geothermal energy, energy from the temperature differential across the ocean depth, energy from the wind, and energy from the ocean tides. It is logical that all possible sources should be thoroughly studied and that the most practical combinations of these be used to meet future energy demands based on their availability, accessibility, cost of conversion, and potential detriment to man and his environment.

The Sun As An Energy Resource

One need only consider the food he eats, the clothes

he wears, and the fuels he consumes to realize that man has always been dependent upon nature's ability to utilize solar energy in the production of organic matter through photosynthesis. In addition to the natural utilization of solar energy, man can construct devices which collect solar energy and convert it into other forms of useful energy. One of the advantages of utilizing solar radiation as an energy resource is that, for all practical purposes, the sun can be considered as an inexhaustible source which transmits enormous quantities of energy to the earth's surface. Another advantage is that extensive harnessing of solar energy would probably pose no serious threat to the environment.[2] One of the main disadvantages is that, due to the low energy density of the solar flux, large collector facilities are required to produce moderate quantities of energy, and thus the initial and operating costs are high. Also, the amount of solar energy available at any point on the earth's surface is restricted to daylight hours and is limited by atmospheric conditions. This point is especially relevant because solar energy cannot be conveniently stored for use during such periods.

Survey of Solar Energy Applications

The purpose of this section is to provide an overview of past, present, and proposed solar energy applications in order to lend better perspective to this work. This is

accomplished by citing examples of four categories of solar energy applications.

Utilization of Natural Processes

Recently, the Joint Solar Energy Panel of the National Science Foundation and The National Aeronautics and Space Administration[2] theorized that substantial energy supplies could be derived by cultivating and harvesting large quantities of organic matter. According to their theory, this growth would then be combined with organic wastes from cities to be used directly, or converted into gaseous and liquid fuels for subsequent use. They further state that commercial power production from combustion of urban wastes is already practiced in certain areas, primarily Europe; that many enterprises such as the lumber industry produce much of the power they consume by combustion of their industrial wastes; and that animal wastes are used by several countries to satisfy part of their energy requirements.

Devices for Direct Absorption

Devices which utilize direct absorption of solar energy for distillation of sea water have been widely investigated. The United States Department of the Interior[3], for instance, has sponsored considerable research on solar stills.

Many applications which utilize absorption of solar radiation, depend on a device referred to as a flat plate collector. These collectors consist of a plate oriented

toward the sun and coated so as to absorb as much of the solar energy as possible. The heat so absorbed is then transferred to a fluid which is circulated through the collector. O'neill, McDonald, and Sims[4] present a good discussion of the design of flat plate collectors using the latest technology. Flat plate collectors can be utilized in absorption refrigeration systems[5] and domestic heat pumps,[6] for example.

Photovoltaic Devices

Photovoltaic devices, often called solar cells, are well known for their use in powering earth satellites. A review of the types of solar cell arrays used in communications satellites is presented in a recent volume of Proceedings of the IEEE.[7] Though solar cells are very expensive and relatively inefficient, continued improvement in their technology could conceivably lead to their widespread use for terrestrial applications. Berman[8], among several others, has investigated the design of solar cells for terrestrial uses.

An interesting proposed application is to place satellites in stationary orbit above the earth with giant arrays of photovoltaic cells to generate large quantities of electricity. This electricity would then be converted and transported to earth via microwave transmission, where it would be converted back to electrical energy for normal consumption. This proposal presents many technical challenges,

such as transportation of satellite components into orbit, assembly of components while in orbit, control of the motion of the satellite, and the cooling of conductors, conversion equipment, and transmitting devices. However, it has many advantages such as not requiring extensive land areas, not being affected by atmospheric conditions, and being able to function almost continually, even during hours of darkness on the earth below. Because of these advantages, this proposal has received considerable attention in the literature.[9]

Devices Utilizing Solar Energy Concentrators

The intensity of the solar flux at the earth's surface is adequate for numerous applications. However, for other applications it is necessary to concentrate the solar flux before it can be utilized. Concentrating devices can be divided into two categories based on whether they produce a point or a linear focus. The two classifications are considered separately in the following sections.

Concentrators with a Point Focus. Perhaps the most explored and most practical of all solar applications is that of solar furnaces. Extremely high temperatures can be obtained with these devices, which usually utilize a parabolic shaped concentrator. Trombe[10] discusses the various applications of solar furnaces for high temperature research and manufacturing, and describes the 1000 kw solar furnace built at Montlouis, France.

Another device which lends itself to the use of a point

focusing concentrator is the heat engine.[11] These devices have been considered for applications in both space and terrestrial technology.

Hildebrandt, Haas, Jenkins, and Colaco[12] have proposed a large terrestrial solar power plant that would essentially utilize a point focus. In their proposal, a field 1.8 kilometers in diameter would be filled with individual reflectors, each about three to five square meters in area, which could be independently oriented so as to reflect incident radiation onto a receiver at the top of a 450 meter tower. The energy so concentrated would serve as the heat source for either a magnetohydrodynamic generator or for generating steam to drive turbine generators at ground level.

Concentrating Devices with Linear Foci. Dr. C. G. Abbot, famous for his work in solar energy research, designed and constructed numeous conversion devices. Among the better known of these is a small cylindrical parabolic concentrator.[13] This concentrator has a reflector that is about six feet long and two feet wide. The receiver is constructed of two concentric pyrex tubes with the space between maintained at a high vacuum. Through the center tube runs a heat transfer fluid in which lampblack is suspended to absorb the incident radiation.

In 1913, Shuman and Boys[14] built a large solar steam generating plant on the banks of the Nile River near Meadi, Egypt. The steam was used to power a pump which irrigated

adjacent arid land. Their system was composed of seven cylindrical parabolic concentrators, each 14 feet wide and 250 feet long, and developed 50 to 60 horsepower.

In 1963, the University of Marseilles constructed a solar boiler composed of seven cylindrical parabolic concentrators, each one meter wide and eight meters long, all having a common receiver.[15] Tracking was accomplished by actuation of a linkage system which then pivoted each parabolic concentrator as required.

An interesting type of linearly focusing refractive concentrator is being developed and has already demonstrated experimental success.[16] The refractor is an extruded plastic plate, flat on the side facing the sun, and shaped on the other side to form parallel flat strips. The pitch of each strip is such that the light passing through it is directed onto a common receiver below. Tracking is accomplished by lateral translation of the receiver.

Definition of the Problem

As previously mentioned, many applications of solar energy require that the flux be concentrated before it can be efficiently utilized. The concentration required for most solar energy applications is best accomplished with devices which have a linear focus. The linearly focusing devices which have received the most consideration utilize the cylindrical parabolic design. A typical cylindrical

parabolic concentrator is shown in the top sketch of Figure 1. A simple single pass receiver is shown centered on the focal line. Tracking is accomplished by rotating the entire concentrator about the focal line. The cylindrical parabolic concentrator has several significant drawbacks. First, it is difficult to economically manufacture the parabolic geometry. Secondly, although it is not difficult to track the sun with a small parabolic concentrator, it becomes more difficult as the size of the concentrator increases.

This research investigates a linearly focusing concentrator which accomplishes tracking without rotating the entire concentrator about its focal line, and which concentrates the solar flux via economical flat reflective surfaces. This concentrator is shown in the bottom sketch of Figure 1, and is called a segmented plane solar concentrator because it is composed of flat reflective segments whose axes lie in a common plane. Initial focusing is accomplished by orienting each segment so that its reflected image is incident upon the receiver. As explained in Appendix A, which details several geometric relationships relative to this work, tracking is accomplished after an initial focusing by rotating all segments equally about their axes. The principle of the segmented plane concentrator was apparently first conceived by Carl Guntner[17] in 1906 as an efficient means of producing steam for industrial applications. However, a literature search has revealed no evidence that

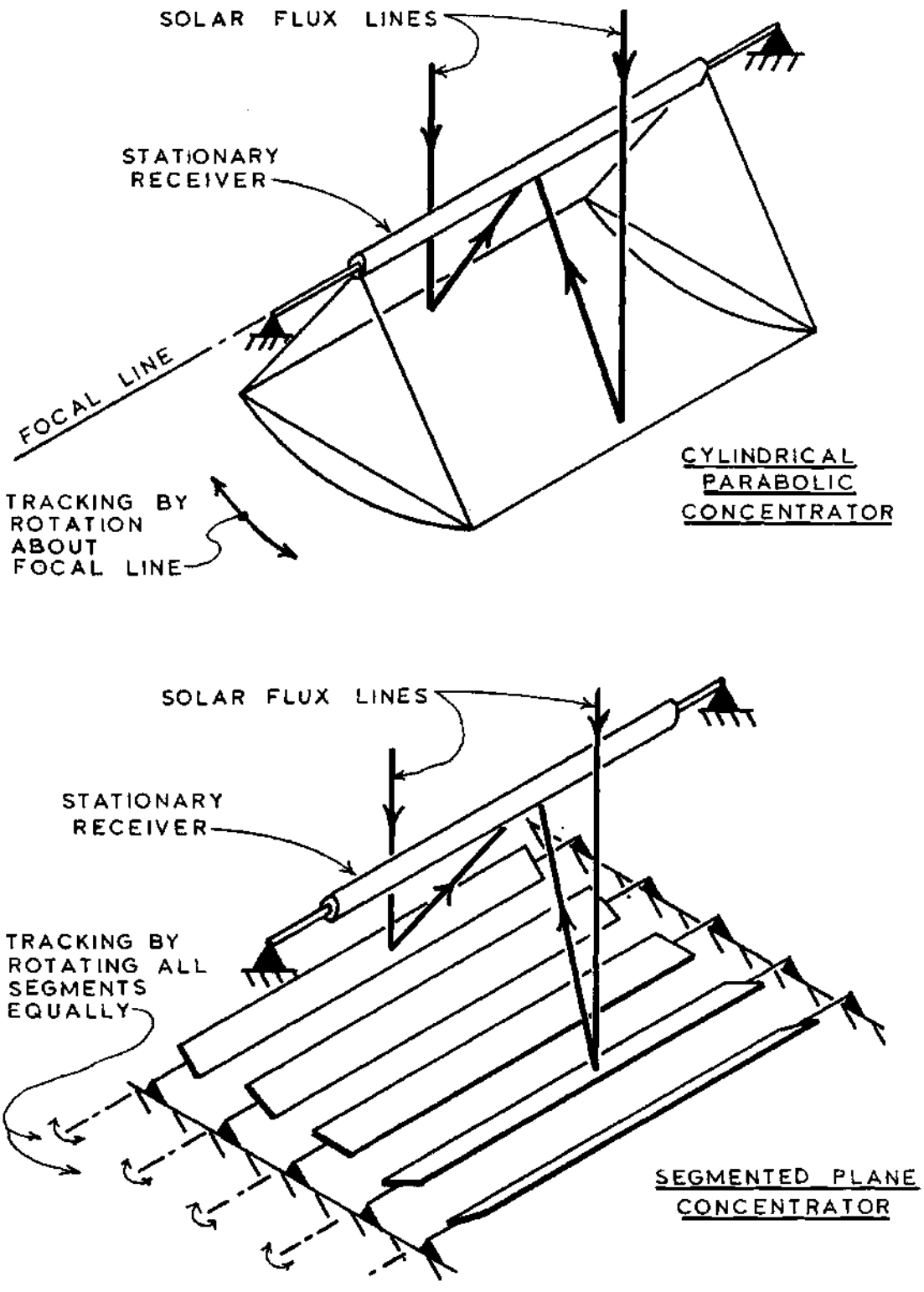

Figure 1. Comparison of Cylindrical Parabolic and Segmented Plane Concentrators

anyone has ever quantitatively evaluated his proposal.

Objective and Basic Approach

The object of this work is to establish a quantitative evaluation of the performance of a segmented plane solar concentrator to determine the practicality of the working principle, and to gain insight into the design of solar devices in general. To achieve this objective, a segmented plane concentrator is constructed using simple materials and fabrication techniques. It is then tested as a system with various receiver configurations by heating a fluid under flow conditions typical of practical applications.

CHAPTER II

DESIGN OF THE EXPERIMENTAL CONCENTRATOR AND RECEIVERS

Initial Concentrator Design

The initial design was dependent upon the size of the concentrator required, the desired concentration ratio, and the orientation of the concentrator. These parameters in turn dictated the segment and tracking mechanism requirements.

A concentrator with sufficient reflective surface area to produce a measurable flow of heat transfer fluid over the temperature range of this program was necessary. A reflective area of 25 square feet, which would produce a nominal thermal output of one kilowatt, was selected to satisfy this requirement since that size would also meet economic and portability limitations.

For the segmented plane concentrator, the concentration ratio is a function of the segment width, the spacing between segments, and the overall width of the concentrator. Since solar concentrators are generally used for high temperature applications, and because the basic approach of this program was to examine conditions typical of actual applications, the concentration ratio was to be made as high as practically possible consistent with the materials available.

Because of its availability, highly polished stainless

steel was selected as the reflective surface material. The stainless steel selected required flexural and torsional support to prevent distortion of the projected image when the segments were supported and pivoted from their ends. One inch square steel tubing was selected for the support because it would allow a narrow segment width and because it would provide the required strength at a minimum cost. A suitable segment width and spacing between segments had to be selected to provide adequate clearance during rotation of the segments, to permit a high concentration ratio, and to allow a high area efficiency. The term area efficiency refers to the ratio of the total reflective surface area to the total concentrator area including the spaces between segments. A simple graphical analysis demonstrated the desirability of a segment width of 1-1/2 inches and 3/16 inch spacing between segments, which would yield an area efficiency of 88 percent.

The design of the tracking mechanism was a function of the maximum segment rotation required. The amount of rotation, in turn, was dependent upon the concentrator orientation (north to south or east to west). The analysis presented in Appendix A showed that less segment rotation would be required with east to west than with north to south orientation. On the other hand, the analysis also showed that with east to west orientation, the sun's motion would cause the composite image to travel more along the axis of

the receiver than would occur with north to south orientation. However, for the purpose of evaluating the concentrator, the travel of the image could be compensated for by having a receiver that could be moved along its centerline. Therefore, the east to west orientation was selected.

For economic reasons a four bar parallel linkage system was chosen to accomplish the equal rotation of the segments during tracking. Figure 2 describes the linkage system design. The slot in the pivot pins was located so that rotation of the segments would take place about the centerlines of the reflective surfaces. The locking nuts shown for each segment were to be loosened while focusing, and then tightened for tracking. As is demonstrated in Appendix A, tracking is accomplished by rotating all segments by one half the change in θ, the angle formed by a vertical normal and the component of the solar flux normal to the axis of the concentrator. Figure 20 of Appendix A shows that between the hours of 9 a.m. and 3 p.m. solar time, θ varies over only a 65 degree range throughout the year. The linkage system thus had to provide for only 33 degrees of segment rotation. The scale drawing of Figure 3 indicated that 1/2 inch diameter holes in the tracking bar would allow the required rotation for the size of the components shown.

The Prototype

A small prototype consisting of ten reflective

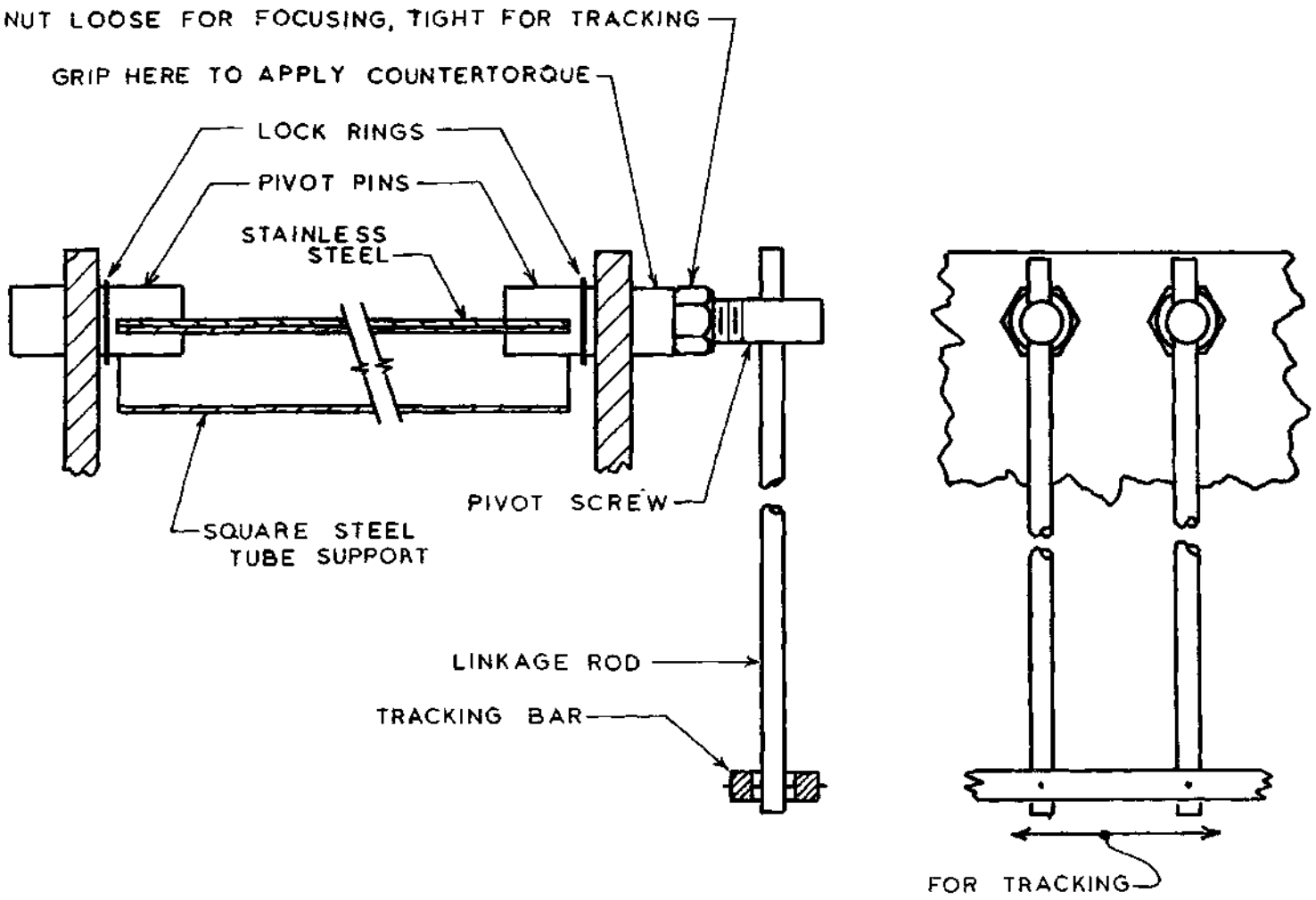

Figure 2. Focusing and Tracking Mechanism

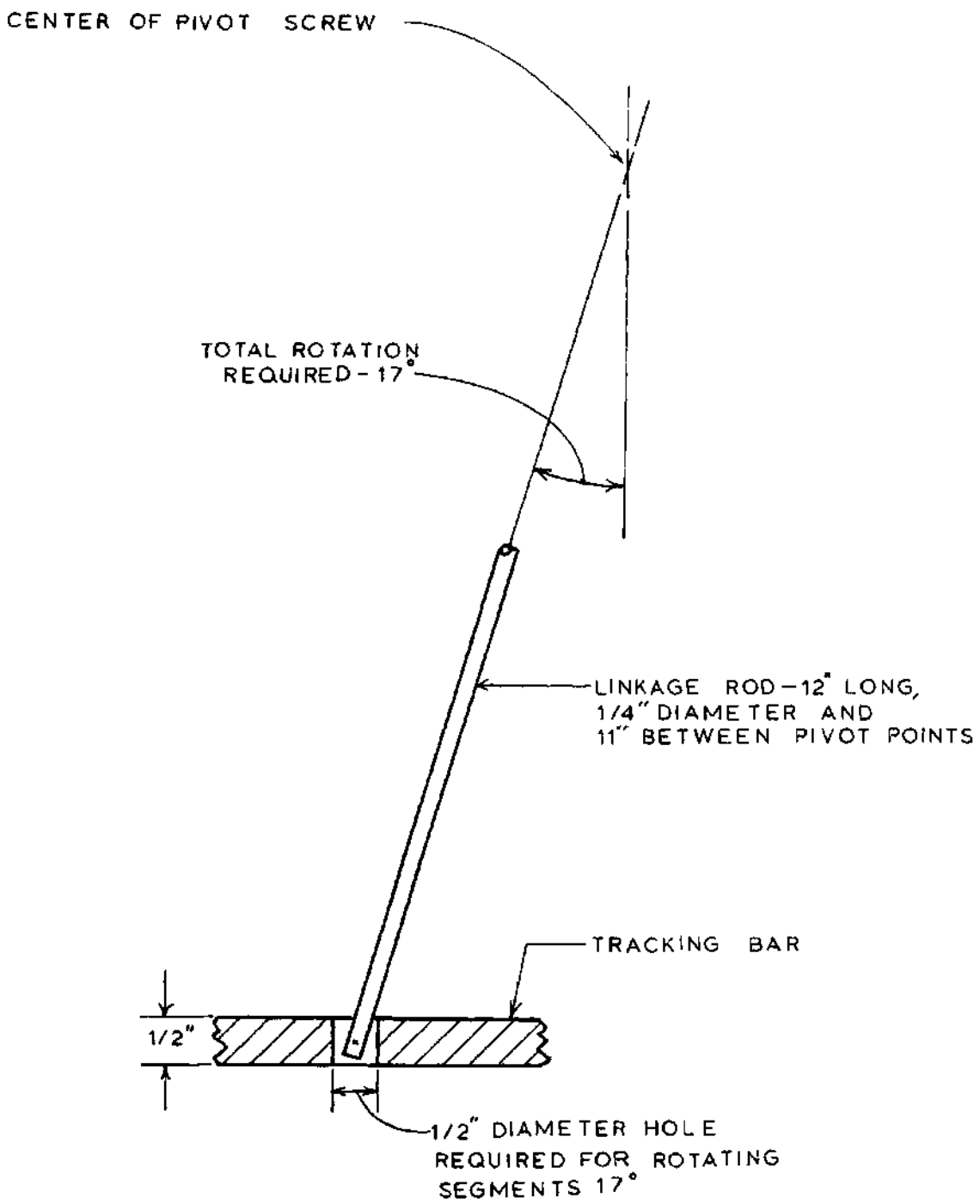

Figure 3. Tracking Bar Design

segments, 1-1/2 inches wide, 42 inches long, and spaced 3/16 inch apart was constructed to evaluate the initial design. Preliminary tests with the prototype indicated that due to the nonlinearity of the reflective segments, only about 80 percent of the composite image was incident upon a two inch diameter receiver. To obviate this inefficiency, the fabrication procedure illustrated in Figure 4 was adopted. Following this procedure, the reflective side of the stainless steel was placed against the way of a long lathe bed and was clamped against the way through small aluminum channels which held the stainless steel evenly against the way. Epoxy was applied to the steel tube which was in turn placed onto the stainless steel without any pressure. Once the epoxy cured, the stainless steel retained the shape of the flat way instead of the irregular square tube. With the improved design, all of the composite image was incident upon the 2 inch diameter receiver.

Initially, there was excessive clearance where the linkage rods passed through the pivot screws which prevented simultaneous rotation of the segments. A setscrew added to the side of each pivot screw to firmly hold the linkage rods eliminated this problem. In addition to this, the full scale concentrator linkage components were to be machined to closer tolerances.

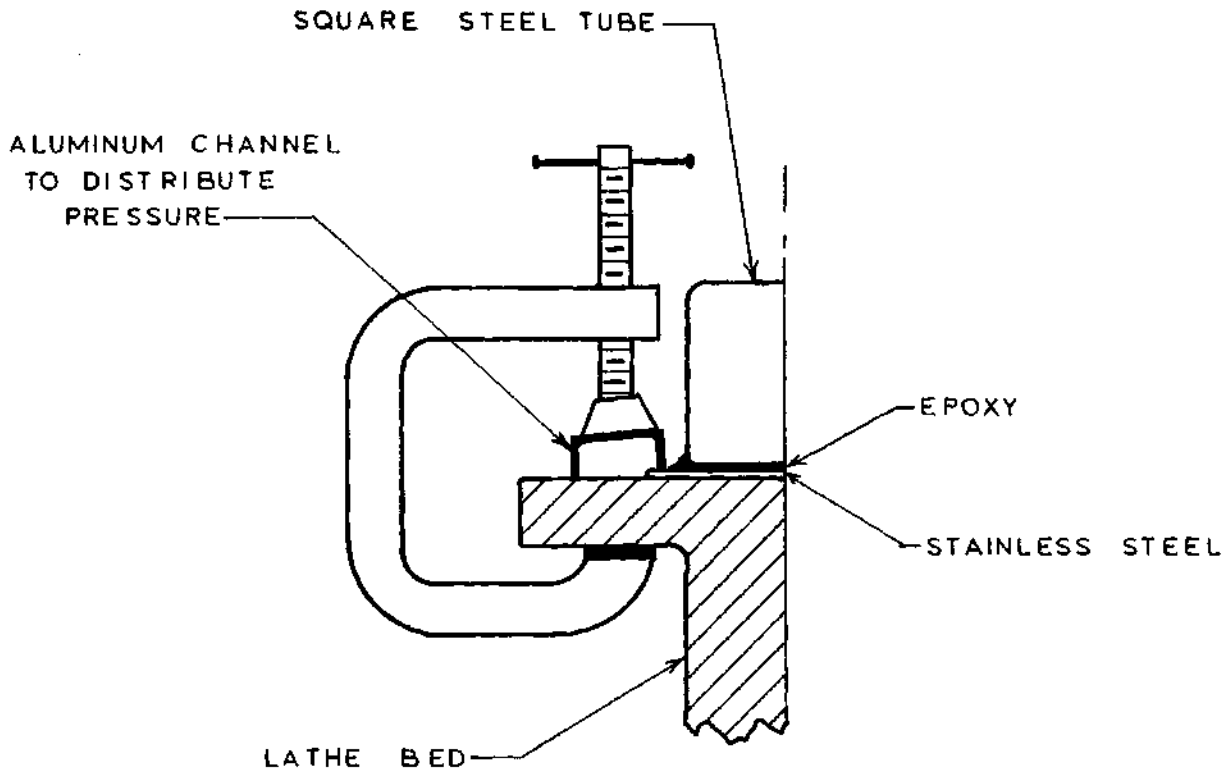

Figure 4. Segment Fabrication Technique

Fabrication of the Concentrator

The full scale concentrator was constructed from the initial design as modified in accordance with the changes required in the small prototype. Sixty 1-1/2 inch by 42 inch segments were needed to provide the 25 square feet of reflective area desired. These were divided into two equal arrays which shared a common centerline. So constructed, the concentrator has a nominal width of 51 inches and a nominal length of 86 inches. Figure 5 gives an overall view of the full scale concentrator. Most of the components of the concentrator are made of noncorrosive materials and all other components are treated to retard corrosion. The concentrator is mounted on a rigid frame, and six jack screws are provided to lift the concentrator off its wheels and to provide a means of leveling the concentrator.

Receiver Designs

McCrary[18] designed and fabricated the various receiver configurations having been given the criteria that: (a) the receiver diameter should be as near two inches as possible, but in no case less than two inches; (b) the portion of the receiver upon which the composite image was to fall should be six inches longer than the composite image; and (c) the bottom half of the receiver must be surfaced as the absorbing area. These criteria were based primarily on the results of the prototype tests.

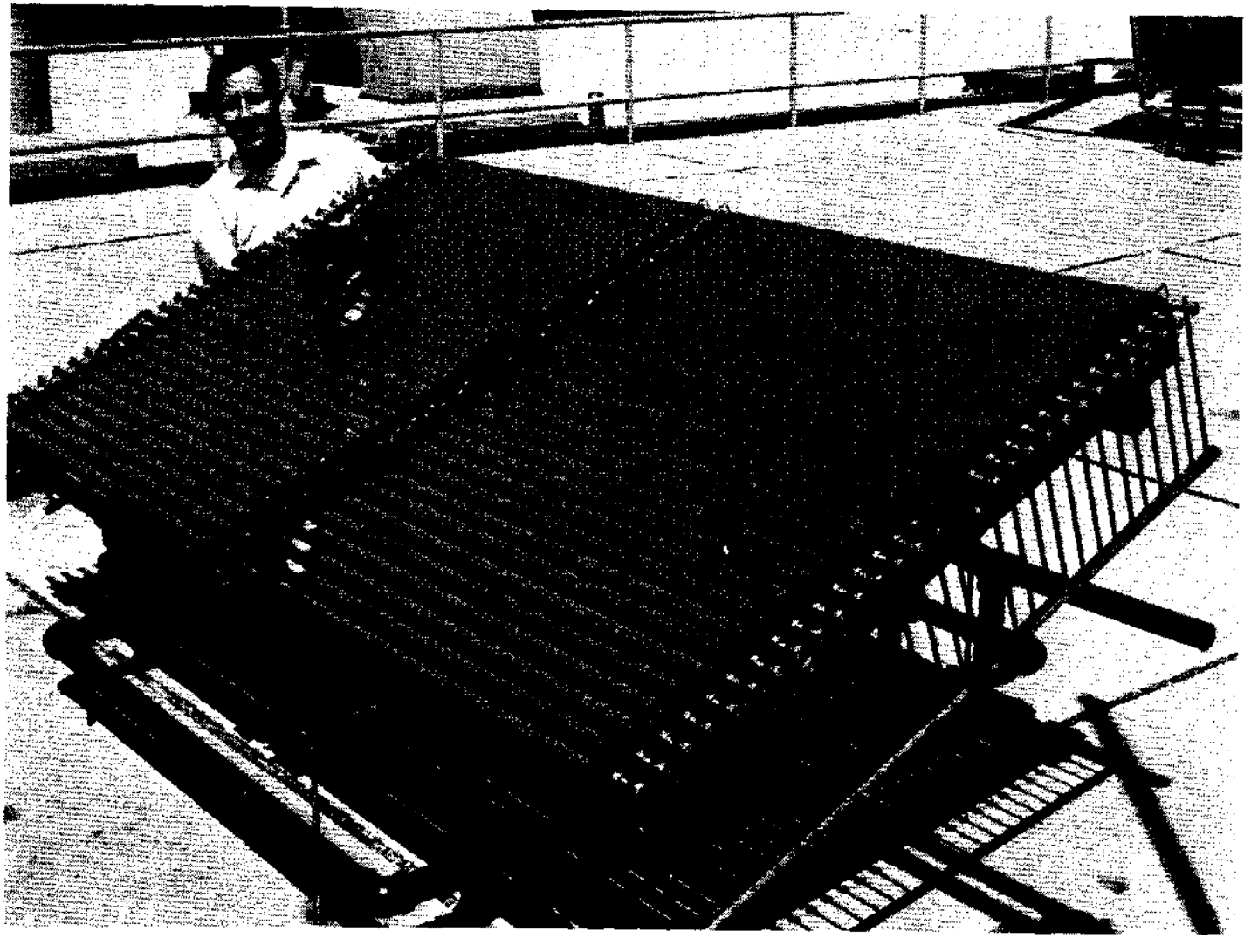

Figure 5. Full Scale Concentrator

The bare pipe receiver shown in Figure 6 was constructed to serve as a basis for comparison of all subsequent receiver designs. The air vent shown was installed on top of the receiver so that trapped air could be bled off. A thermocouple well 3/4 inch deep and 1/4 inch in diameter was installed to indicate the temperature of the water in the receiver. A commercially available carbon black paint was used to surface the bottom half of the pipe. This basic receiver pipe was used as part of all successive receivers.

The next three receiver configurations tested are shown in Figure 7. In the first case a metal shroud was formed and placed around the receiver pipe. The shroud was secured to, but held away from, the pipe by bolts soldered to the top of the pipe. The space between the pipe and shroud was filled with insulation and sealed at each end. The opening on the bottom of the shroud was made as small as possible without interfering with the incoming concentrated flux. The next two configurations involved adding an initial, then a second layer of clear plastic film to the shroud as shown. The plastic film used was Tedlar,[4] a polyvinyl flouride which is cheaper and has better transmission characteristics than ordinary glass.

The last configuration is shown in Figure 8. It was formed by surrounding the receiver pipe with a clear acrylic tube. There was a 3/8 inch space between the receiver pipe and the acrylic tube with provisions for evacuating this

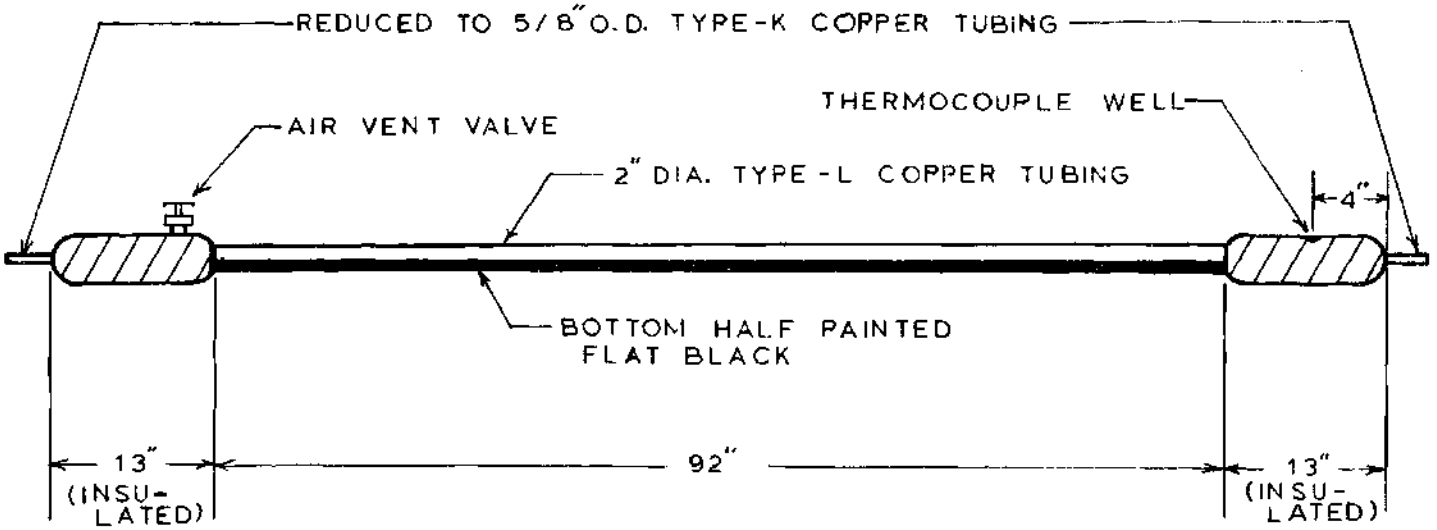

Figure 6. Bare Pipe Receiver

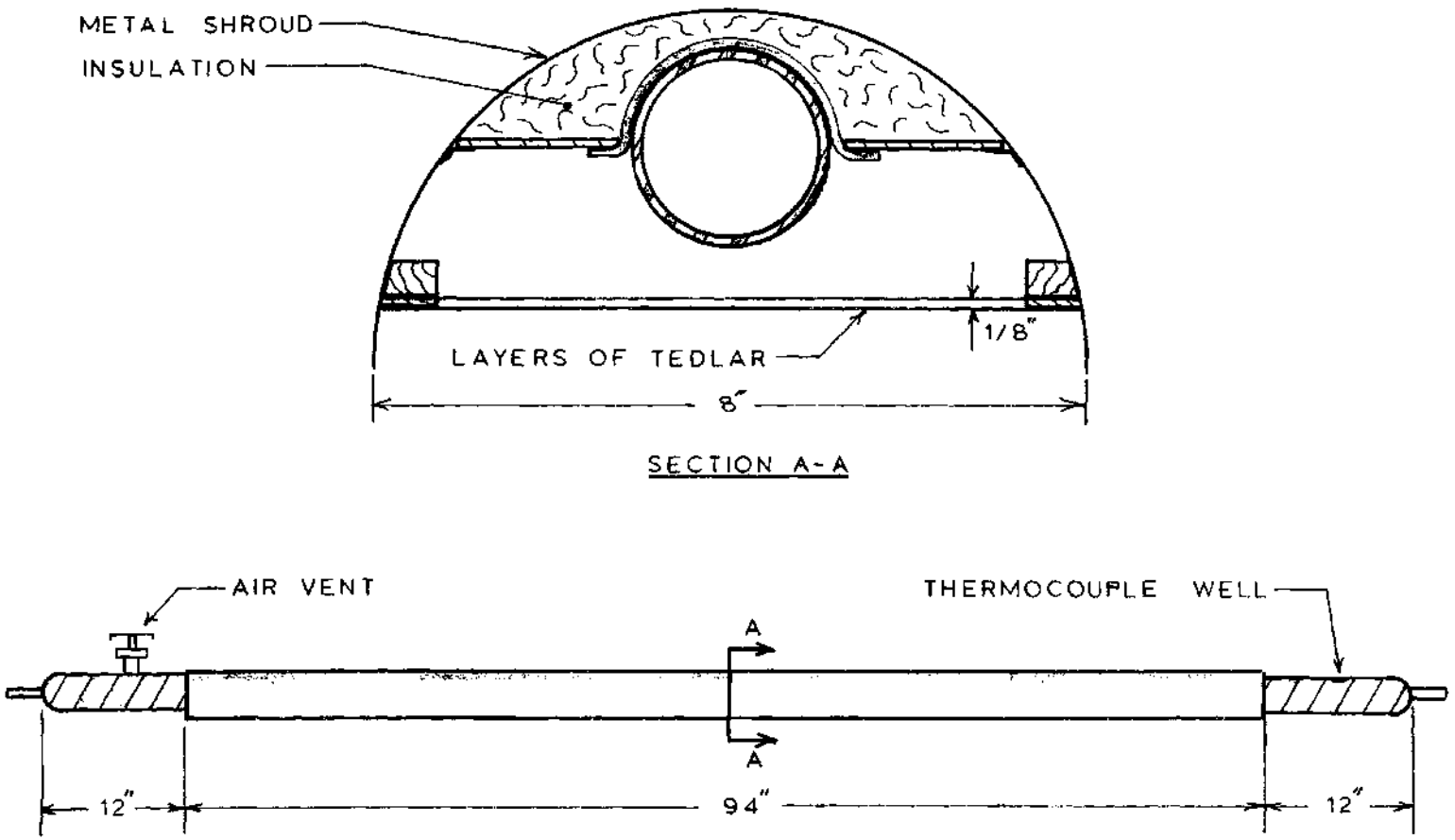

Figure 7. Shrouded Pipe Receiver Configurations

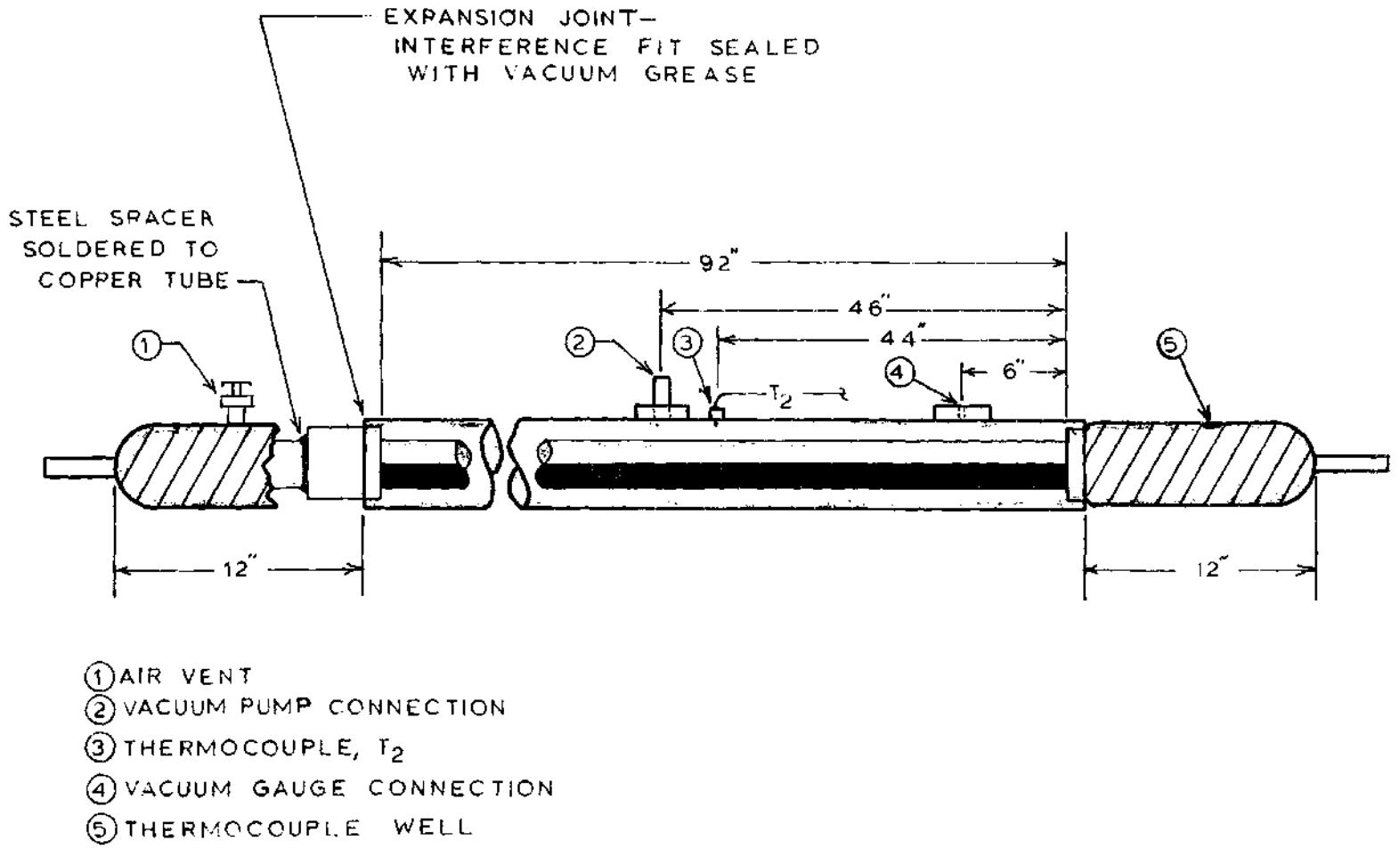

Figure 8. Acrylic Tube Receiver Configuration

annular space. The acrylic tube was selected over glass primarily due to its workability and a smaller probability of accidental breakage.

CHAPTER III

EXPERIMENTAL PROGRAM

Flow Circuit

The flow circuit, as shown in Figure 9, consisted of the receiver and cooling coil branches. The cooling coil branch was provided to eliminate fluctuations in the flow rate caused by changes in the temperature of the valve during initial tests.

The flowrate of the system did not exceed three lbm/min, and most flowrates were in the range of zero to one lbm/min. Due to the low flowrates involved, a graduated cylinder and stop watch were used to measure the flow.

The receiver control valve shown in Figure 9 was located downstream of the receiver in order to produce enough back pressure so that any air in the receiver could be bled off. The section of hose in the receiver branch upstream of the receiver was covered with a reflective foil to prevent the temperature of the water from rising due to the incident solar energy.

Instrumentation and Equipment

Copper constantan thermocouples and a Leeds and Northrup potentiometer were used throughout the experimental program. The thermocouple wells, each filled with oil, were

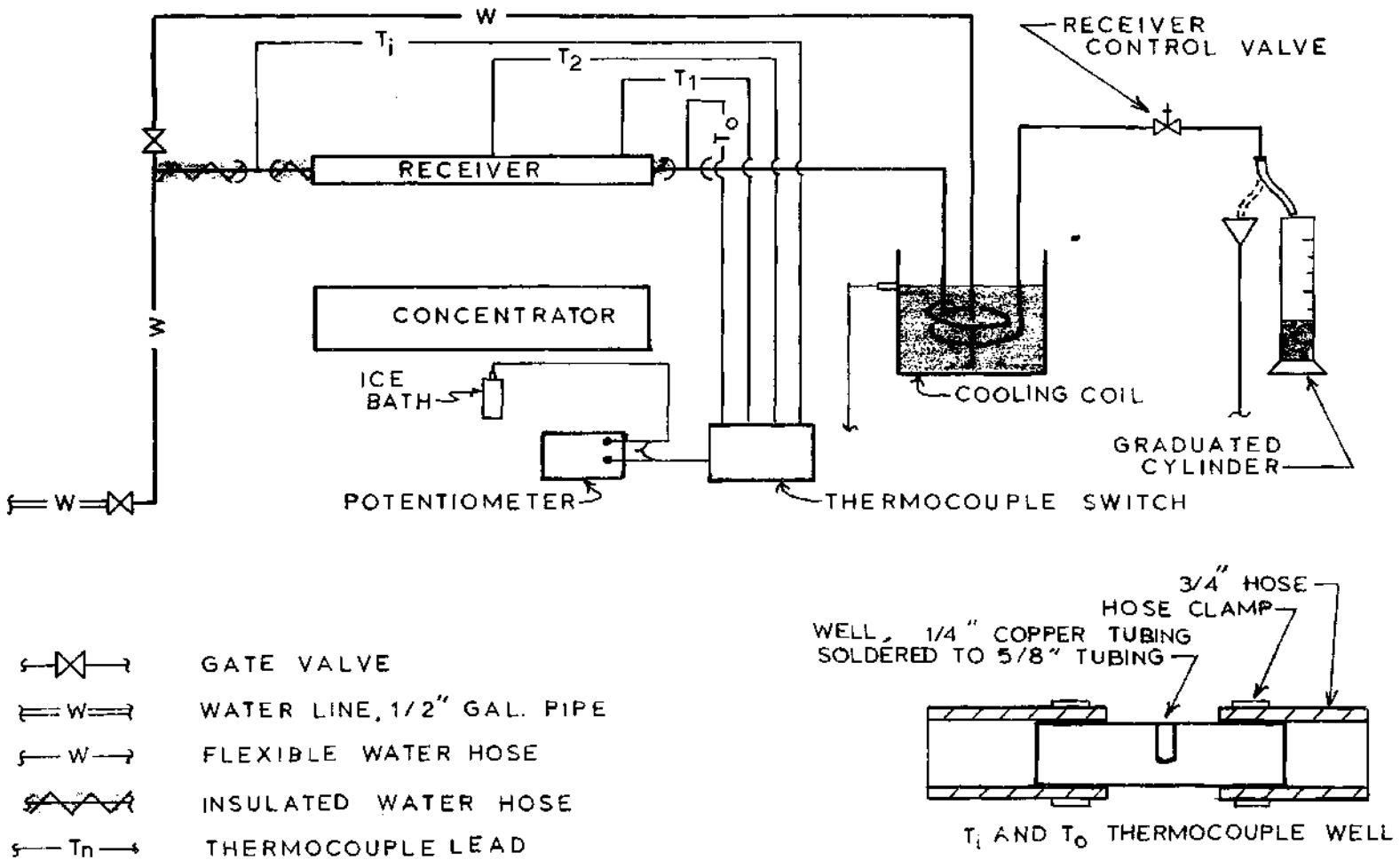

Figure 9. Flow Circuit and Experimental Apparatus

located as shown in Figure 9. Thermocouple number one, T_1, was used to monitor the water temperature in the receiver and for comparison with other thermocouple data. The inlet and outlet thermocouple wells, T_i and T_o, were each isolated from the receiver by five inch lengths of rubber hose; these were fabricated as shown in Figure 9. Thermocouple number two, T_2, was used only with the acrylic tube receiver and monitored the temperature of the air in the gap between the copper pipe and the acrylic tube.

A Welch vacuum pump was used in the evacuated acrylic tube test, and was connected to the receiver with a four foot length of 3/4 inch inside diameter rubber vacuum hose. The vacuum pressure was monitored with a Hastings vacuum gage and a DV-6m gauge tube.

The wind speed was measured in feet per minute with a stop watch and a Taylor vane anemometer, and the wind direction was determined by a vane. These measurements were taken near the center of the receiver tube. The ambient temperature was measured with a mercury thermometer which was shaded from the sun.

Physical Arrangement

Figure 10 indicates the overall dimensions of the experimental apparatus, excluding the instrumentation. The variable motion of the receiver is indicated by arrows in this figure. Figure 11 is an overall view of the experimental

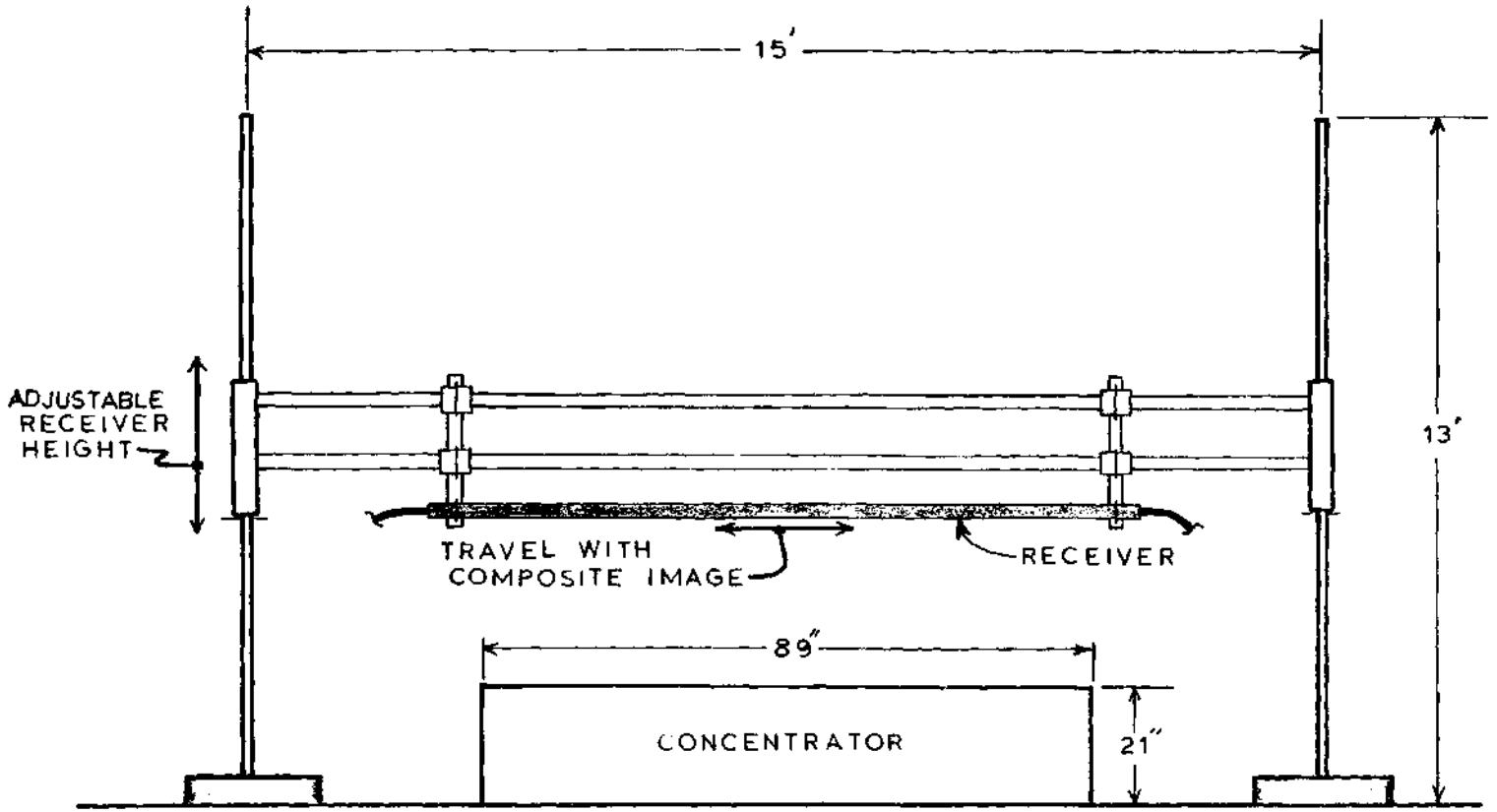

Figure 10. Physical Dimensions of Experimental Apparatus

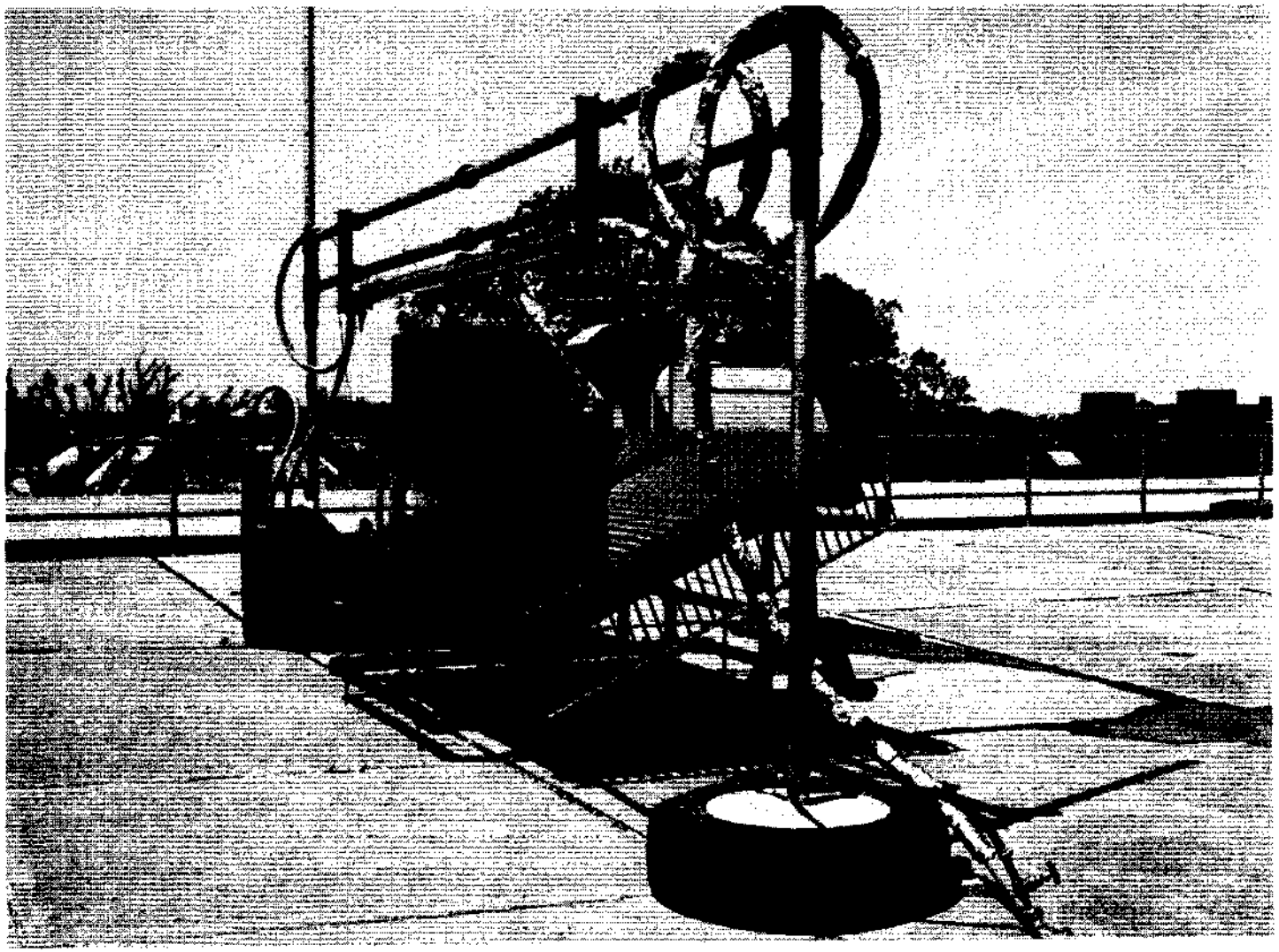

Figure 11. Overall View of Experimental Apparatus

apparatus showing the unevacuated acrylic tube receiver being evaluated with the concentrator in a tilted position.

Focusing of the Concentrator

Following any relative motion between the concentrator and the receiver, except longitudinal translation of the receiver, the former must be refocused. This occurred three times during the experimental program. Focusing is accomplished by first loosening all lock nuts. Next a segment is rotated until its image is projected onto the receiver. Then the locking nut is tightened with care not to rotate the segment. This procedure is followed until all segments are properly positioned which takes about 30 minutes and is most easily accomplished during the hour before and after solar noon.

Procedure

For a particular days testing the concentrator was usually already focused. Therefore, the first requirement was to tighten all hose clamps, close the receiver control and cooling coil valves, pressurize the receiver branch, and bleed the air from the receiver. Next the tracking bars were adjusted so that the composite image fell on the receiver, at which time monitoring of T_1 was started. When T_1 reached approximately 200°F, the receiver control valve was set for the smallest desired flowrate, usually .2 lbm/min. After about 45 minutes, when the outlet temperature had

stabilized, the following data was recorded: the time of day, all thermocouple temperatures, the ambient temperature, the flowrate, the wind speed and direction, the vacuum pressure if applicable, and the number of segments shaded by the receiver. Then a new flowrate was set and the procedure, beginning with monitoring T_o, was repeated.

The reason for first heating the water to the maximum temperature desired and subsequently taking data at lower and lower temperatures was twofold. First, when progressing from a higher temperature to a lower one, the increased flowrate and the heat losses from the receiver allowed T_o to stabilize faster. Thus more data points were established in the course of a day's testing. Second, if one progressed from cold to hot data points, by late afternoon when the incident radiation is much less intense, it would be difficult to obtain the high outlet temperatures with a measurable flowrate.

The Experiments

In the first of three basic experiments, the performance of each receiver configuration was evaluated at a standard position as indicated in Figure 12a. In the second experiment, the unevacuated acrylic tube receiver was tested at the increased height indicated in Figure 12b to determine any resultant changes in performance. In the third experiment, the unevacuated acrylic tube was evaluated with the concentrator tilted approximately normal to the solar flux

at solar noon, as shown in Figure 12c, to ascertain the effects of tilting upon the performance of the system.

Comments on Safety of Operation

From the standpoint of safety, two points should be made concerning the operation of experiments similar to that of this program. First, dark sunglasses should be worn at all times during preparation and testing. Second, the system should be treated with caution because the receiver often contains several gallons of water under about 15 pounds of pressure and in excess of 200°F.

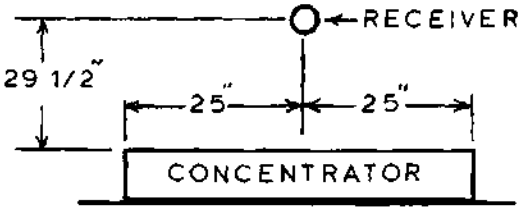

Figure 12a. Standard Height Position

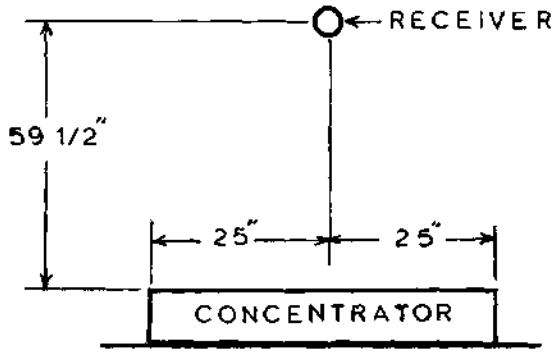

Figure 12b. Increased Height Position

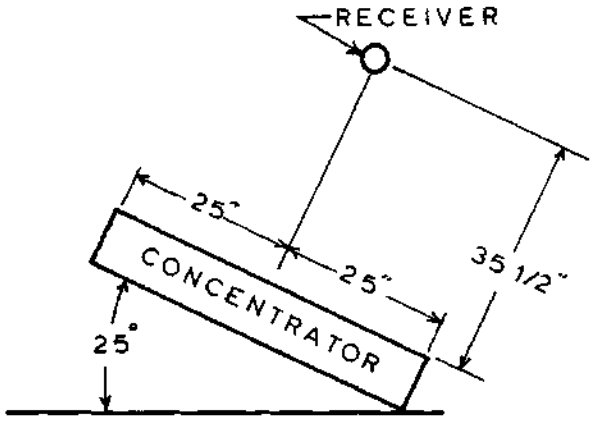

Figure 12c. Tilted Concentrator Position

CHAPTER IV

EXPERIMENTAL RESULTS AND DISCUSSION

General Discussion

For the purpose of evaluating a concentrator-receiver system, the thermal efficiency, η_T, is defined as the ratio of the heat conveyed to the heat transfer fluid, to the direct radiant energy incident upon the concentrator. During the experimental program, sufficient data was taken to evaluate the thermal efficiency of each concentrator-receiver system for each test condition. These values are tabulated in Tables 14 through 20 of Appendix D. However, as explained in the text which follows, care must be exercised in directly comparing efficiencies evaluated for differing test conditions.

The thermal efficiency may be expressed as

$$\eta_T = \frac{\dot{Q}_{in} - L_T}{\dot{Q}_{in}} , \tag{1}$$

where $\dot{Q}_{in}$ is the energy incident upon the concentrator, and L_T is comprised of the total system losses expressed as

$$L_T = L_g + L_{ac} + L_{or} + L_q, \tag{2}$$

where

L_g = geometric losses,

L_{ac} = absorptive losses of the concentrator,

L_{or} = optical losses of the receiver, and

L_q = thermal losses of the receiver.

The nature of these losses is self-explanatory except that of the geometric losses which are the losses caused by the spaces between segments, and that of the optical losses of the receiver which may include, for example, energy reflected from the receiver pipe and the various transparent insulations.

The energy absorbed by the reflectors, and the optical losses of the receiver, are functions of the incident radiation and the particular concentrator-receiver system. The geometric losses are a function of the incident radiation and the position of the sun as indicated by θ, which is the angle between the vertical normal and a component of the solar flux line normal to the east-west axis of the concentrator. The thermal losses may be expressed as

$$L_q = UA(\Delta T), \tag{3}$$

where U is the overall heat transfer coefficient for a given receiver, A is a convenient area basis for the value of U, and ΔT is the mean temperature differential between the receiver and the ambient. A is a system constant, and U is a function of the wind and the type of receiver. Therefore,

the thermal efficiency may be expressed as

$$\eta_T(c\text{-}r,w) = f(\dot{Q}_{in},\theta,\Delta T)\,, \tag{4}$$

where c-r and w indicate the dependence of thermal efficiency upon a given concentrator-receiver system and a given wind condition. Equation (4) reveals that in order to compare the thermal efficiencies of concentrator-receiver systems directly, four of the five variables must be held constant. It being virtually impossible to hold any of these constant except the type of concentrator-receiver system tested, such an attempt was not made. Instead, equation (4) is interpreted in absolute terms as

$$\eta_{T_{c\text{-}r,w}} = \frac{G\cdot R\cdot O_r\cdot\dot{Q}_{in}\text{-}UA(\Delta T)}{\dot{Q}_{in}}\,, \tag{5}$$

where G is the geometric ratio which accounts for the geometric losses, R is the reflective ratio which accounts for the absorptive losses of the concentrator, O_r is the optical ratio of the receiver which accounts for the optical losses of the receiver, and c-r and w indicate the dependence of thermal efficiency upon the type of concentrator-receiver system and a given wind condition. The physical significance of the various ratios can be better understood with reference to the energy balance diagram of Figure 13. In the following, the values of G, R, O_r, and UA are determined so that for

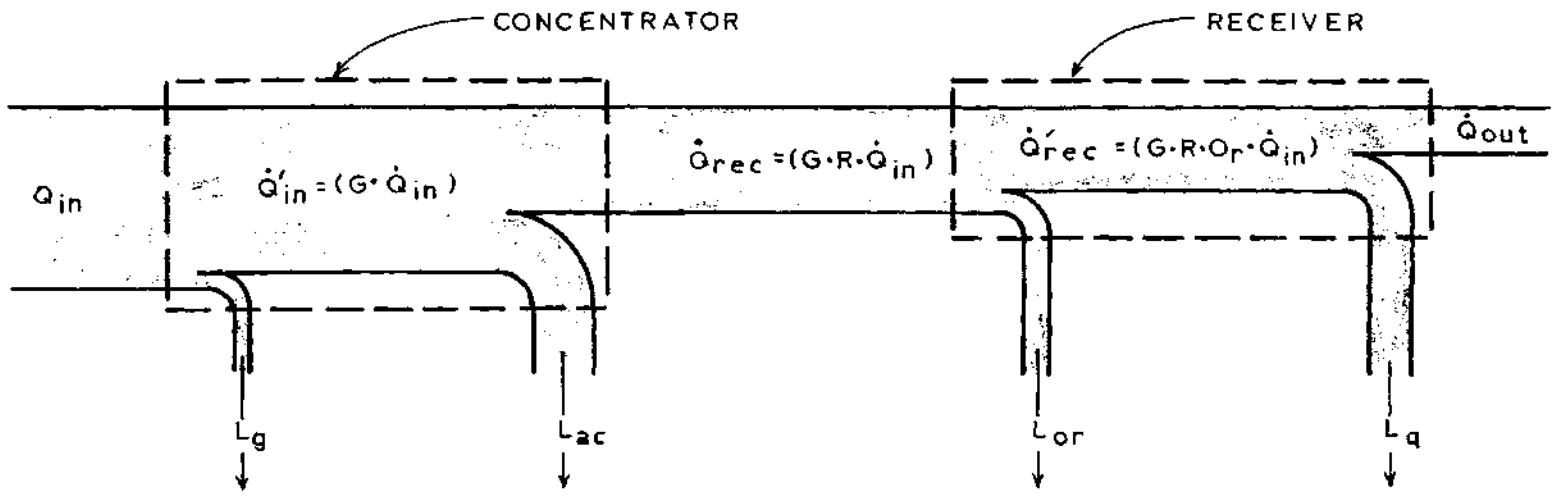

LEGEND

$\dot{Q}_{in}$ -ENERGY INCIDENT UPON CONCENTRATOR (CALCULATED VIA APPENDIX-B)

$\dot{Q}'_{in}$ -ENERGY INCIDENT UPON REFLECTORS

$\dot{Q}_{rec}$ -ENERGY REFLECTED ONTO RECEIVER

$\dot{Q}'_{rec}$ -ENERGY INCIDENT UPON RECEIVER AND CONVERTED INTO THERMAL ENERGY

$\dot{Q}_{out}$ -THERMAL ENERGY TRANSFERRED TO HEAT TRANSFER FLUID

L_g -GEOMETRIC LOSSES (APPENDIX-A)

L_{ac} -LOSSES BY ABSORPTION OF THE REFLECTIVE SEGMENTS

L_{or} -OPTICAL LOSSES OF RECEIVER

L_q -THERMAL LOSSES

G -GEOMETRIC RATIO- $\dot{Q}'_{in}/\dot{Q}_{in}$

R -REFLECTIVE RATIO- $\dot{Q}_{rec}/\dot{Q}'_{in}$

O OPTICAL RATIO- $\dot{Q}'_{in}/\dot{Q}_{rec}$

Figure 13. Energy Balance Diagram

any values of $\dot{Q}_{in}$, ΔT, and θ, the performance of each concentrator-receiver system can be predicted.

In this analysis, the mean surface temperature of the receiver pipe, T_s, is taken as being equal to the outlet temperature of the receiver, T_o. This assumption is quantitatively substantiated by the analysis of the following section where it is shown that this assumption leads to close correlation of the experimental and calculated values of the average heat transfer coefficient for the bare pipe receiver. This assumption is reasonable, heuristically, when it is considered that the large cross sectional area of the receiver resulted in extremely low through velocities. Therefore, recirculating flow due to natural convection was large in comparison, causing a thorough mixing to occur in the receiver. This reasoning is supported by the fact that at high values of T_o, the surface near the inlet end of the receiver, like that at the outlet end, was too hot to touch rather than being cool as would be the case if the through flow were predominant and a thorough mixing did not occur.

The incident radiation for this work is established by the relation

$$\dot{Q}_{in} = I_D \cdot A_c \ , \tag{6}$$

where I_D is the direct solar radiation as calculated by the method discussed in Appendix B, and A_c is the total primary

surface area of the concentrator less the area between the two arrays of reflectors and the area shaded by the receiver. By deducting the shaded area, the receiver shading variable is not required in equations (4) and (5). This is considered appropriate for this work because in a specific application, the receiver shading can be controlled or even eliminated by proper placement of the receiver. Therefore, it should be noted that if equations (4) and (5) are to be utilized for conditions where shading occurs, the definition of geometric losses should be expanded to include losses due to shading.

Analysis of the Data from the Standard Height Tests

The analysis of data for each receiver configuration follows a procedure similar to the bare pipe analysis, which is explained in detail. Succeeding sections contain only summary information about the various concentrator-receiver configuration tested and about variations from the bare pipe analysis. Specific data and supporting calculated values are tabulated in Appendix D. In all tests, the composite image was incident entirely upon the bottom half of the receiver pipe, which was coated with a carbon black paint having a solar absorptivity of 0.95.[19]

Bare Pipe Receiver

During the bare pipe tests, θ was never less than 42°. Therefore, as explained in Appendix A, no geometric losses were encountered, and thus for the bare pipe tests, the

geometric ratio for use in equation (5) equals unity. Further, since the absorptivity of the bare pipe receiver surface is 95%, the optical ratio, O_r, of equation (5) is equal to 0.95. Therefore, reference to Figure 13 indicates that

$$L_q = (1)(.95)R \cdot \dot{Q}_{in} - \dot{Q}_{out}. \qquad (7)$$

Since $\dot{Q}_{out}$ and $\dot{Q}_{in}$ are known for each data point, by assuming a value of the reflective ratio, corresponding values of heat loss can be calculated from equation (7) for each experimental condition. By plotting the values of heat loss so obtained against $(T_o - T_a)$, it can be determined if the correct value of the reflective ratio was assumed. This can be determined from the fact that the curve so formed with the correct value of the reflective ratio must pass through the intersection of the axes, since at $(T_o - T_a)$ equal to zero, the heat loss must be zero. Figure 14 shows the plot so obtained for three assumed values of the reflective ratio, with the supporting data presented in Table 1. As seen in Figure 14, this trial and error process establishes the reflective ratio as .65 and hence the reflectivity of the stainless steel as 65 percent, which is in close agreement with published data.[20,21,22] In plotting the curve of Figure 14, a constant slope is assumed for the curve, as the combined unit surface conductance, $\bar{h}$, is essentially constant over the temperature range of the experiment. The slope of the line representing a

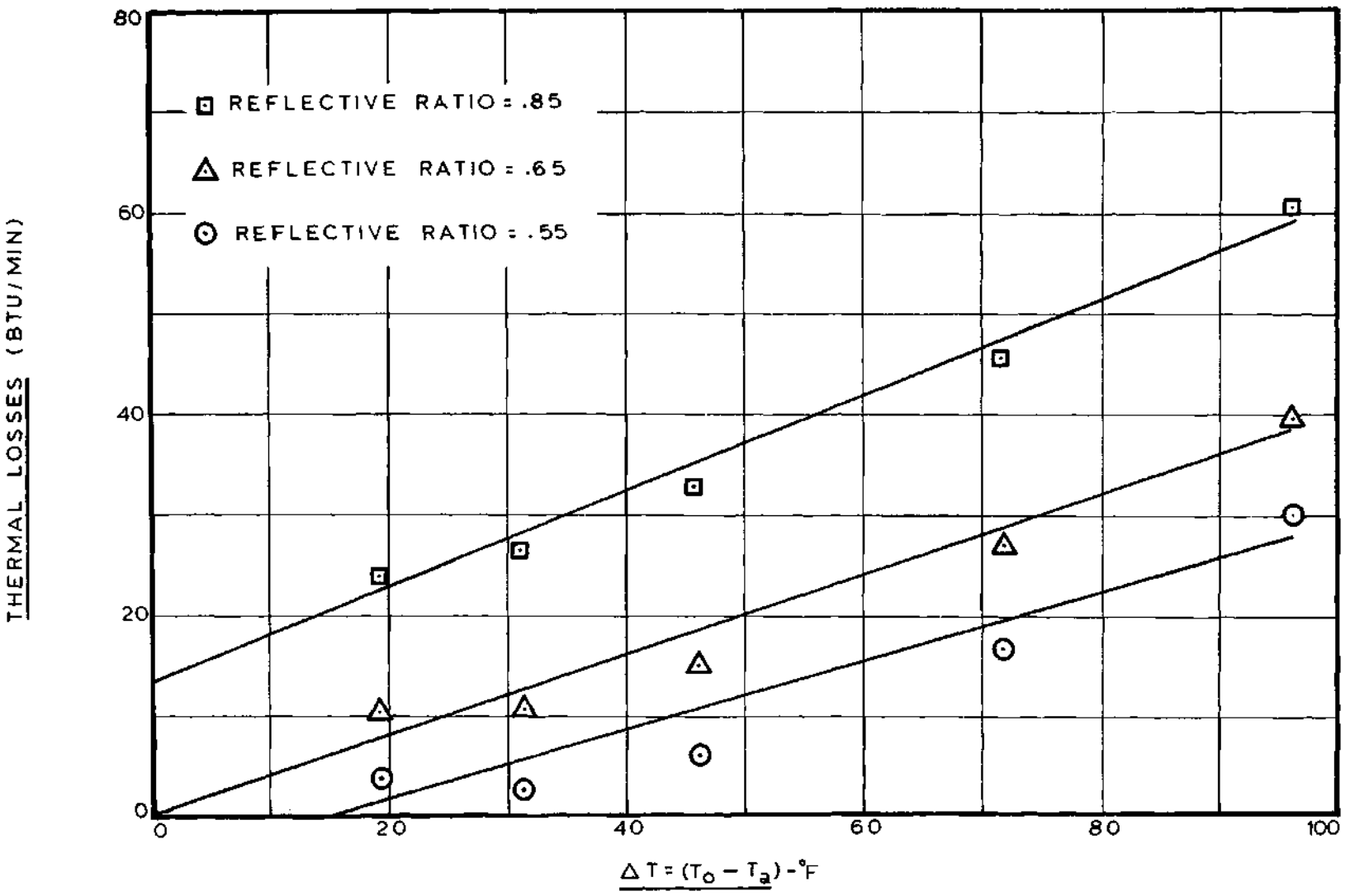

Figure 14. Analysis of Data From Bare Pipe Tests

Table 1. Analysis of Data from Bare Pipe Tests

Solar Time	$\dot{Q}_{in}$ * (Btu/min)	$\dot{Q}_{out}$ * (Btu/min)	$T_o - T_a$ * (°F)	L_q ** for R=.55 (Btu/min)	L_q ** for R=.65 (Btu/min)	L_q ** for R=.85 (Btu/min)
1205	105.5	25.2	96.0	29.9	39.9	60.0
1300	99.5	35.0	71.0	17.0	26.5	45.3
1330	92.5	42.4	46.0	6.0	14.7	32.2
1355	86.4	43.1	30.5	2.0	10.3	26.6
1435	73.3	34.8	19.0	3.5	10.5	24.3

*From Table 14

**Calculated from equation (7).

reflective ratio of .65 in Figure 14 equals the product UA, which is also equal to $\bar{h}A$, since for the bare pipe,

$$L_q = UA(T_o - T_a) = \bar{h}A(T_o - T_a).$$

The slope of the line representing a reflective ratio of .65 in Figure 14 is .40 Btu/min/°F. Therefore, since the outside area of the pipe is 4.27 ft^2, $\bar{h}$ determined experimentally is .094 Btu/min/ft^2/°F, or 5.64 Btu/hr/ft^2/°F. This value is in close agreement with the calculated value of .114 Btu/min/ft^2/°F, or 6.87 Btu/hr/ft^2/°F, determined in Appendix C. The calculated value of $\bar{h}$ is for the same conditions as the 1205 PM bare pipe test and is based on the assumption that the mean surface temperature of the receiver is equal to the outlet temperature. It should be noted that if that assumption were substantially erroneous, the calculated and experimental values of $\bar{h}$ would not agree so closely, but rather the experimental value would be considerably lower than the calculated value.

Summarizing, the bare pipe analysis has shown that the reflective ratio of the stainless steel is .65, that the product UA for the bare pipe is .400 Btu/min/°F, and that the assumption of equality of the average surface temperature of the receiver pipe and the outlet temperature is quite reasonable.

Shrouded Pipe Receiver

During the shrouded pipe tests, the geometric ratio was equal to unity. Using the same trial and error procedure demonstrated for the bare pipe data analysis, the reflective ratio was again found to be .65, and the product UA for the shrouded pipe was found to be .330 Btu/min/°F. The plot of thermal losses used in this analysis is shown in Figure 15, and the corresponding values are presented in Table 21.

Shrouded Pipe with One and Two Layers of Tedlar

During the performance of these tests, the geometric ratio was also equal to unity. With the reflective ratio established as .65 by the bare pipe and shrouded pipe analyses, it is possible to determine the optical ratio and the product UA for other receiver configurations. The procedure is similar to that for the bare pipe except that the reflective ratio is set at .65. Thus, from Figure 13,

$$L_q = (1)(.65)\cdot O_r - \dot{Q}_{out}. \qquad (8)$$

By assuming values of the optical ratio, corresponding values of thermal losses can be calculated from equation (8). Then, by plotting the thermal losses versus $(T_o - T_a)$, the correct optical ratio is established when the resulting plot passes through the intersection of the axes. Following this procedure, the optical ratio for the shrouded pipe with one and two layers of tedlar was determined to be .75 and .62,

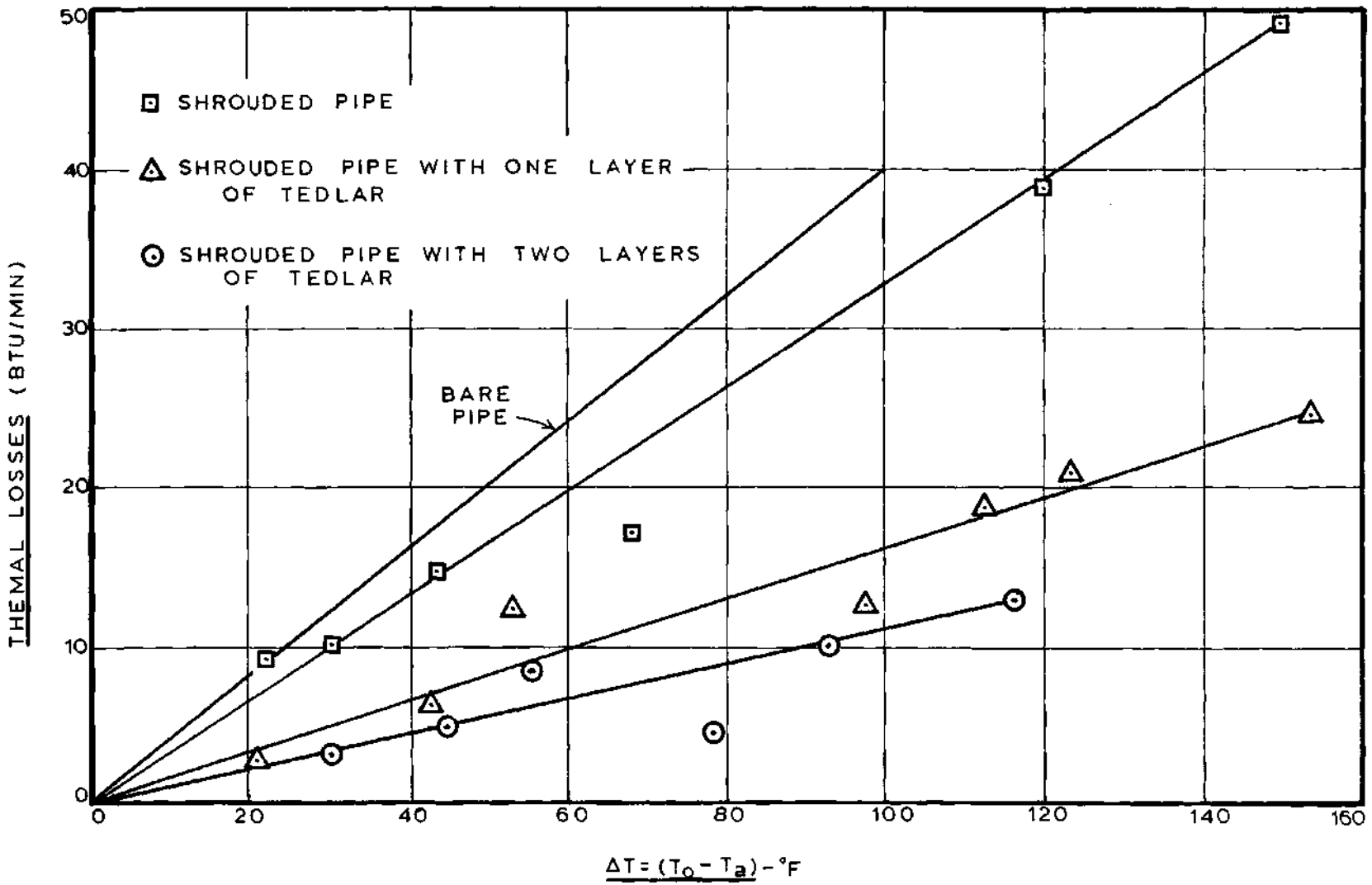

Figure 15. Analysis of Data From Shrouded Pipe Tests

respectively. Further, the corresponding values of the product UA were determined to be .163 Btu/min/°F and .108 Btu/min/°F, respectively. The plots of the thermal losses are shown in Figure 15, and the corresponding values are given in Tables 22 and 23.

Acrylic Tube Receiver, Evacuated and Not Evacuated

The data taken on March 8, 1974, for evaluating the unevacuated acrylic tube does not agree well with data taken on numerous other occasions for the same configuration. Therefore, the data taken on April 16, 1974, for the unevacuated tube is used because it is the most complete and most representative of all the data for that receiver. The data of April 16, 1974, is for the tests where the concentrator is tilted at an angle with the horizontal. However, this should have no bearing on the optical and thermal characteristics of the receiver. The data for the unevacuated receiver was evaluated in the same fashion as that for the shrouded pipe with Tedlar, with the exception that geometric losses had to be accounted for. The geometric ratio was determined by the graphical means described in Appendix A to have been approximately 0.9 during the hours of testing. Figure 16 shows the curve for the unevacuated configuration and the supporting data is presented in Table 24. The analysis indicates that the product UA for the unevacuated receiver is .158 Btu/min/°F and that the optical ratio is 0.75. This value of UA is about 40 percent higher than the

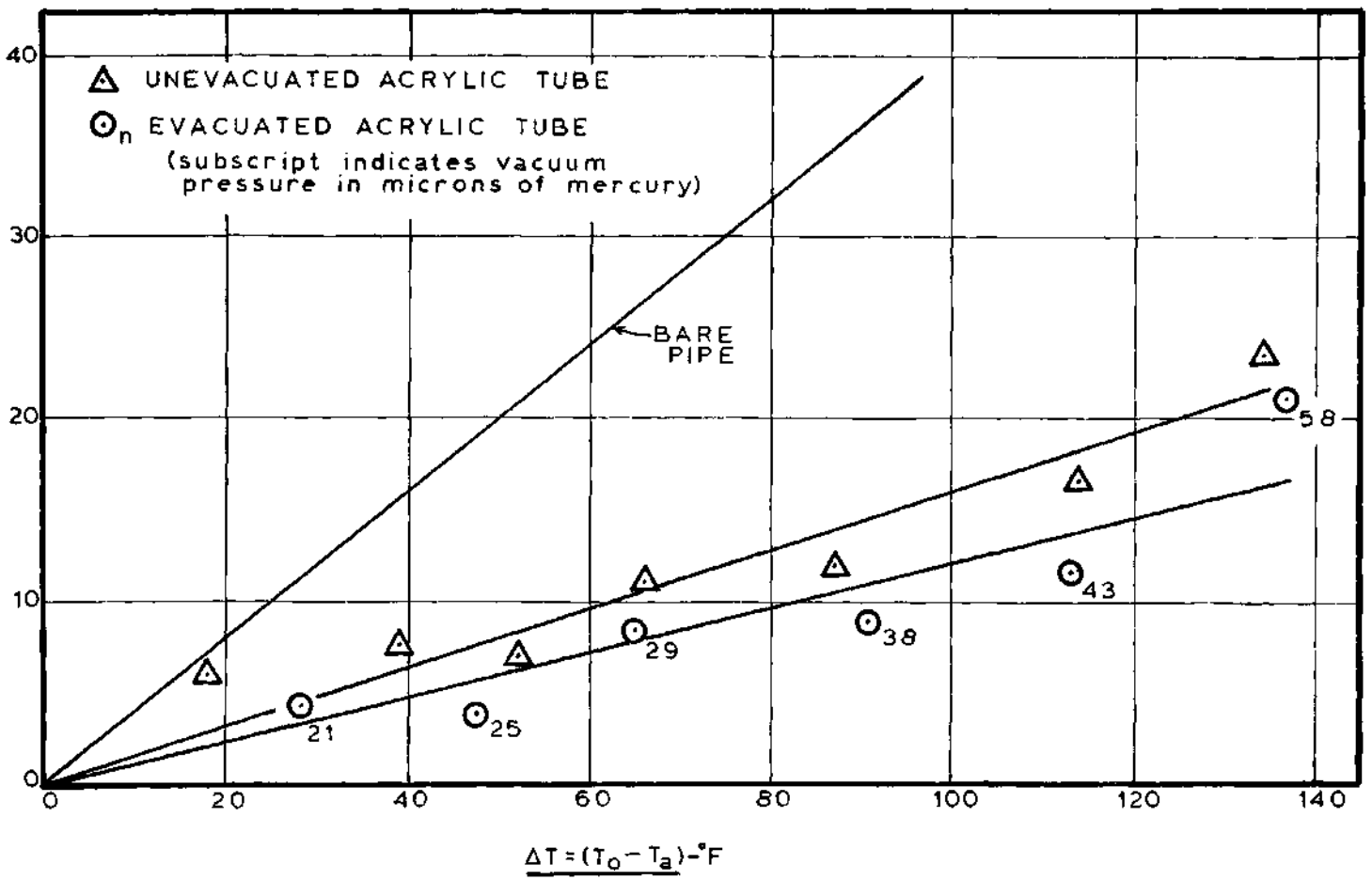

Figure 16. Analysis of Data From Acrylic Tube Tests

value of .114 Btu/min/°F calculated in Appendix C. The only known significant factor which may have caused this difference is that the acrylic tube sagged significantly during the testing, causing the clearance between the inner copper pipe and the acrylic tube to be reduced by as much as 75 percent at the top center of the receiver, and also causing the gap along the bottom to increase by an equal amount. The resultant increase in thermal resistance along the bottom was more than offset by the resultant decrease along the top because the thermal resistance is a function of the logarithm of the ratio of the radii. The heat loss model of Appendix C shows that the air gap is the primary thermal resistance in the unevacuated configuration, thus the change in gap width could account for much of the difference in the calculated and experimental values of UA. The sag was caused by slight inaccuracy in the fabrication of the acrylic tube from two short sections and by the weakening of the acrylic at high temperatures.

The data for the evacuated acrylic tube receiver is also plotted in Figure 16, with the accompanying data given in Table 25. The conductivity of air is relatively independent of pressure until the pressure approaches that pressure where the mean free path of the molecules of air is equal to the gap width. As the pressure is reduced below that range, the conductivity is reduced proportionately. In the analysis of Appendix C, it is shown that for a gap width of .34 inch,

such as that for the acrylic tube receiver gap, the pressure would have to have been reduced to 5.8 microns of mercury before the conductivity of the air would have been significantly affected. Since the lowest vacuum attained was 21 microns, the conductivity of the air was never affected. Accordingly, there is little difference between the slope of the line for the evacuated case, .121 Btu/min/°F, and that of the line for the unevacuated case, .158 Btu/min/°F. The slight difference in the slopes is attributed to the possible difference in the sag of the acrylic tube for the two experiments and to the fact that the vacuum greatly reduced the amount of heat transfer by convection between the pipe and the tube. The heat transfer analysis in Appendix C shows that convection for an air gap of .34 inches, effectively increases the conductivity of the air by about twelve percent. Therefore, a substantial reduction in the convective effect could account for as much as fifty percent of the difference.

Analysis of the Unevacuated Receiver at an Increased Height

On April 7, 1974, the unevacuated acrylic tube was tested at a height of 59-1/2 inches above the concentrator for comparison with the performance of the system at the standard receiver height. Focusing at the increased height was easier and produced a sharper image due to the accompanying decrease in aperture angle. It was also apparent that the

composite image traveled faster from west to east along the receiver centerline and that the position of the tracking bars had to be adjusted more frequently. These effects are easily understood with reference to the geometric considerations detailed in Appendix A. A third effect which was not as obvious during the test was that at the increased height, greater geometric losses were encountered than would have been at the standard height. This is explained by the fact that when the receiver is raised and the segments are focused, the segment surfaces are more nearly parallel to the horizontal. This decreases the geometric losses for the segments on the southern side of the concentrator. However, this decrease is more than offset by an increase for those on the north side. Using the graphical procedure detailed in Appendix A, the geometric ratio for the increased height test was determined to have been .91. The experimental performance of the acrylic tube receiver at the increased height is summarized in Table 2, with the supporting data presented in Table 26.

The performance of the acrylic tube receiver tested at the standard height, under the same conditions as the increased height test, can be predicted from the relation

$$\dot{Q}_{out} = G \cdot R \cdot O_r \cdot \dot{Q}_{in} - L_q, \qquad (9)$$

where

Table 2. Comparison of Performance of the Unevacuated Acrylic Receiver at Heights of 59.5 and 29.5 Inches

Solar Time	Performance at 59.5 Inches (Experimental)			Performance at 29.5 Inches (Predicted)		
	$\dot{Q}_{in}$ (Btu/min)	$\dot{Q}_{out}$ (Btu/min)	η_T	$\dot{Q}_{in}$ (Btu/min)	$\dot{Q}^{*}_{out}$ (Btu/min)	η_T
1145	128.4	34.3	26.7	128.4	36.2	28.2
1230	126.3	34.5	27.3	126.3	36.4	28.8
1255	124.0	46.8	37.7	124.0	48.6	39.2
1320	120.0	45.5	37.9	120.0	47.4	39.4
1340	114.0	41.4	36.3	114.0	43.0	37.7

*Thermal output determined by equation (9).

G = .94 by graphical analysis,

R = .65 by previous analysis,

O_r = .75 by previous analysis,

and $\dot{Q}_{in}$ and L_q are the same as those for the increased height test. The results of this procedure are also summarized in Table 2, with appropriate calculated values given in Table 27. Comparison of the results of Table 2 shows that there was only about a 1.5 percent decrease in efficiency at the increased height. However, that decrease could be higher or lower, depending on the position of the receiver and the position of the sun.

Analysis for the Tilted Concentrator Test

The positions of the concentrator and receiver for the tilted concentrator test were previously indicated in Figure 12. Two counteracting effects were encountered when the concentrator was tilted. First, the concentrator was more nearly normal to the solar flux for most of the day, so that the energy incident upon the concentrator was greater. Second, greater geometric losses were encountered because tilting the concentrator also made the spaces between the segments more normal to the solar flux, which increased the gap losses. Using the graphical procedure outlined in Appendix A, the geometric ratio for the tilted position was determined to have been essentially constant at 0.9. The experimental performance of the tilted concentrator is summarized in Table 3, with

Table 3. Performance of Unevacuated Acrylic Tube Receiver with the Concentrator Tilted

Solar Time	Performance for Tilted Concentrator, G=.90 (Experimental)			Performance for Horizontal Concentrator, G=.94 (Predicted)			Performance for Tilted Concentrator, G=.94 (Predicted)		
	$\dot{Q}_{in}$*	$\dot{Q}_{out}$*	η_T	$\dot{Q}_{in}$*	$\dot{Q}_{out}$*	η_T	$\dot{Q}_{in}$*	$\dot{Q}_{out}$*	η_T
1115	124.5	31.7	25.4	111.5	28.2	25.2	124.5	34.1	27.4
1205	126.0	39.1	31.0	112.0	35.1	29.3	126.0	41.4	33.8
1250	124.5	43.3	34.8	111.5	40.2	34.9	124.5	46.1	37.0
1310	123.5	43.5	35.2	111.0	40.3	36.3	123.5	45.9	37.1
1330	118.0	45.3	38.4	109.0	43.6	40.0	118.0	47.6	40.3
1350	111.5	41.8	36.3	105.0	41.1	39.2	111.5	44.0	39.4
1420	102.0	39.2	38.4	98.0	39.5	40.4	102.0	41.1	40.3

*Btu/min

supporting data compiled in Table 28.

The performance of the concentrator-receiver system can be predicted for the case where the concentrator and receiver maintain their relative positions but the concentrator is horizontal, and where all other conditions are the same as those for the tilted concentrator tests. This is accomplished by applying the relationship

$$\dot{Q}_{out} = G \cdot R \cdot O_r \cdot \dot{Q}_{in} - L_q, \tag{10}$$

where

G = .94 is determined graphically,

R = .65 by previous analysis,

O_r = .75 by previous analysis,

$\dot{Q}_{in}$ is determined by Appendix B,

and L_q is equal to the thermal losses encountered during the tilted concentrator test. This procedure was applied to each test condition, and the results are also summarized in Table 3, with supporting value given in Table 29. Comparison of this calculated performance with the actual performance shows how much improvement was gained by tilting the concentrator. It may be noted that for each test, except the latest of the day, there was some increase in output. However, only for the tests where the incoming energy was increased enough to offset the increased geometric losses was there an increase in thermal efficiency.

The performance of the acrylic tube receiver tested under the same conditions as the tilted concentrator test can also be predicted for the hypothetical case where the concentrator is tilted by the same amount, but the geometric ratio remains constant. This is accomplished by again applying equation (10) with the exception that both $\dot{Q}_{in}$ and L_q are taken as the same as for the actual test. The results of this procedure are shown in Table 3, with appropriate calculated values given in Table 30. Comparison of this calculated performance with the actual performance shows how much advantage there would have been in tilting the concentrator had the tilting not been accompanied by a decrease in the geometric ratio.

It is important to realize that the two counteracting effects of tilting may be greater or smaller than those encountered in this program for any other conditions.

Discussion of Results

The geometric ratio can be determined graphically for any situation, and, as a result of the preceding tests and analysis, the reflective ratio, the optical ratio, and the product UA are known for each concentrator-receiver system. Equation (5) is rewritten below and a summary of the constants is given in Table 4.

$$\eta_{T_{c-r,w}} = \frac{G \cdot R \cdot O_r \cdot \dot{Q}_{in} - UA(\Delta T)}{\dot{Q}_{in}} . \qquad (5)$$

Table 4. Summary of Values Relative to Equation (5)

Receiver	G	R	O_r	UA*	Wind Speed (MPH)	Wind Direction	U**
Bare Pipe	Graphical	.65	.95	.400	1.4	NNW	5.61
Shrouded Pipe	Graphical	.65	.95	.330	6.2	NNW	4.64
Shrouded with One Layer	Graphical	.65	.75	.163	3.3	SW	2.29
Shrouded with Two Layers	Graphical	.65	.62	.108	6.6	SW	1.52
Unevacuated Acrylic Tube	Graphical	.65	.75	.158	2.0	NW	2.22

*Btu/min/°F

**Btu/hr/ft^2/°F, based on outside area of bare receiver pipe.

Reference to the evacuated acrylic tube receiver test is omitted from Table 4 and the present discussion due to the lack of sufficient experimental data. The values of U in Table 4 are calculated based on the outside area of the bare pipe receiver. Also, the values of the product UA in Table 4 are dependent upon the wind speed and direction at the time of the experiment. Therefore the average wind speed and direction is also listed. The wind speed happened to be considerably higher on the days when the shrouded pipe with two layers of Tedlar were tested. Had the wind been two to three miles per hour on those days, as it was on the days the other receivers were tested, the respective values of the product UA would be slightly smaller.

By using equation (5) and the constants from Table 4, it is possible to predict the performance of the experimental concentrator-receiver systems under any normal conditions. For example, assume that the experimental concentrator-receiver systems are to be tested at solar noon on the 21st day of February without any shading of the concentrators by the receivers. Further assume that the receivers are to be located so that the geometric ratio equals unity. For these conditions, the incident horizontal radiation would be 106 Btu/min. The predicted performance for the assumed conditions is shown in Figure 17. This figure was developed by solving equation (5) for the efficiencies of each receiver for values of ΔT equal to 10° and 100°F with the other

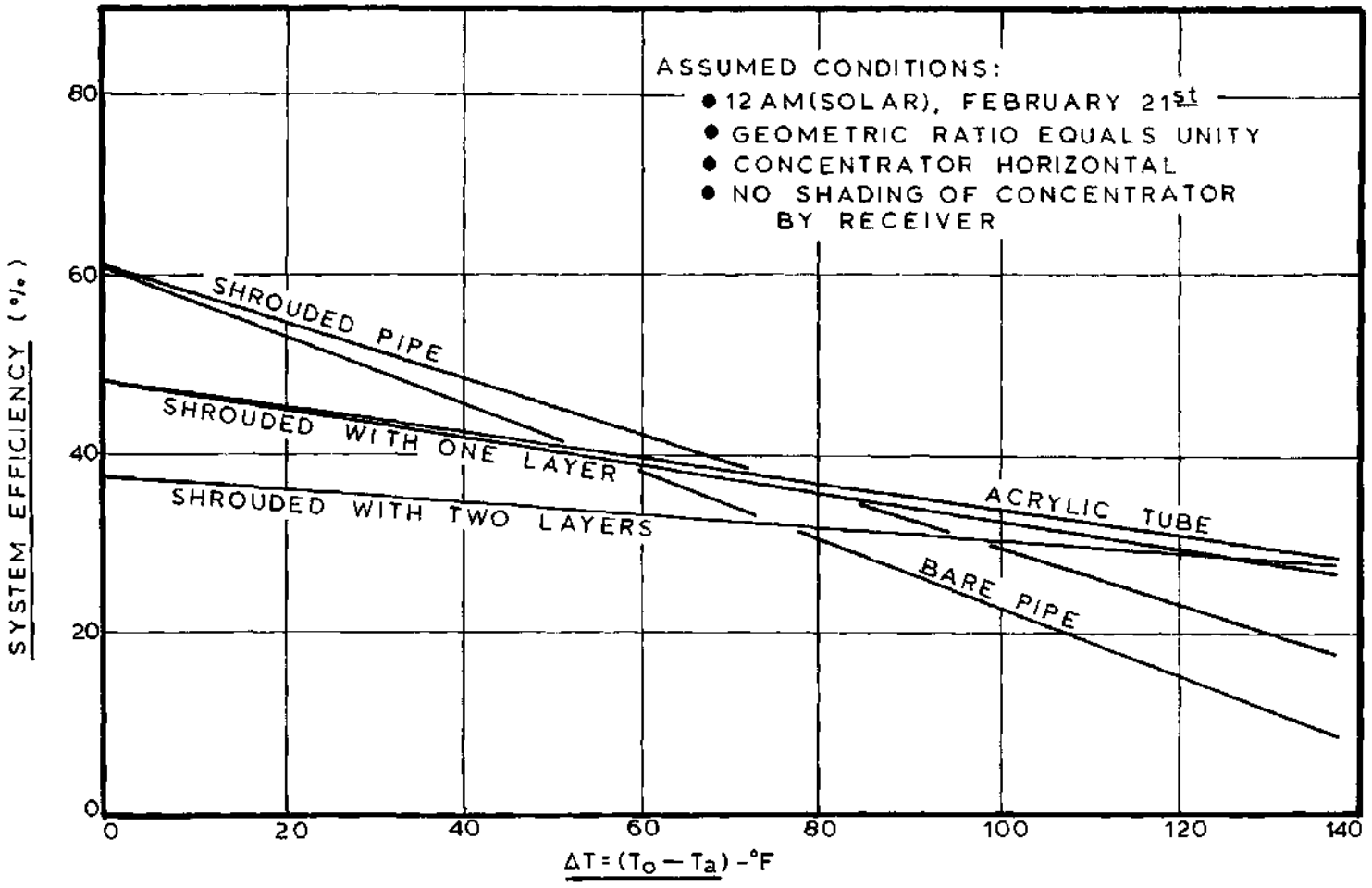

Figure 17. Comparison of Predicted Performances of the Experimental Concentrator-Receiver Systems

parameters held constant as dictated by the assumed conditions. The two values for each receiver were plotted and a straight line drawn through each pair. The calculated values used in constructing the figure are in Table 31. The linear relationship is justified because the overall heat transfer coefficient, U, is essentially constant for each receiver in the temperature range of the experiments. However, caution should be exercised in extrapolating the lines to higher values of ΔT since radiation losses, which are not proportional to ΔT, become more significant with increasing values of temperature difference.

The slopes of the lines in Figure 17 indicate how well the receivers are insulated. The slopes range from that of the bare pipe with no insulation, to that of the best insulated receiver, i.e., the shrouded pipe with two layers of Tedlar. The points where each line intersects the vertical axis represent the cases of zero thermal losses. These intercepts represent the maximum possible efficiency for each concentrator-receiver system provided negative values of ΔT are not considered. If the ambient temperature equals the inlet temperature, then the intercepts represent the case of an infinite flow rate with zero temperature rise. Thus it can be seen that the intercepts are a function of the absorptive losses of the concentrator and the optical losses of the receiver.

Figure 17 illustrates that, when transparent insulations

are used to reduce the thermal losses of the receiver, they also decrease the amount of energy which actually reaches the receiver pipe. It shows that, for low temperature differences between the receiver and the environment, the addition of transparent insulations increases the optical losses more than it decreases the thermal losses, resulting in lower efficiencies. At higher temperature differences, the opposite is true favoring the addition of transparent insulation. Therefore, as shown in Figure 17, the shrouded pipe with no transparent insultation performs best up to a temperature difference of 75°F, beyond which the acrylic tube receiver performs most efficiently.

If the curves in Figure 17 representing the shrouded pipe with two layers of Tedlar and the acrylic tube receivers are extrapolated, they intersect at ΔT equal to 150°F. This indicates that beyond that value, the shrouded pipe with two layers of Tedlar may well be more efficient. However, at some point beyond the range of ΔT where heat transfer by radiation becomes significant, the acrylic tube receiver may again be more efficient. This is because the best information available, though incomplete, indicates that the acrylic tube[23] is opaque to infrared radiation whereas Tedlar[24] is translucent. Thus the acrylic tube would provide better insulation against heat loss by radiation. However, it should be noted that the acrylic tube[23] loses much of its strength at service temperatures in excess of 160°F.

Figure 18 predicts the output of the acrylic tube concentrator-receiver system for several hours on February 21st. It was constructed by determining the thermal output of the system for values of ΔT equal to 10° and 100°F from the relation

$$\dot{Q}_{out} = G \cdot R \cdot O_r \cdot \dot{Q}_{in} - UA\Delta T, \tag{11}$$

where

G = unity,

R = .65 by previous analysis,

O_r = .75 by previous analysis,

$\dot{Q}_{in}$ is determined from Appendix B, and

UA = .158 Btu/min/°F by previous analysis.

The resulting pairs of points were then plotted and a straight line drawn through them. The related calculated values are in Table 32. This figure indicates approximately how large a single concentrator-receiver system of the same design would have to be to satisfy a given requirement. However, it should be realized that the performance characteristics of a significantly larger concentrator-receiver system would differ somewhat from those of Figure 18.

The preceding analysis determined that the reflective ratio of the polished stainless steel of the experimental concentrator was .65. Therefore, a substantial amount of energy was prevented from ever reaching the receiver, causing

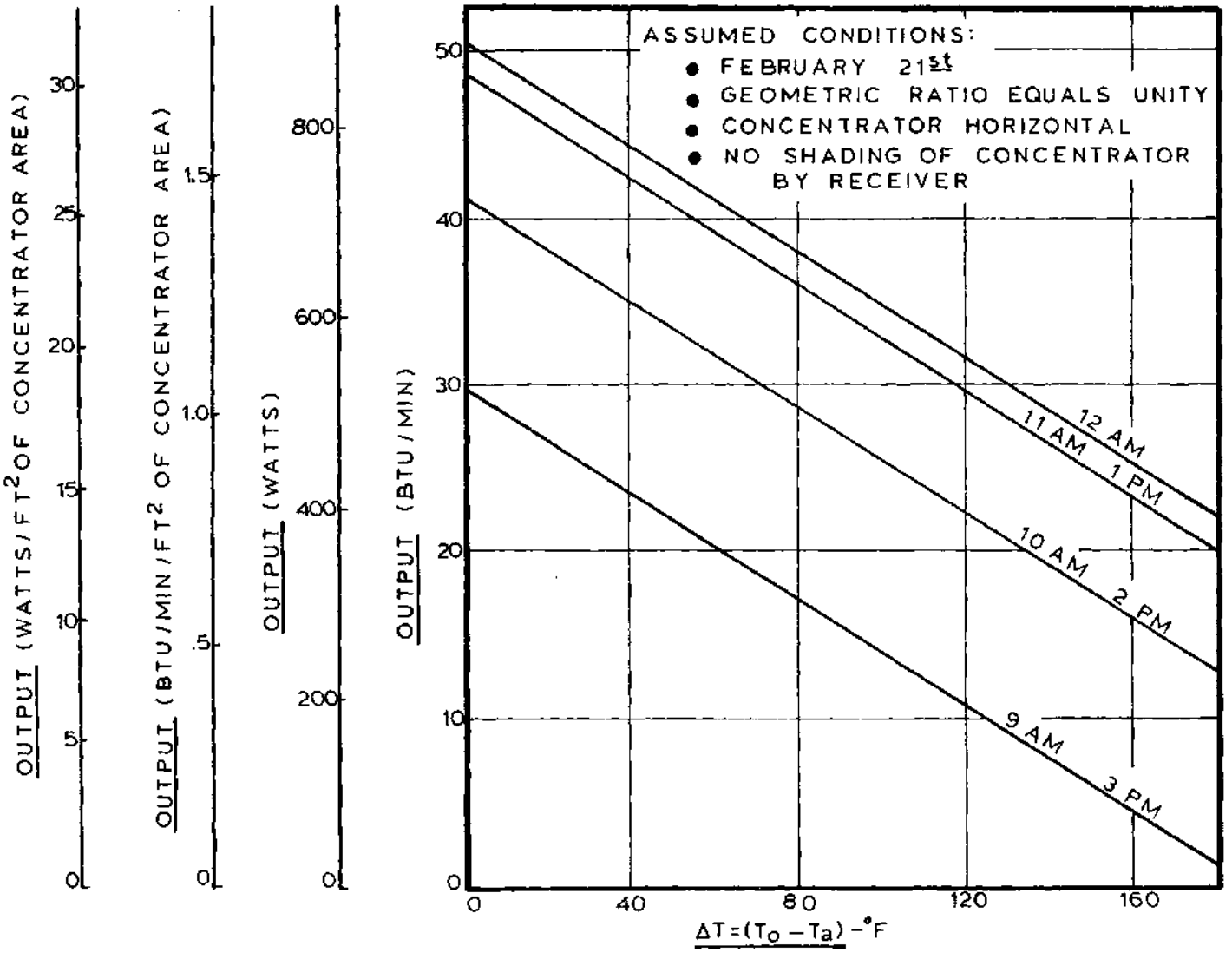

Figure 18. Predicted Performance of Acrylic Tube System in Atlanta, Georgia

a significant loss in efficiency. Substantially higher efficiencies would have resulted in the experimental program had the reflective segments been made of a material, such as a highly polished aluminum alloy[21], with a reflective ratio of .85. This point is illustrated in Figure 19 where the performance of the shrouded pipe and acrylic tube receivers are predicted for tests with concentrators having reflective ratios of .65 and .85. The same conditions and procedures used in developing Figure 17 were used in developing this figure, and the corresponding calculated values are given in Table 33. In accordance with equation (5), the increase in the reflective ratio shifts the lines vertically. It can also be seen that the vertical shift is greater for the shrouded pipe because of its higher optical ratio. This unequal shift also increases the value of ΔT at which the lines representing the shrouded pipe and acrylic tube receivers intersect.

In conclusion, the preceding analysis has shown through the increased height and tilted concentrator tests, that the geometric loss parameter is important. It has also been shown that for low temperature applications as exemplified by this work, receivers without evacuated jackets can be fabricated that will perform with reasonable efficiencies. In addition, it has been shown that significant improvements over the experimental concentrator could be achieved by increasing the reflectivity of the primary surface. Curves

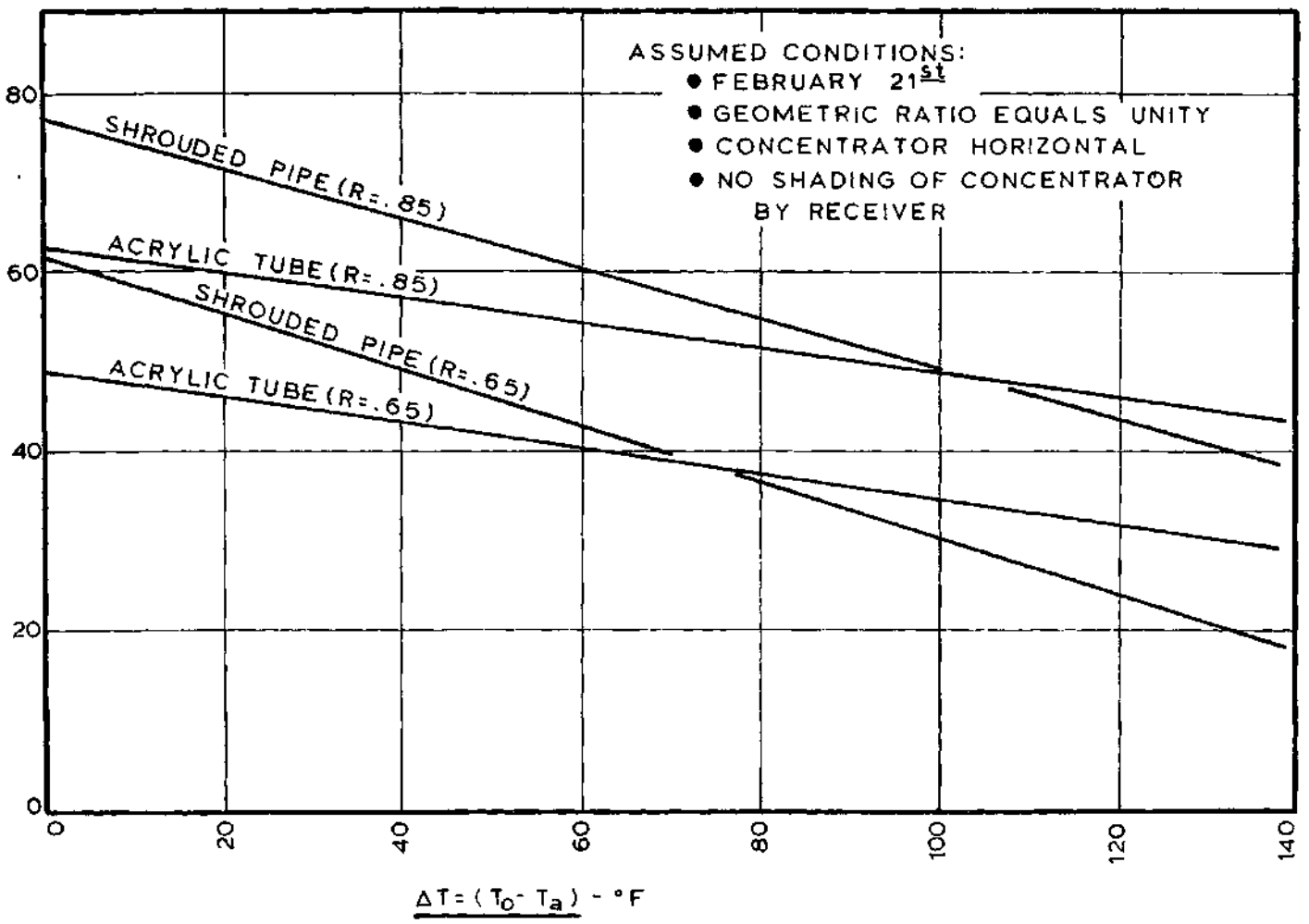

Figure 19. Predicted Effect of Varying Concentrator Reflectivity

similar to those of Figure 19 could also be generated to demonstrate improvements which could be achieved by decreasing the optical losses and improving the insulating properties of the transparent receiver insulations.

CHAPTER V

CONCLUSIONS AND RECOMMENDATIONS

Conclusions

This thesis presents the design and evaluation of a segmented plane solar concentrator and several receiver configurations. The following conclusions are drawn from this work:

1. It is feasible to economically fabricate a segmented plane solar concentrator that will efficiently concentrate incident solar radiation.

2. The advantages of the segmented plane concentrator are:

(a) Rotation of the entire concentrator about its axis is not required for tracking, thus simplifying the required supporting structure.

(b) For a given receiver position, the aperture angle is constant, which can greatly simplify receiver design.

(c) Concentration can be achieved without use of complicated surface geometries.

(d) The receiver can be located at any position parallel to the concentrator axis, making it possible to reduce or even eliminate the shading of the concentrator by the receiver.

(e) The segmented plane concentrator has a thin cross section, or in other words, has a low profile in comparison with other concentrators, which is advantageous from an esthetic point of view. Also, the low profile design means that less supporting structure is required, less wind loading is encountered, and cleaning of the reflective segments is facilitated.

(f) The reflective surfaces may be protected during hailstorms by rotating all segments so as to face downward. This would be applicable mainly in power plant applications where the tracking mechanism would allow complete rotation of all segments when deemed necessary by the attending personnel.

3. The disadvantages of the segmented plane concentrator are:

(a) Though the entire concentrator need not be rotated about its focal line for tracking, the individual segments do require coordinated rotation.

(b) The concentration ratio is limited by the minimum segments width attainable.

(c) Geometric losses, or losses due to the space between segments, can be significant.

4. The minimization of energy losses due to absorption by the reflective surface of the concentrator and due to reflection from transparent insulations of the receiver is very important.

5. Of the concentrator-receiver systems tested, and for the temperature range of the program most suited for applications, the unevacuated acrylic tube system is superior in performance.

6. For low temperature applications as exemplified by this work, receivers without evacuated jackets can be fabricated that will perform with reasonable efficiencies.

Recommendations

Segmented Plane Concentrator

Many of the design parameters for solar energy concentrators are a strong function of the desired application. However, there are several parameters peculiar to the segmented plane concentrator which can be evaluated so as to be applicable to its design for any application. For instance, an in depth evaluation of the geometric loss parameter is needed. The variables of such an investigation should include the overall width of the concentrator, the position of the receiver with respect to the concentrator, the segment width, the spacing between segments, the tilt of the concentrator, the orientation of the concentrator, i.e., linearly east to west or north to south, and the full range of the sun's altitude and azimuth for the whole year at any latitude. Only with the aid of a computer would such a study be feasible.

Although the four bar parallel linkage system appeared

best for the experimental concentrator, it is possible that other types of tracking mechanisms would be best suited for larger systems. For instance, it might be best in the largest systems to have the segments rotated by groups, or even to have each segments independently rotated by individual drive motors. Therefore, a study of the best type of segment rotation system for residential, commercial, and power plant size concentrator systems is needed. This study should be coordinated with the design of an automatic control system for tracking.

Receiver Design

It is obvious that the vacuum shrouded receiver could be thermally the most efficient; thus, further effort to economically fabricate such a receiver is warranted. The main problem encountered with this type of receiver in the experimental program was that the difference in the thermal expansion of the inner pipe and the outer acrylic tube made it difficult to have adequate seals between the two. Several alternatives exist; for instance, if both the fluid inlet and outlet to the receiver were on the same end, and if the inner tubes were freely positioned within the outer tube, thermal expansion would be no problem and ordinary mechanical seals on the one end would be satisfactory.

This program has demonstrated that for low temperature applications, an adequately efficient receiver is possible without a vacuum jacket. Therefore, the design of this type

of receiver should also be pursued. Improvement over the receiver designs of the experimental program can be achieved by using transparent insulations with better insulating properties, and higher optical ratios. In addition, the insulating properties of thin air gaps could be better utilized. Also, design of a receiver with less fluid volume would increase the fluid velocity. This increase in velocity would in turn increase the efficiency of heat transfer to the fluid. The increased velocity would also reduce the mean temperature of the receiver, which would thus reduce the heat losses.

Further experimental evaluation of carefully designed receivers can be economically accomplished. Therefore, such evaluations are strongly encouraged, because the eventual success of solar concentrator applications will depend strongly on the economical design of an efficient receiver.

Concentrator-Receiver System Considerations

Several points were realized during this program which are applicable to all types of concentrator-receiver systems and which deserve future consideration. For a given concentrator width, increasing the concentration ratio can be accompanied by a decrease in the receiver diameter, thus reducing the heat loss area. Also, for a given concentrator area, if the width of the concentrator is increased, the lengths of the concentrator and receiver are also decreased and again the heat loss area is reduced.

For the experimental program, a movable receiver was employed to compensate for the translation of the composite image along the axis of the receiver. However, for actual applications, this would be impractical and thus attention should be directed toward finding suitable alternatives. For long concentrators, where the amount of the image that would travel off the end of the receiver is small in comparison with the total receiver length, both east to west and north to south orientations would be acceptable. For small concentrators, however, north to south orientation would probably be best suited because with that orientation, less image travel is encountered. Also, having a receiver that is sufficiently longer than the concentrator so that the image never travels off the receiver might be feasible for north to south orientation, but this approach must be weighed against the amount of additional heat loss that would be encountered by increasing the receiver length.

The design of any type of reflective concentrator should include careful selection of the primary surface material. The material selected should have as high a reflectivity as possible consistent with workability, durability and economic considerations.

Instrumentation and Procedure

Further evaluations similar to that of this work should include a study of the temperature profile of the receiver

surfaces to facilitate thermal analysis. Also, it would be better to take the average of the wind velocity over a five minute period up to the time data is taken, rather than the one minute period used in this work. It is also recommended that whenever possible, a pyrheliometer or similar device be used to actually measure the direct radiation intensity instead of calculating the intensity as done in this work.

APPENDICES

APPENDIX A

GEOMETRIC RELATIONSHIPS

The purpose of this appendix is to provide a more thorough description of various geometric relationships relative to the working principle and design of the segmented plane solar concentrator.

Resolution of the Solar Flux

A study of the geometric relationships is dependent upon an understanding of the motion of the sun relative to the earth and is greatly facilitated by resolving the solar flux into convenient components. There are several means by which the position of the sun may be specified.[25] The means most useful for this work is to specify the south solar azimuth, α_s, and the solar altitude, β, as shown in Figure 20. Also shown in Figure 20 are the components of a solar flux line normal and parallel to the east-west and north-south axes. In addition, Figure 20 defines the angles ψ, θ, and γ, which aid in this work. Values of these angles may be calculated from the following equations:

$$\theta = \text{Arctan}[\cot\beta \sin(\tfrac{\pi}{2} - \alpha_s)], \tag{12}$$

$$\gamma = \text{Arccos}[\sin\beta/\cos\theta], \text{ and} \tag{13}$$

α_s – SOUTH SOLAR AZIMUTH

β – SOLAR ALTITUDE

$\overline{CO}$ – TYPICAL SOLAR FLUX LINE

$\overline{CD}$ – COMPONENT OF FLUX LINE PARALLEL TO E-W AXIS

$\overline{CF}$ – COMPONENT OF FLUX LINE PARALLEL TO N-S AXIS

$\overline{CG}$ – COMPONENT OF FLUX LINE PERPENDICULAR TO N-S AXIS

$\overline{CB}$ – COMPONENENT OF FLUX LINE PERPENDICULAR TO E-W AXIS

θ – ANGLE BETWEEN VERTICAL AND $\overline{CB}$

ψ – ANGLE BETWEEN VERTICAL AND $\overline{CG}$

γ – ANGLE BETWEEN FLUX LINE AND $\overline{CB}$

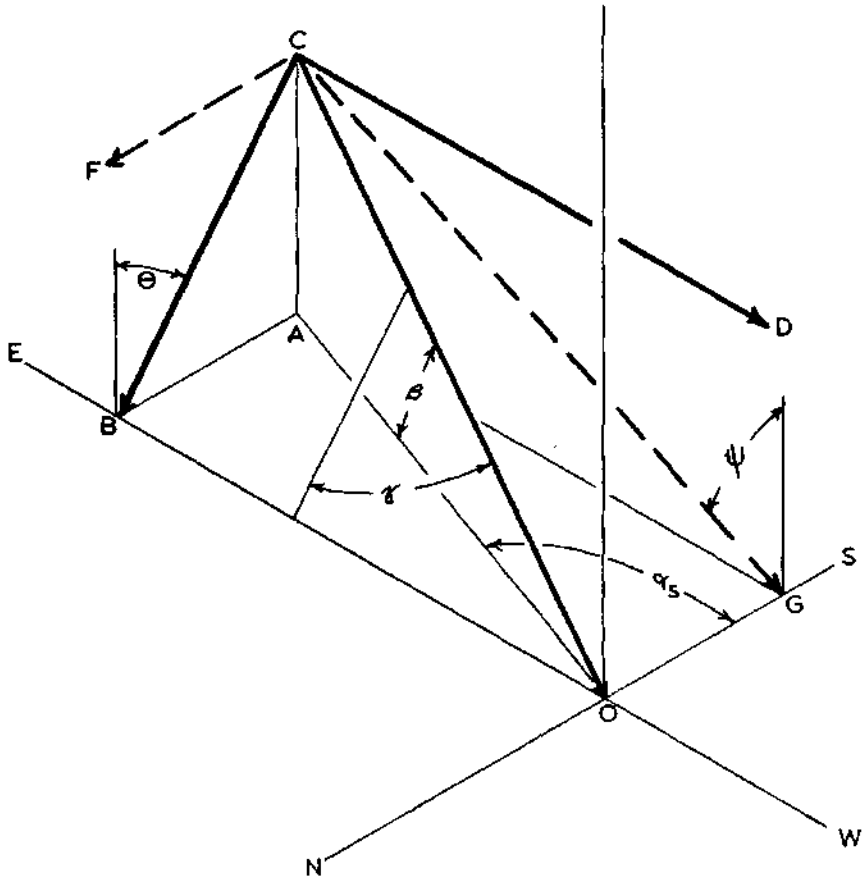

Figure 20. Resolution of the Solar Flux and Definition of Angles

$$\psi = \frac{\pi}{2} - \text{Arctan}[\tan\beta/\sin\alpha]. \qquad (14)$$

Using these equations and values of solar altitude and azimuth interpolated from the ASHRAE Handbook of Fundamentals,[26] Figures 21, 22, and 23 were developed which show the variation of θ, γ, and ψ as a function of the season and solar time for Atlanta, Georgia.

Focusing Relationship

This analysis of the focusing relationship is similar to that presented by Russel[27] for a segmented cylindrical concentrator. Figure 24 shows the focusing relationship for a typical concentrator and receiver, and is applicable to both north-south and east-west orientations by use of the appropriate value of σ as defined in the figure. An incident solar flux line, $\overline{SO}$, resolved into component $\overline{SE}$, parallel to the segments, and $\overline{SO}'$, perpendicular to the axis of the segment, is depicted in the figure. If the segment is oriented at the angle ρ_n with the horizontal, component $\overline{SO}'$, at angle of σ with the vertical, would then be reflected at angle $(2\rho_n + \frac{\pi}{2} - \sigma)$; the parallel component, $\overline{SE}$, would not be altered. Therefore, the reflected beam, $\overline{OD}$, is composed of two components; $\overline{CD}$, equal and parallel to $\overline{ES}$, and the other, $\overline{OC}$, equal in magnitude to $\overline{SO}'$, but perpendicular to the axis at angle $(2\rho_n + \frac{\pi}{2} - \sigma)$ with the horizontal. If the reflected beam, $\overline{OD}$, is to be incident upon the receiver, the position

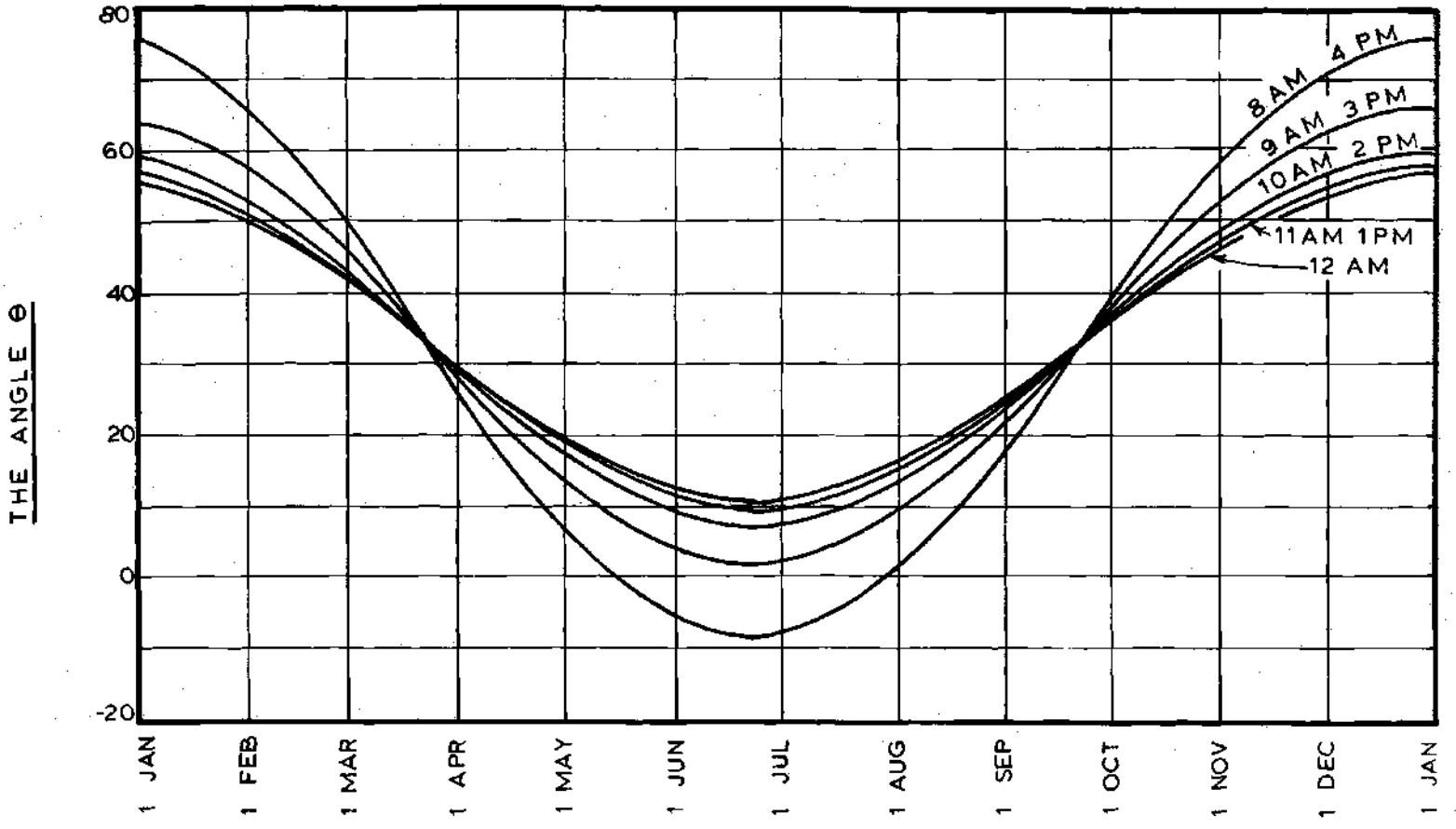

Figure 21. Variation of the Angle θ for 33°-45' Latitude

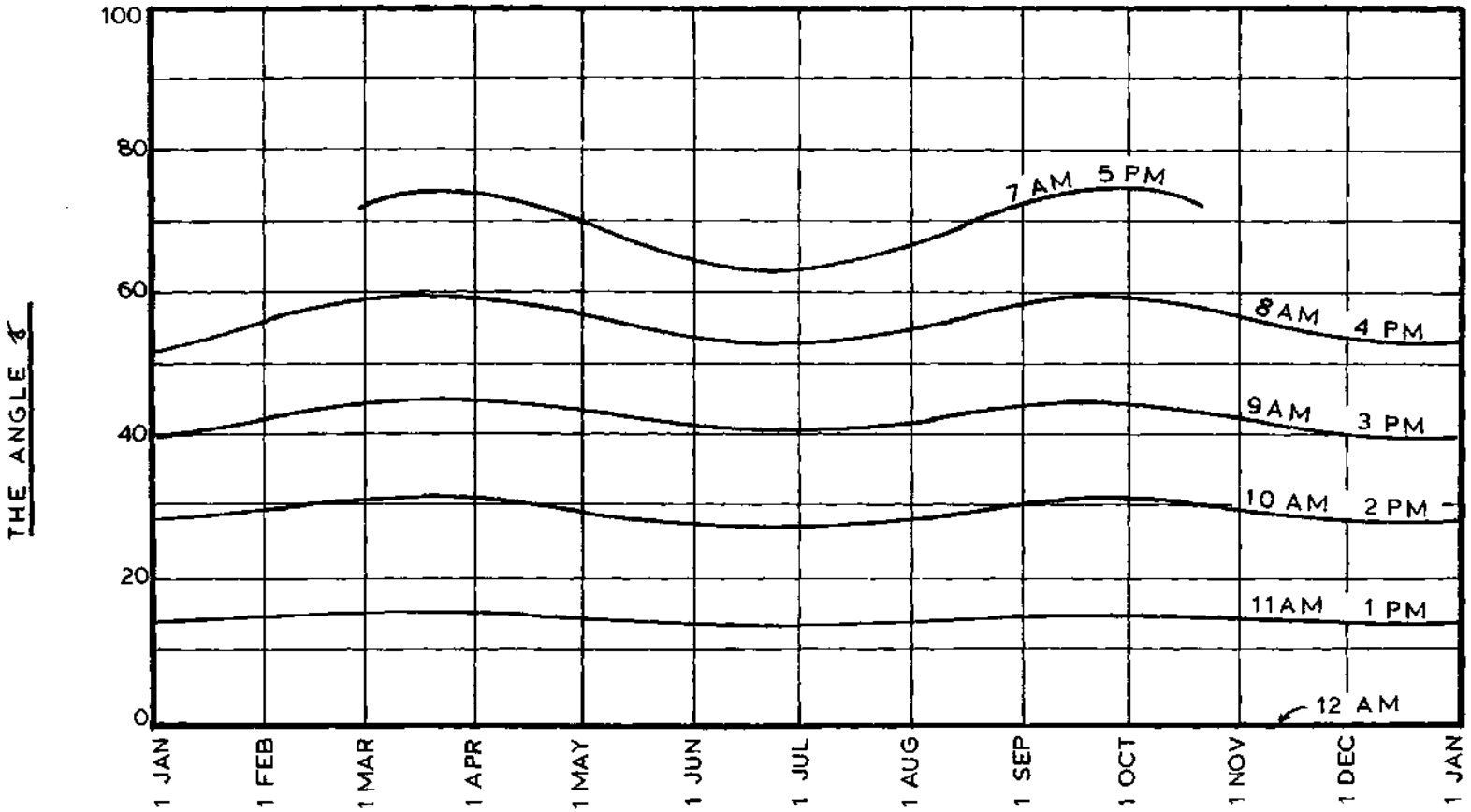

Figure 22. Variation of the Angle γ for 33°-45' Latitude

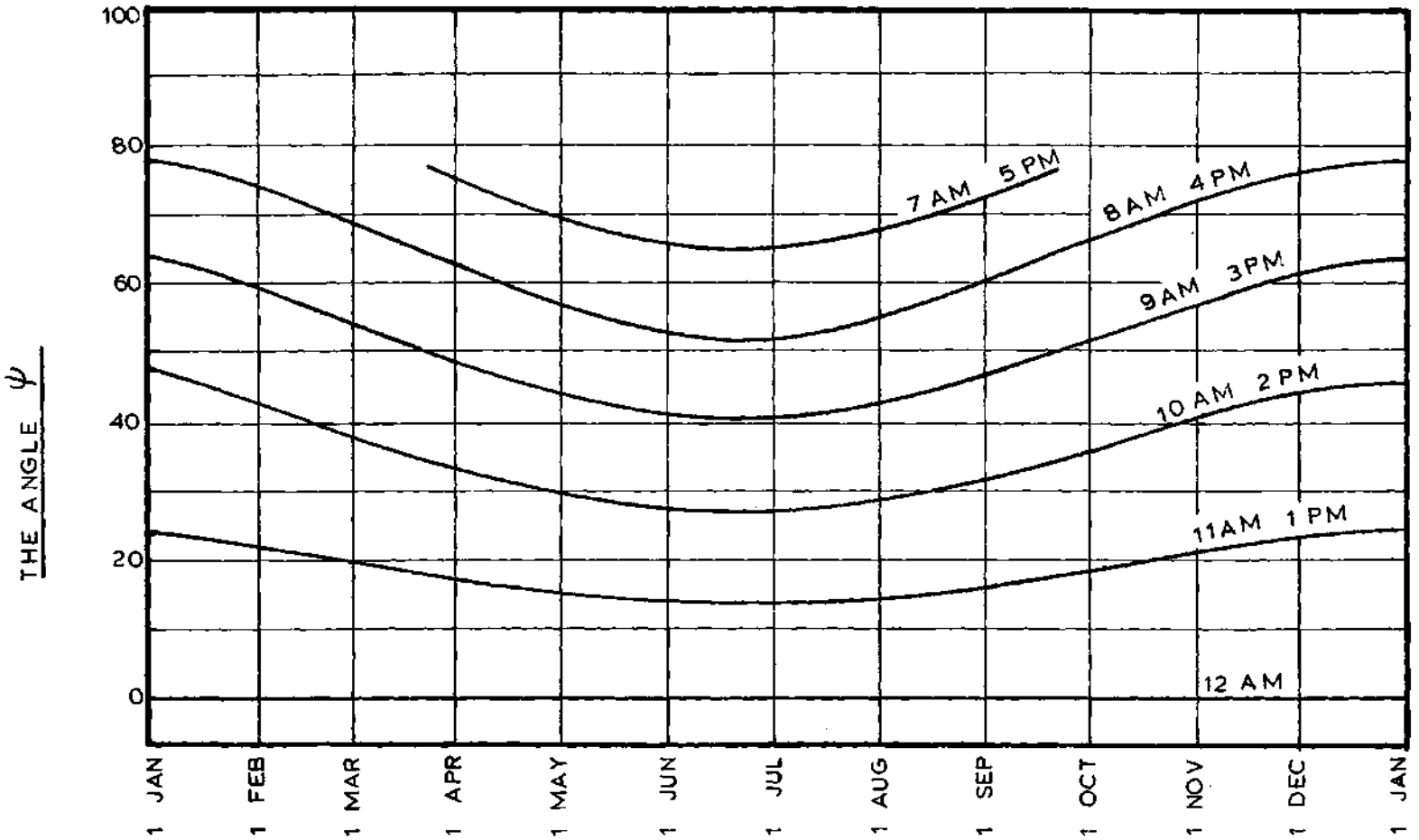

Figure 23. Variation of the Angle ψ for 33°-45' Latitude

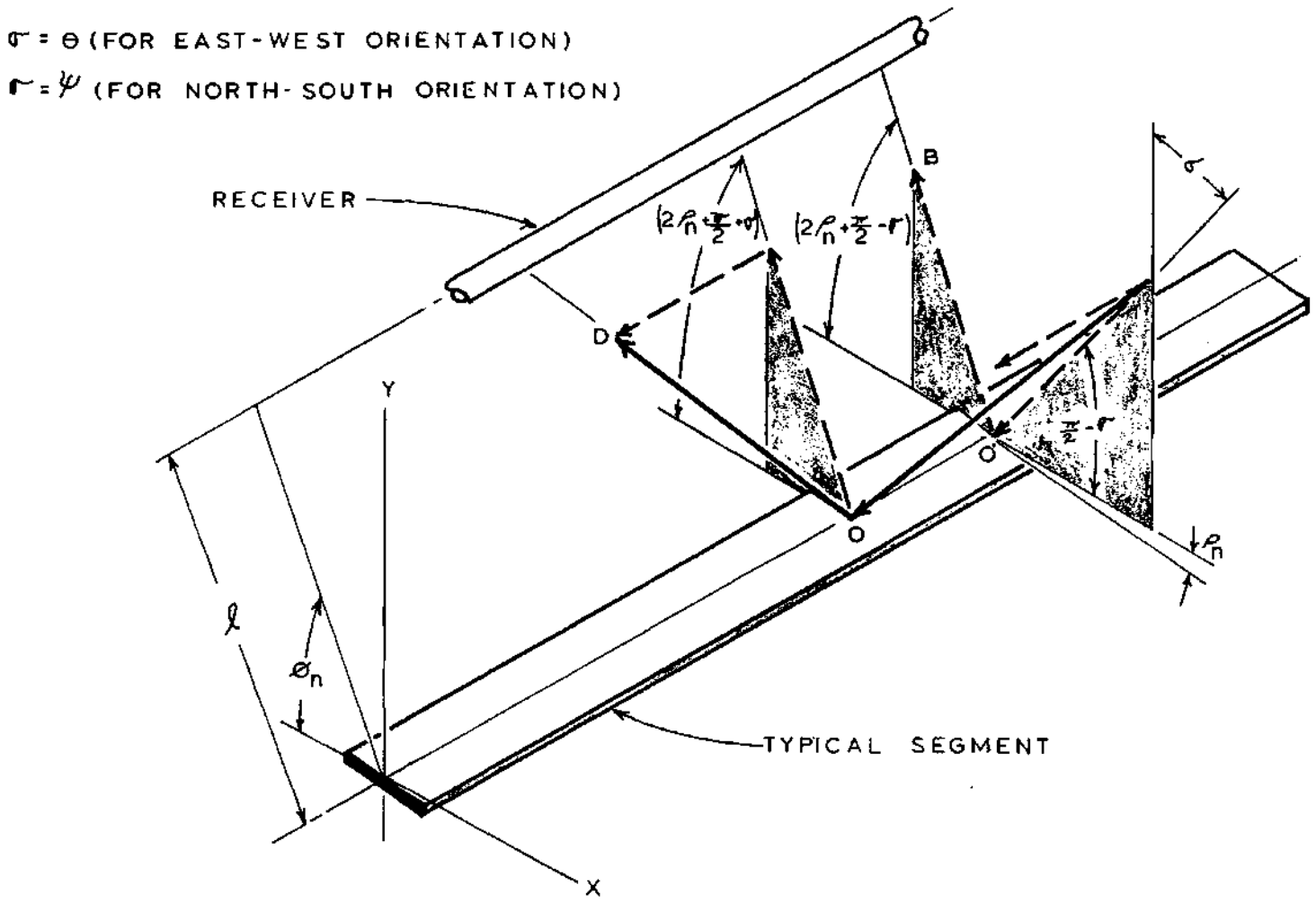

Figure 24. Focusing Relationship for a Typical Segment

of which is defined by ℓ and ϕ_n, then the segment must be so rotated as to satisfy the relation

$$\rho_n = \frac{\sigma}{2} + \frac{\phi_n}{2} - \frac{\pi}{4}. \tag{15}$$

Accordingly, for proper focusing, each segment of a segmented plane concentrator must be rotated so as to satisfy equation (15). Since ρ is a function of σ and ϕ, both of which lie in a plane normal to the axis, focusing and tracking can be analyzed by use of a two dimensional drawing such as that in Figure 25. By mentally moving the receiver of Figure 25, it can be seen that the receiver need not be centered above the concentrator in order for each segment to be focused.

Tracking Relationship

Since the receiver is fixed relative to the axis of each segment for a given concentrator-receiver system, it follows that ϕ is constant for each segment. Therefore, the relationship

$$\frac{\partial \rho}{\partial \sigma} \Big|_{\phi} = 1/2, \tag{16}$$

the partial derivative of equation (15), represents the variation of ρ for all segments necessary to keep the image focused on the receiver as σ changes with time. Therefore, if σ increases by 10°, for instance, then tracking is

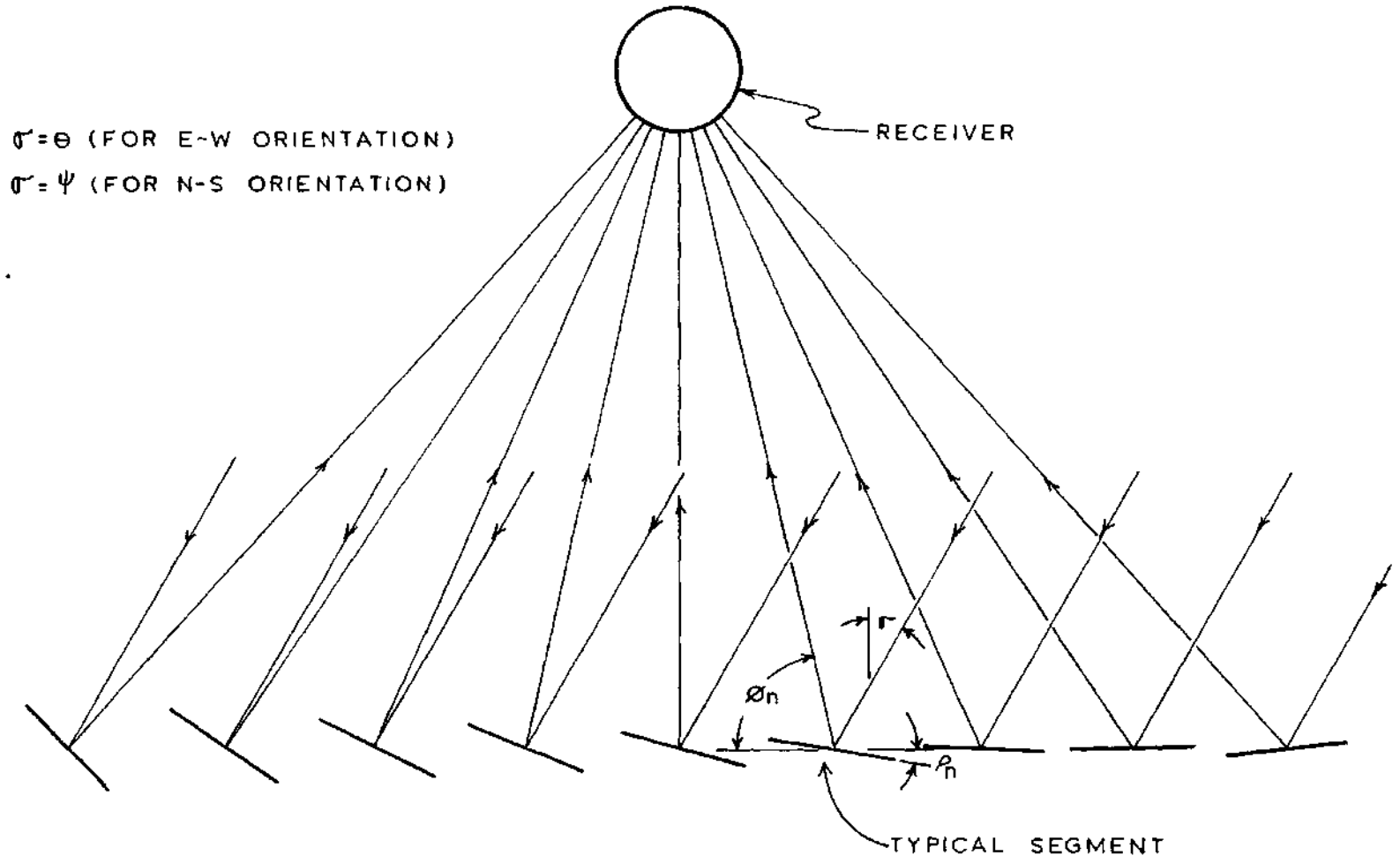

Figure 25. Two Dimensional Diagram of Focusing Relationship

accomplished by rotating all segments clockwise by 5°. Comparison of Figures 21 and 22 reveals that tracking for east to west concentrator orientation requires less rotation of the segments than is required for north to south orientation.

Edge, Shading, and Gap Losses

There are three modes by which portions of the energy incident upon the plane of a concentrator may be lost due to the positions of the segments. Any combination of these losses may occur for a given segment. Figure 26 depicts a situation where all three modes occur at the same time. Shading losses are equal to that portion of the energy incident upon the plane of the concentrator which is reflected by a segment, but which is prevented from hitting the receiver due to shading by the adjacent segment. Edge losses equal that portion of the energy incident upon the plane of the concentrator which will not be incident upon a segment because the segments are at an angle ρ_n with the horizontal. Gap losses are equal to that portion of the energy incident upon the plane of the concentrator which will not be incident upon any segment because of the gap width between segments. Figure 27 depicts a situation where the segment width and spacing are the same as that in Figure 26, but a different incident angle of the solar flux and a different receiver position relative to the segment results in no loss of incident energy. The only inefficiency involved is that a

S -SHADING LOSSES

G -GAP LOSSES

E -EDGE LOSSES

L_g - TOTAL GEOMETRIC LOSSES

S_p - SPACING BETWEEN SEGMENTS

L_g/S_p - AREA LOSS RATIO

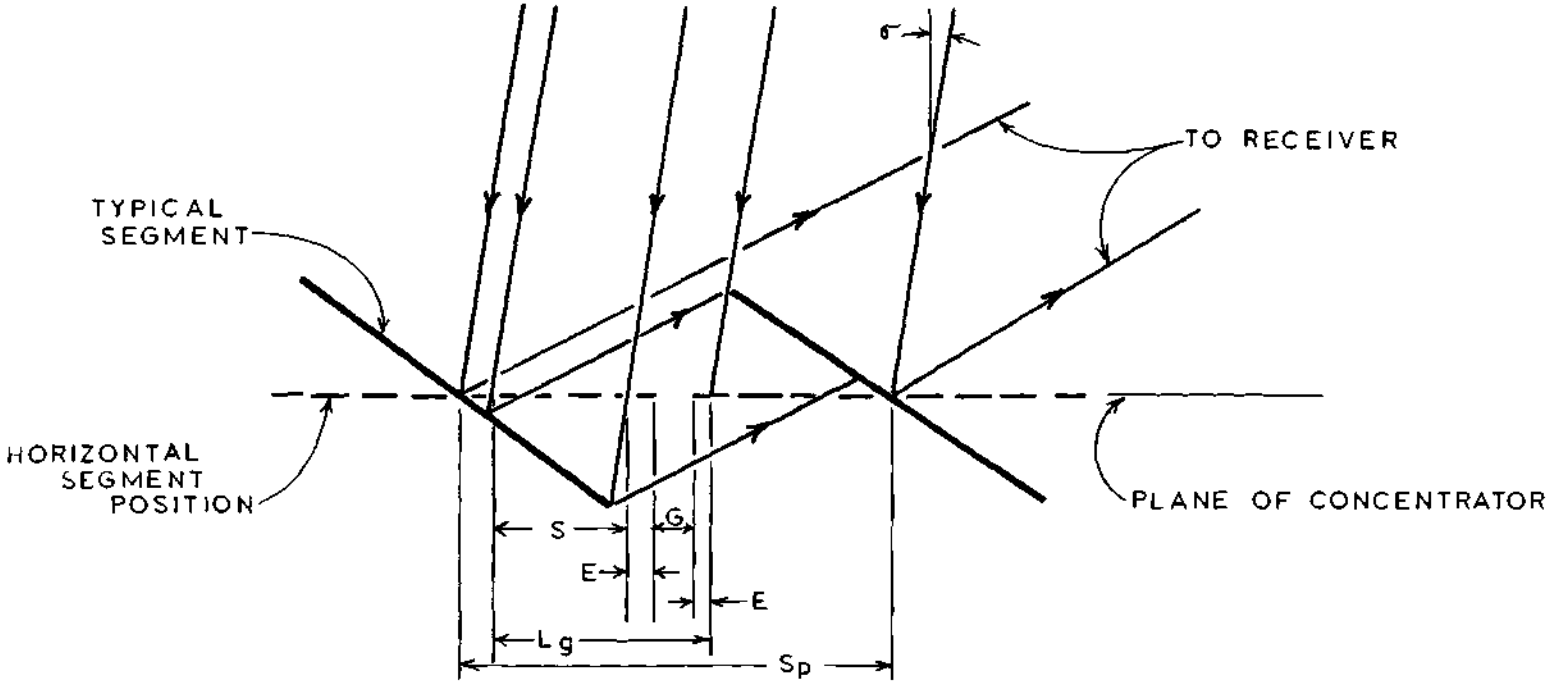

Figure 26. Explanation of Geometric Losses

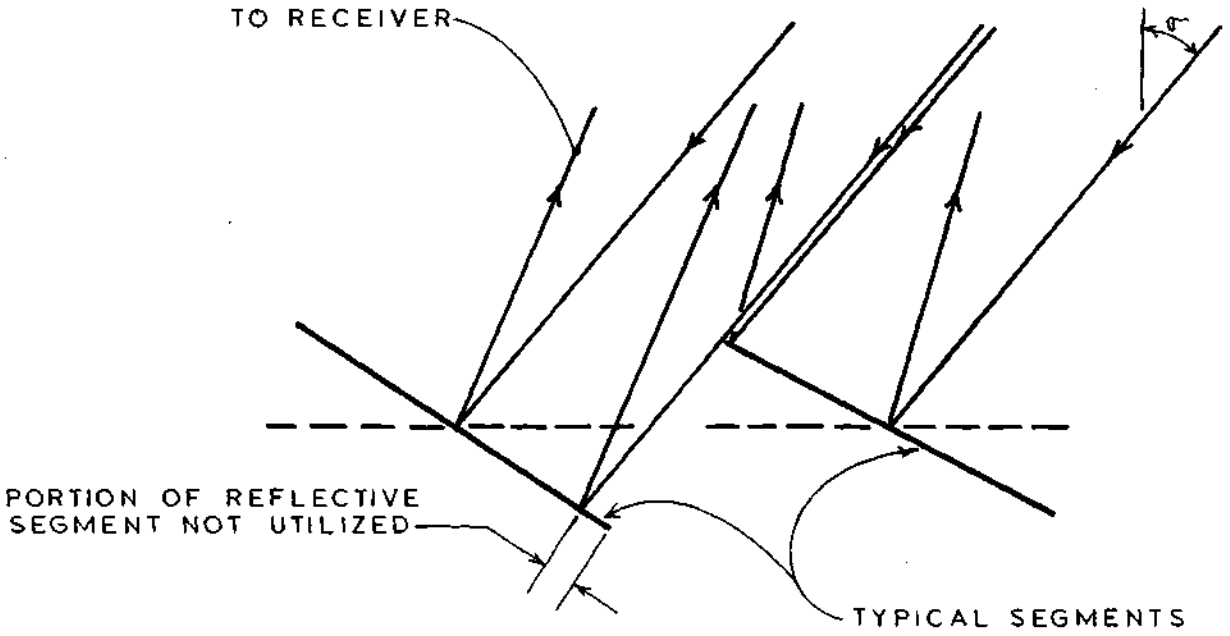

Figure 27. Position of Segments and Receiver for No Geometric Losses

portion of the segment's reflective area is not being utilized.

As can be seen, these three modes are a function of the ratio of the segment width to the segment spacing, the position of segments relative to the receiver, the incident angle of the solar flux, and the angle formed between the horizontal and the plane of the concentrator, shown in Figures 26 and 27 as zero, for simplicity. The combined effect of all three types of losses described here is called the geometric losses, L_g, as shown in Figure 26.

For the analysis of Chapter IV, it is necessary to know the amount of geometric losses encountered under various specified conditions. This task was accomplished in this work by drawing to scale a cross sectional view of all segments in their focused positions for the specified angle of incidence. Incident and reflected solar flux lines were also placed on the drawings so that the geometric losses for each segment could be graphically measured in the same manner indicated in Figure 26. An interesting fact was determined by following this procedure for the concentrator of this program in a horizontal position, and the receiver at the standard height: By evaluating the geometric losses for several values of θ, it was determined that as long as θ is greater than 35°, geometric losses either don't occur or are negligible. A look at Figure 21 reveals, therefore, that any geometric losses encountered during the standard height

tests of this program which lasted until March 14, 1974, were negligible. It should be emphasized that the 35° limitation mentioned above applies only to the concentrator-receiver system described. However, similar limitations would exist for other systems. In this work, when determining the geometric losses where the receiver shaded the concentrator, as in the tilted concentrator test, the geometric losses were taken as being equal to the geometric losses for an unshaded concentrator multiplied by the ratio of the unshaded segments to the total number of segments.

Travel and Variable Length of Image

Figure 23 graphically displays the variation of the angle γ through each day of the year, and Figure 28 shows the relationship between γ and the travel of the composite image along the axis of the receiver. The incident flux shown is typical of mid-morning in early December. As depicted, the distance x will decrease until solar noon, when γ and x are zero. During the afternoon hours, x will be negative and will extend toward the east from point A.

Because the perpendicular distances from corresponding points on each segment to the receiver are different, the reflected beams from those points fall at different values of x along the receiver. The distance Y in Figure 28 shows the difference for segment-1 and segment-2. Therefore, the composite image length increases in proportion to the time

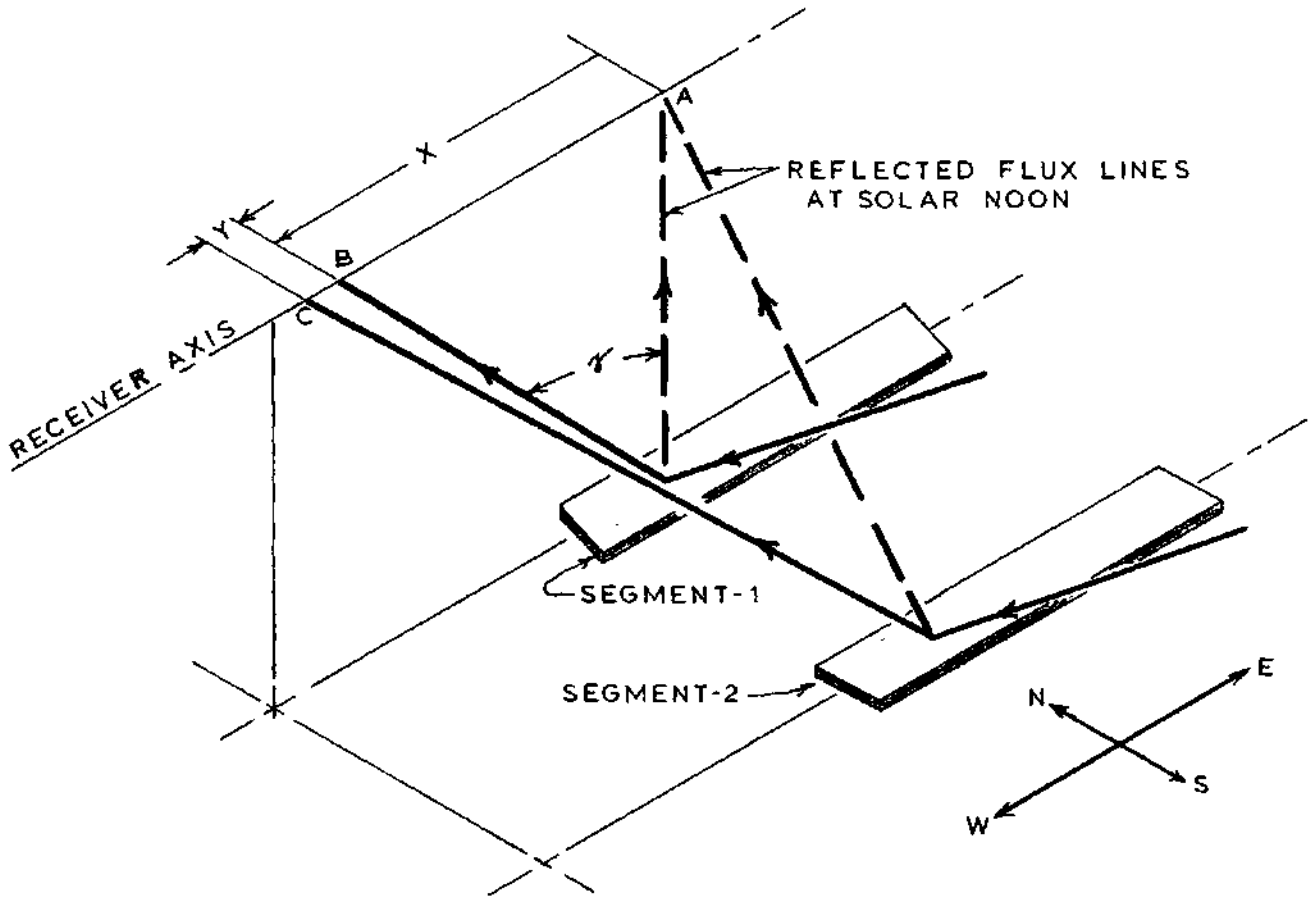

Figure 28. Travel and Length of Composite Image

before and after solar noon. Solar noon is the only time when the length of the composite image equals the segment length.

The position of the image along the centerline of the receiver, and its length, can be calculated by using basic trigonometric relationships and Figure 23, if the position of the receiver relative to each segment and the solar time is known. The same procedure applies for north to south orientation if the angle between the incident flux line and a line perpendicular to the north-south axis is substituted for γ. During the standard height tests of the experimental program, the composite image traveled about three feet between 12 noon and 3 p.m. solar time. During that same period, the length of the composite image increased about six inches. It should be pointed out that if the receiver is not centered over the concentrator, the composite image will be longer for the same height above the concentrator. This will occur because moving the receiver away from the centered position increases the distance from the receiver to the farthest segment, as can be seen in Figure 28.

APPENDIX B

DEVELOPMENT AND APPLICATION OF A PROCEDURE FOR CALCULATING THE DIRECT NORMAL SOLAR RADIATION INTENSITY FOR ATLANTA, GEORGIA

Introductory Remarks

This appendix provides an explanation of the derivation of values for direct normal radiation intensity used in this work, an expedient method for determining such values for Atlanta, Georgia, for future reference, an explanation of the use of the method, and a starting point for further study and improvement upon the procedure.

This presentation is an adaptation of the general procedure due to Threlkeld and Jordan.[28] Their procedure, vis-a-vis several others, is easily applied without severe compromise of accuracy, it being essentially an extension of Moon's[29] work. The procedure is applicable only on clear days and gives values of direct normal radiation intensity only. Direct normal radiation is the solar flux passing directly through the atmosphere and incident upon a surface normal to the flux at the earth's surface, as opposed to the total radiation, which is the sum of the direct normal radiation and any diffuse sky radiation incident upon the same surface.

The basic procedure is to multiply the solar intensity at the outer limit of the atmosphere, I_A, by the total transmissivity of the atmosphere, τ_A,

$$I_{DN} = I_A \cdot \tau_A, \tag{17}$$

where I_{DN} is the direct normal radiation intensity at the earth's surface.

Development of Procedure

Intensity at the Outer Limit of the Atmosphere

The amount of solar radiation incident upon a surface normal to the solar flux at the outer limit of the atmosphere when the earth is at its mean distance from the sun, is called the solar constant, I_o. Johnson[30] estimates the solar constant to be equal to 442.4 Btu/hr/ft^2 with a probable error of $\pm$2%. I_A is related to I_o by the expression

$$I_A = R_s I_o, \tag{18}$$

where R_s denotes the ratio of I_A to I_o, and which may be derived from Figure 29 for a specified time of year.

Calculation of Total Transmissivity

The direct solar beam is reduced in intensity as it passes through the atmosphere by absorption due primarily to ozone and water vapor, and by scattering due to molecules of

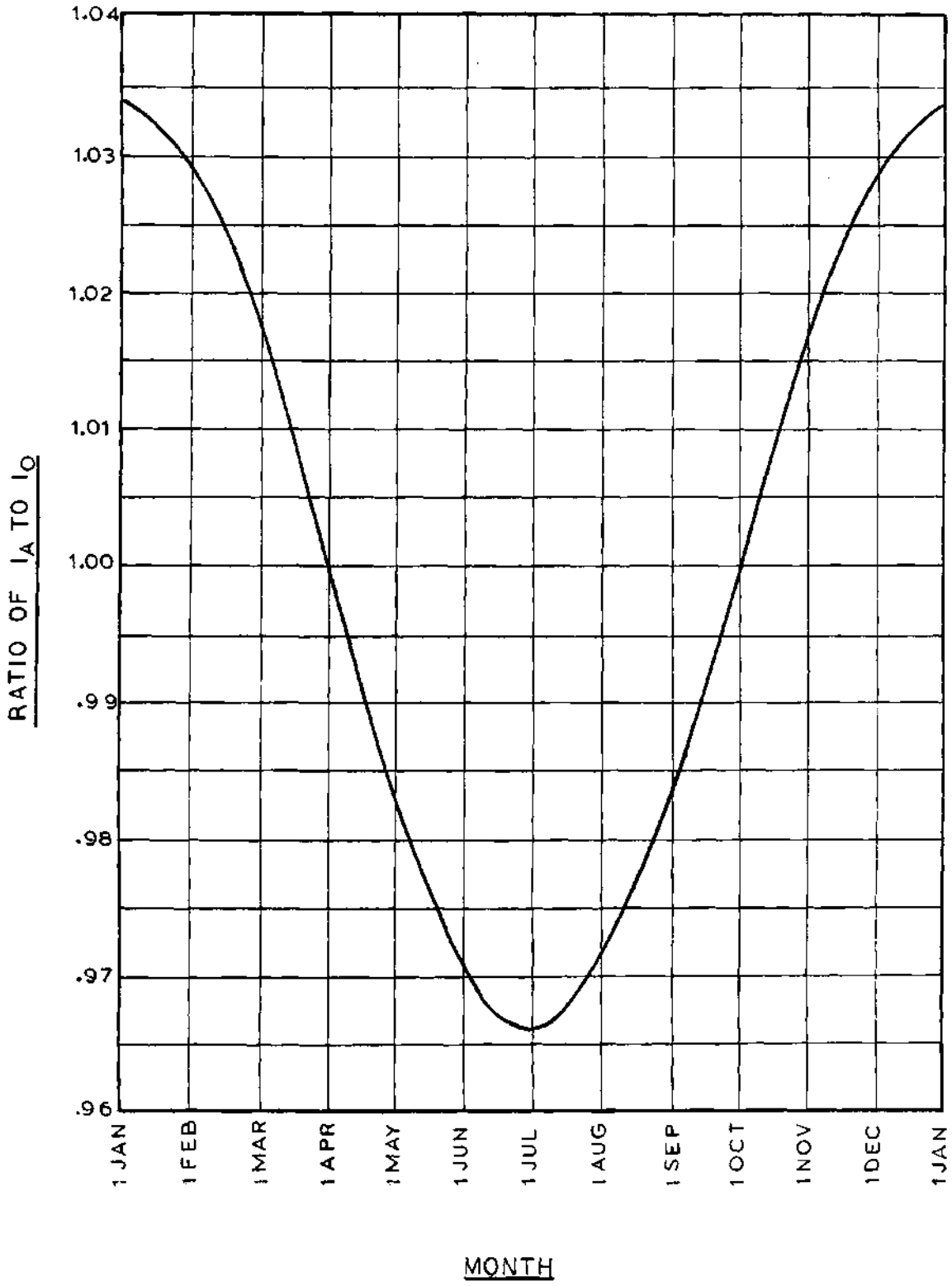

Figure 29. Ratio of the Solar Radiation Intensity At the Outer Limit of the Atmosphere to the Solar Constant

air and water vapor, as well as by scattering due to dust. Regarding each of these effects as being caused by a corresponding layer of the atmosphere, the total transmissivity of the atmosphere at a given wavelength and unit air mass may be expressed as

$$\tau_{\lambda,m=1} = \tau_{A'S_\lambda} \cdot \tau_{WS_\lambda} \cdot \tau_{DS_\lambda} \cdot \tau_{WA_\lambda} \cdot \tau_{OA_\lambda}, \qquad (19)$$

where τ indicates transmissivities; A and S refer to absorption and scattering respectively; D, A', O, and W refer to dust, air, ozone, and water vapor, respectively; λ indicates spectral dependence; and the term air mass, m, refers to the ratio of the length of the path of a solar beam passing through the atmosphere to the length that would exist if the beam passed through the atmosphere normal to the earth's surface. Equation (19) cannot be practically used, however, because it is only applicable for unit air mass and because, in order to solve equation (19), values of spectral transmissivity for the amount of water vapor, air, dust, and ozone in the specific atmosphere must be known. Therefore, Moon[29] proposed that the Bouquer[31,32] relationship be assumed valid for each transmissivity layer. The Bouquer relationship states that the ratio of the intensity of a beam leaving a layer, to the intensity of the beam entering, is geometrically proportional to the length of the path traveled. Moon[29] made this proposal so that equation (19) could be expressed in

terms of the known transmissivities and thicknesses of the layers of a hypothetical reference atmosphere. Moon[29] represented the thickness of the reference layers of air, dust, water vapor, and ozone by an atmospheric pressure of 760 mm of Mercury, 800 dust particles per cubic centimeter, 20 mm of precipitable water, and 3.8 mm (NTP) of ozone, respectively. Threlkeld and Jordan[28] followed Moon's[29] proposal except that they chose a 2.5 mm (NTP) layer of ozone to represent the reference layer of ozone, and equation (19) became

$$\tau_\lambda = [(\tau'_{A,S_\lambda})^{\frac{a}{760}} \cdot (\tau'_{WS_\lambda})^{\frac{w}{20}} \cdot (\tau'_{DS_\lambda})^{\frac{d}{800}} \cdot (\tau'_{WA_\lambda})^{\frac{w}{20}} \cdot (\tau'_{OA_\lambda})^{\frac{o}{2.5}}]^m, \quad (20)$$

where

a = atmospheric pressure in mm of mercury,

d = the number of dust particles per cm^3,

w = precipitable atmospheric moisture in mm,

o = depth of atmospheric ozone (NTP) in mm,

m = air mass,

and τ' represents the transmissivities of the layers of the reference atmosphere at unit air mass. Using the spectral transmissivity curves and tabulated values of spectral transmissivity for air, ozone, water vapor and dust, by Moon[29] and Fritz[33], Threlkeld and Jordan[28] determined the spectral transmissivities of the layers of the reference

atmosphere. Then they were able, with the aid of equation (20), to plot curves of spectral intensity at the earth's surface such as the lower curve in Figure 30. The upper curve represents the spectral intensity at the outer limit of the atmosphere when the earth is at its mean distance from the sun. Therefore, the area under the upper curve equals the solar constant, and the area under the lower curve equals the direct normal solar radiation at the earth's surface for the atmospheric conditions indicated. The ratio of the area under the lower curve to the area under the upper curve, therefore, is the total atmospheric transmissivity, τ, required in equation (17) for the specified atmosphere and air mass. By assuming sea level elevation and 2.5 mm of ozone to be representative of all general locations in the United States, and using the graphical method just described for calculating atmospheric transmissivity, Threlkeld and Jordan[28] generated families of curves similar to those of Figure 31. Threlkeld and Jordan[28] state that the sea level curves may be used up to 1000 feet with no more than one percent error, and thay they may be used up to 5000 ft with no more than three percent error. Fritz[33] states that 2.5 mm of ozone is representative of all middle latitudes. Therefore, linear interpolation between the plots of Figure 31 for Atlanta, in order to solve equation (17), is permissible where appropriate values of precipitable water vapor and dust particle count are known.

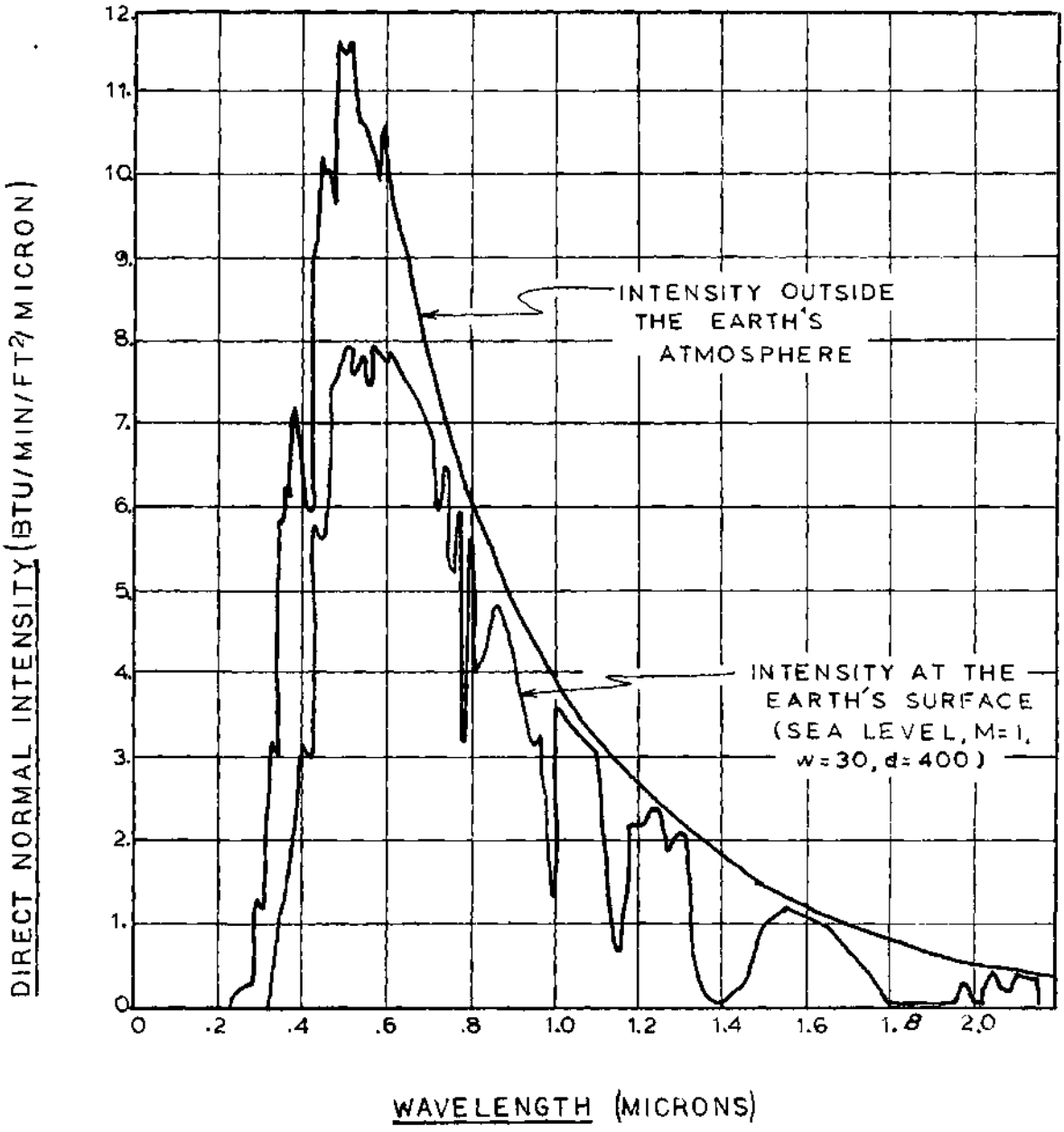

Figure 30. Determination of Atmospheric Transmissivity

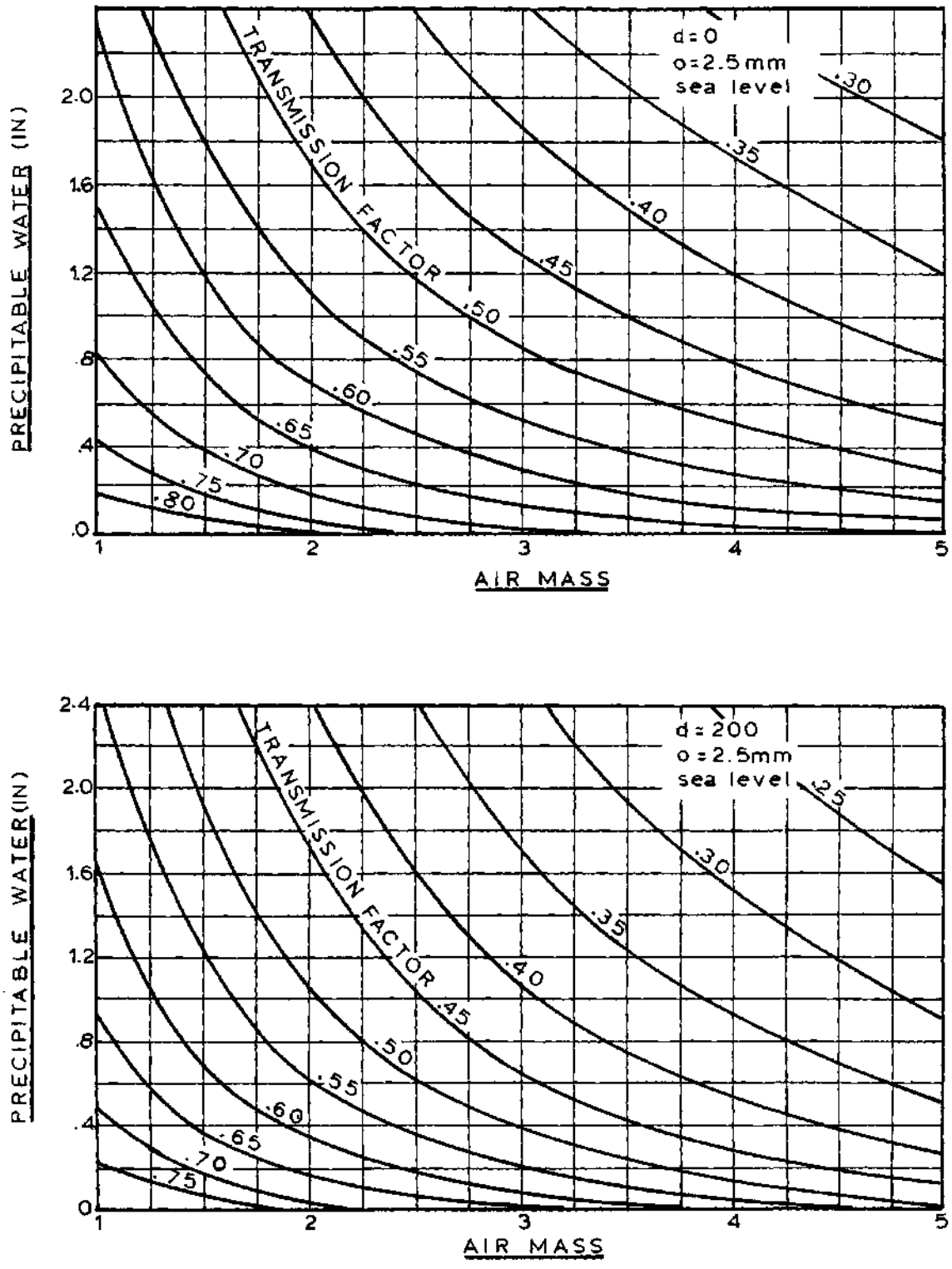

Figure 31. Transmission Factor as a Function of Air Mass, Atmospheric Moisture, and Particulate Pollution

Particle Count and Transmissivity Curves for Atlanta

In developing spectral transmissivity curves, Moon[29] analyzed the atmosphere over Washington, D. C., to determine the spectral transmissivity due to scattering by dust. He then adapted the average dust content of the atmosphere over Washington, D. C., as the content of a hypothetical reference dust layer. To apply the Bouquer relationship to this standard dust layer, an additional parameter was needed to represent the atmosphere's dust content and that of any specified atmosphere as well. Based on a ten year study of the particulate pollution in Washington, D. C., Hand[34] had established an average particle count of 772 particles per cubic centimeter at ground level. Moon[29] approximated this value as 800 particles per cubic centimeter to apply the Bouquer rule and proposed the relation

$$\tau_{DS_\lambda} = [(\tau'_{DS_\lambda})^{\frac{d}{800}}]^m, \qquad (21)$$

which subsequently became a part of equation (20).

The suspended particulate pollution in Atlanta, as in most cities, is measured on a mass per unit volume basis, and therefore no particle count data for Atlanta exists. Thus it is necessary to devise some means of relating the available mass per unit volume data for Atlanta, to the particle count per unit volume scale adopted by Moon[29]. Numerous approaches were attempted to achieve this. The

most practical one, as chosen for this study, is accomplished in three steps as follows: (a) Plot observed direct normal radiation data for cities with differing amounts of suspended particulate pollution. Then on the same axes, plot radiation curves based on calculated values of radiation using various values of dust particle count. A comparison of the curves shows the value of particle count density, d, which best represents each city's suspended particulate pollution. (b) Determine from available pollution records the value on a mass per unit volume basis which represents each city's suspended particulate pollution. (c) Obtain the value on a mass per unit volume basis for the specified area, and linearly interpolate between the values of particle count density found in step (a) to determine the value of particle count density which best represents the specified area.

Threlkeld and Jordan[28] followed step (a) for the cities of Lincoln, Nebraska; Blue Hill, Massachusetts; Madison, Wisconsin; and Washington, D. C. However, they used the average values of radiation intensity on clear days for the years 1933 to 1954, 1911 to 1954, 1910 to 1952, and 1914 to 1936, respectively. Such a long period of years covers a broad range of pollution conditions. In Figure 32, calculated curves by Threlkeld and Jordan[28] for Madison, Wisconsin, and Washington, D. C., are indicated as solid lines. The broken lines represent the mean observed radiation as published by the Weather Bureau[35] for the periods of 1957 to

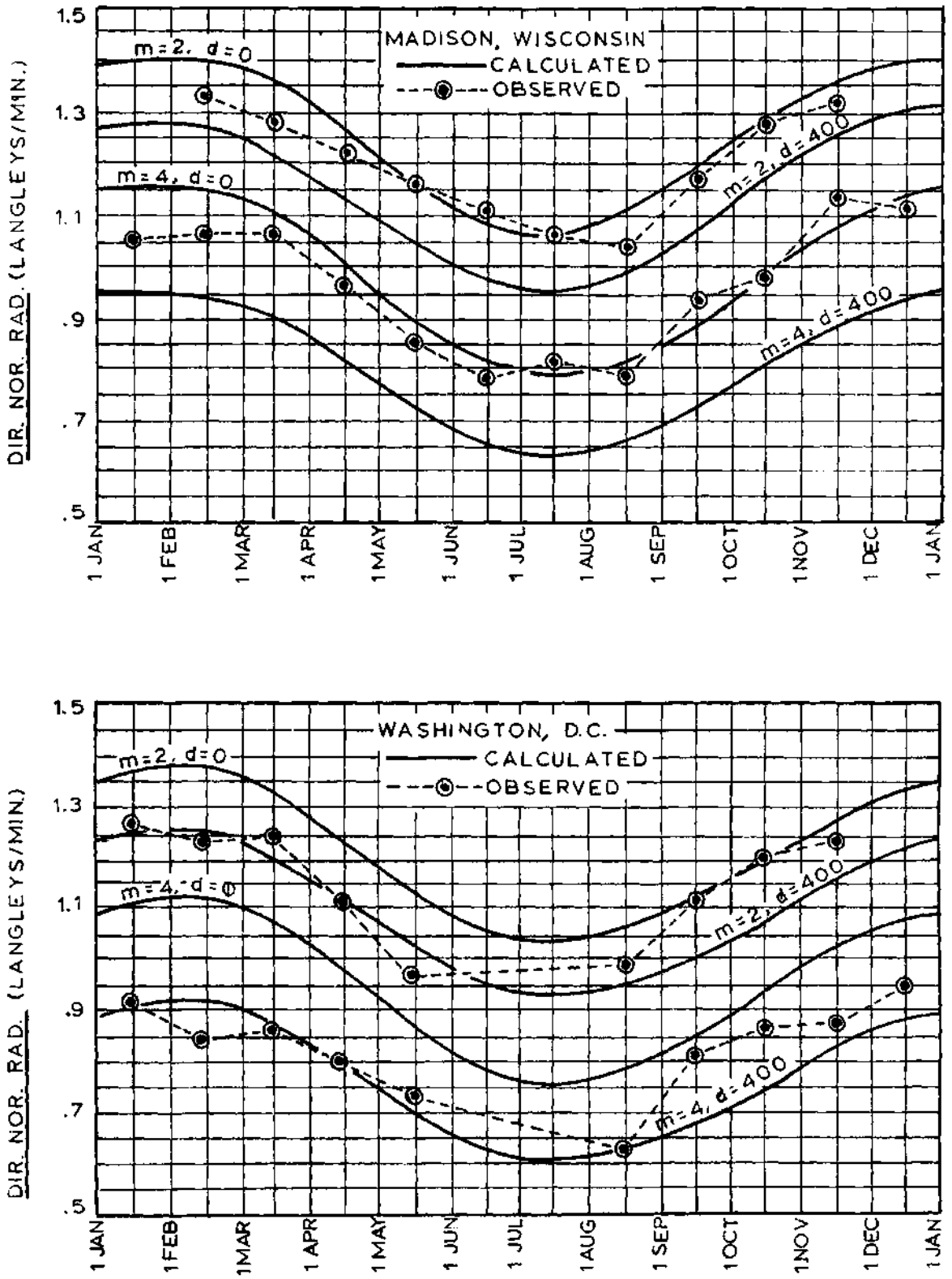

Figure 32. Determination of Particle Count Density for Washington, D. C. and Madison, Wisconsin

1961 and 1954 to 1958, respectively, for the two cities. Following step (a), a comparison of the calculated and observed curves reveals that calculated curves based on annual mean values of d equal to 75 and 300 for Madison and Washington, respectively, correlate well with the mean observed intensity for those cities. Following step (b), the mean value of suspended particulate pollution[36] for Madison and Washington for the periods of 1959 to 1961, and 1958 to 1961, are 88 and 119 micrograms per cubic meter, respectively. The years indicated agree as closely as possible with the periods indicated for the mean observed radiation without use of data from 1957 and before. In 1957, a change was made in the sampling technique used by the National Air Sampling Network[37], and therefore, some error would be introduced in comparing data taken before the changes with current Network samplings for Atlanta. Following step (c), the value of suspended particulate pollution in metropolitan Atlanta[38], measured at the Butler Street sampling station for the years 1970 to 1973 is 98 micrograms per cubic meter. Therefore, linear interpolation as shown in Table 5 below yields a value of particle count density of 148 particles per cubic centimeter as representative of Atlanta's average suspended particulate pollution. Consequently, a value of 150 particles per cubic centimeter is used as the value representing Atlanta's suspended particulate pollution in this work.

Using the value of d equal to 150, Figure 33 was

Table 5. Determination of Particle Count Density for Atlanta

Particulate Pollution (μ_g/m^3)	City	Particulate Pollution (particles/cm^3)
119	Washington	300
98	Atlanta	148 ≈ 150
88	Madison	75

generated by interpolation between the plots of Figure 32. In order to determine the transmissivity of the atmosphere over Atlanta from Figure 33 for any desired value of air mass, the variation of the amount of water vapor in the atmosphere over Atlanta must first be established.

Variation of Atmospheric Moisture Over Atlanta

The upper curve in Figure 34 is a plot of the mean precipitable water in the atmosphere over Atlanta for all days, cloudy and clear, as published by the United States Weather Bureau.[39] The middle curve is a plot of mean precipitable water for clear days only and is arrived at based on the statement by Fritz[40] that the mean precipitable water on clear days is approximately 85 percent of that for all days. The lower curve is the curve assumed by Threlkeld and Jordan[28] for their general procedure applicable anywhere in the continental United States. In their procedure,

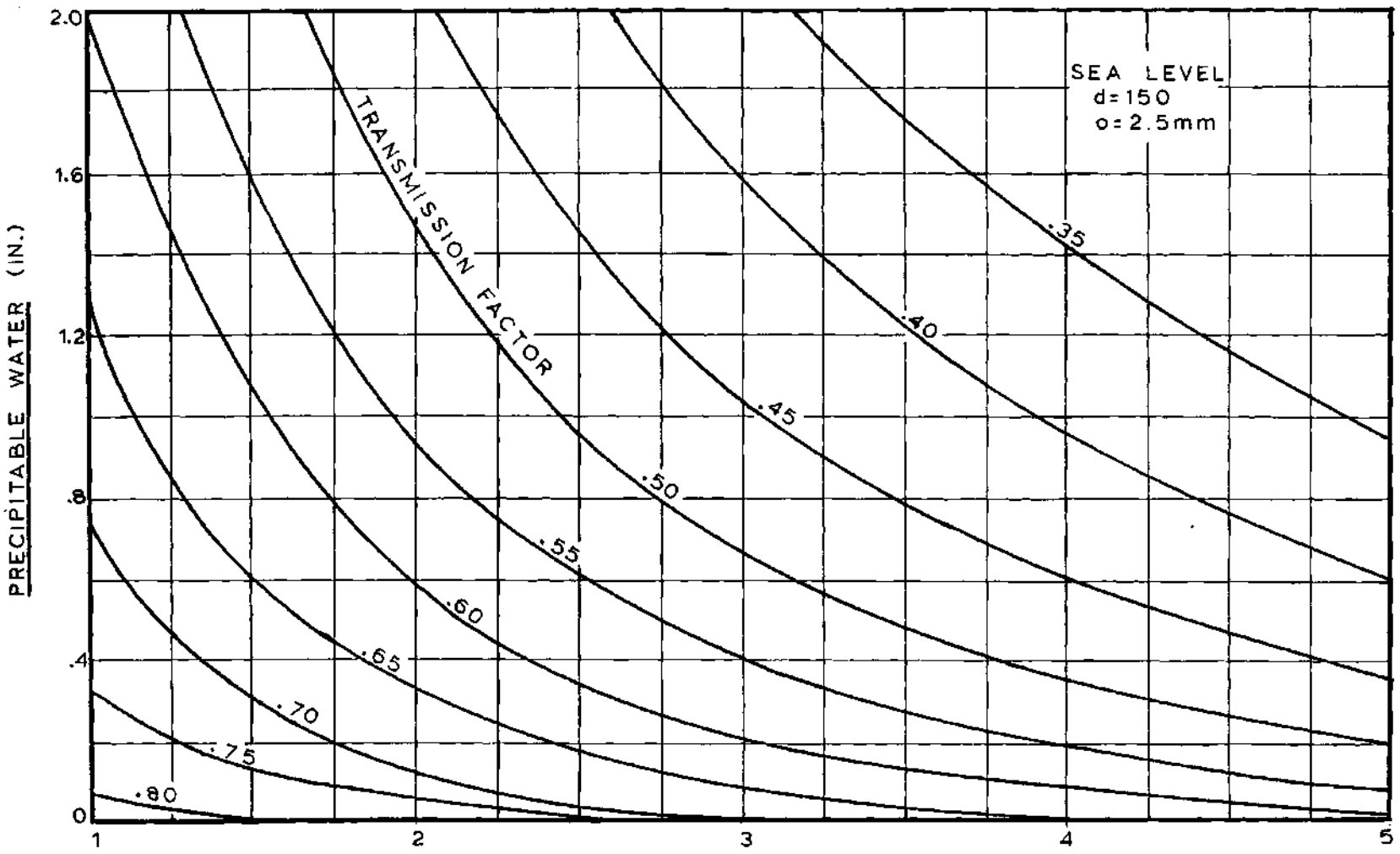

Figure 33. Transmission Factor of the Atmosphere over Atlanta

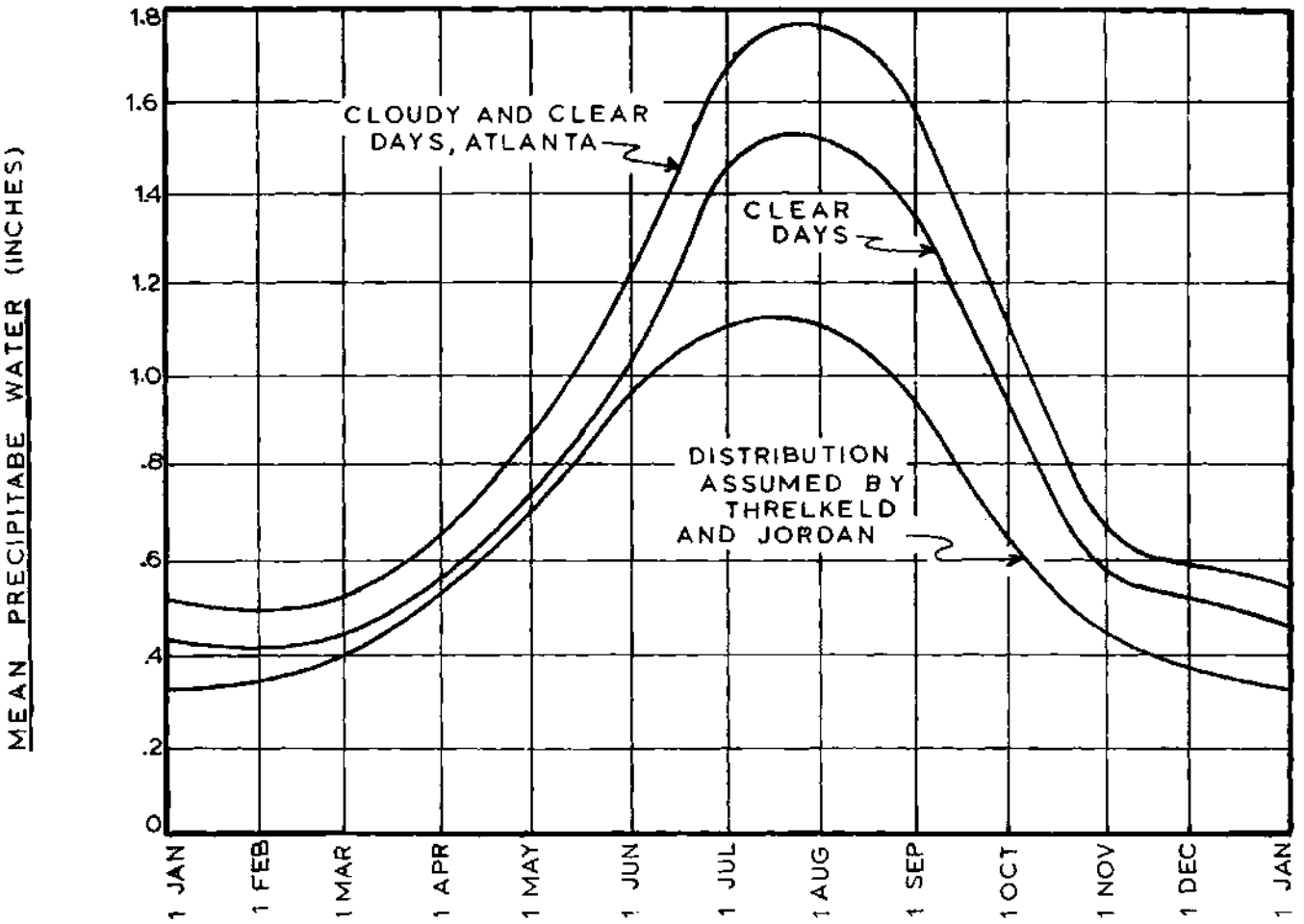

Figure 34. Atmosphereic Moisture in the Atmosphere over Atlanta

deviations from this general distribution for a particular location are compensated for by application of a clearness factor.

Solar Radiation Intensity Curves for Atlanta

With the basic information presented in Figures 33 and 34, along with certain well established relationships, it is possible to calculate the direct normal solar radiation for Atlanta at any hour on any clear day of the year. This operation was performed for the hours between 7 a.m. and 5 p.m. on the twenty first day of each month. The resulting curves are shown in Figure 35. In the following section, several example problems are presented, and the first of these demonstrates the calculations required in arriving at Figure 35.

Figure 36 is a comparison of the radiation intensity curve for 12 a.m. arrived at in this work, with the radiation intensity curves for 12 a.m. by Threlkeld and Jordan's[28] general procedure determined by linear interpolation between their published curves for 30° and 60° latitude. Two of their curves are presented, one with a clearness factor of unity, and one with their recommended clearness factor of .93 for the summer months and .94 for the winter months. As can be seen, Threlkeld and Jordan's[28] curve with a clearness factor of unity correlates best with the curve of this work, rather than their recommended curve with the aforementioned clearness factors. This can be explained by reference to

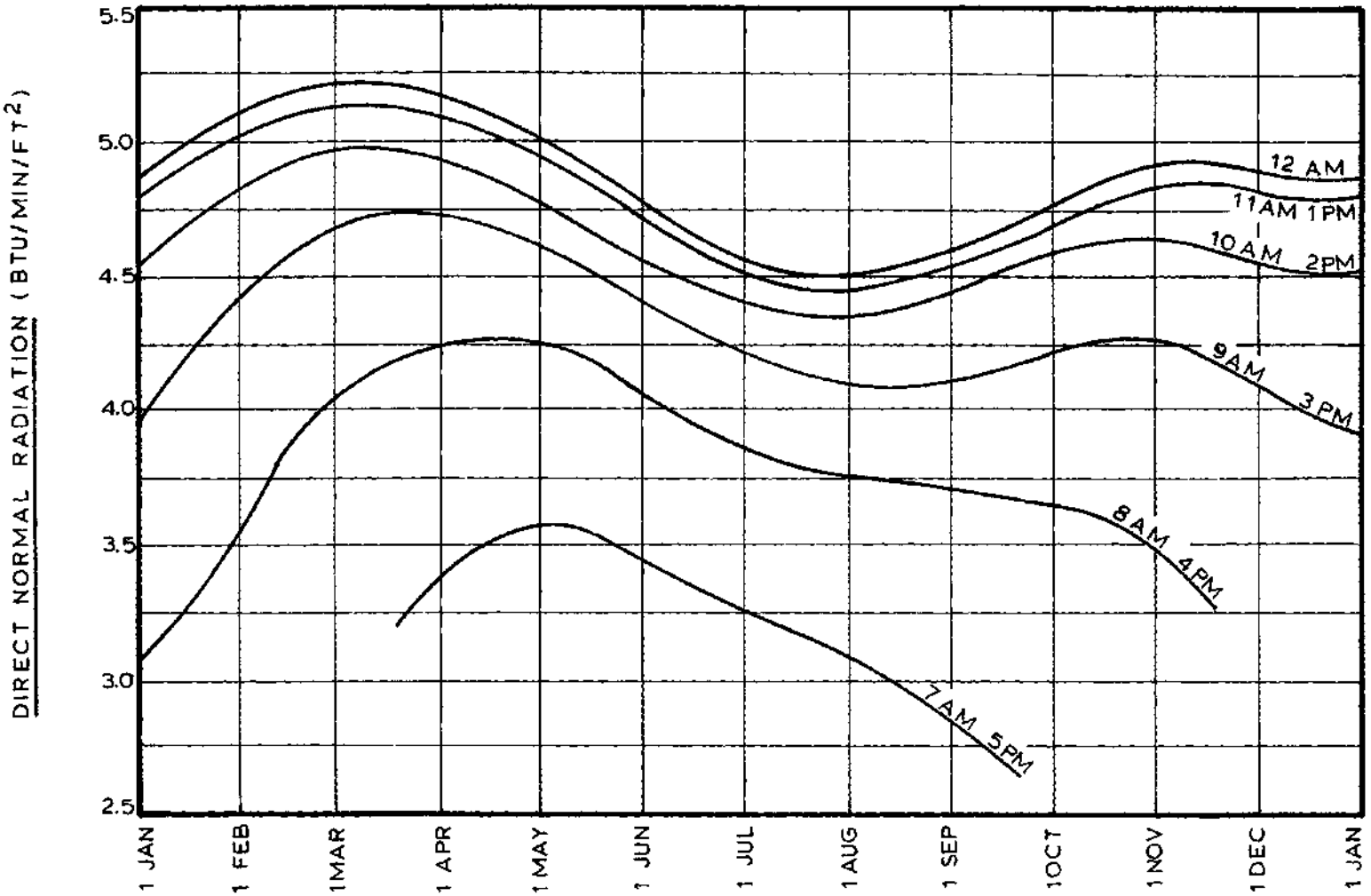

Figure 35. Solar Radiation Curves for Atlanta, Georgia

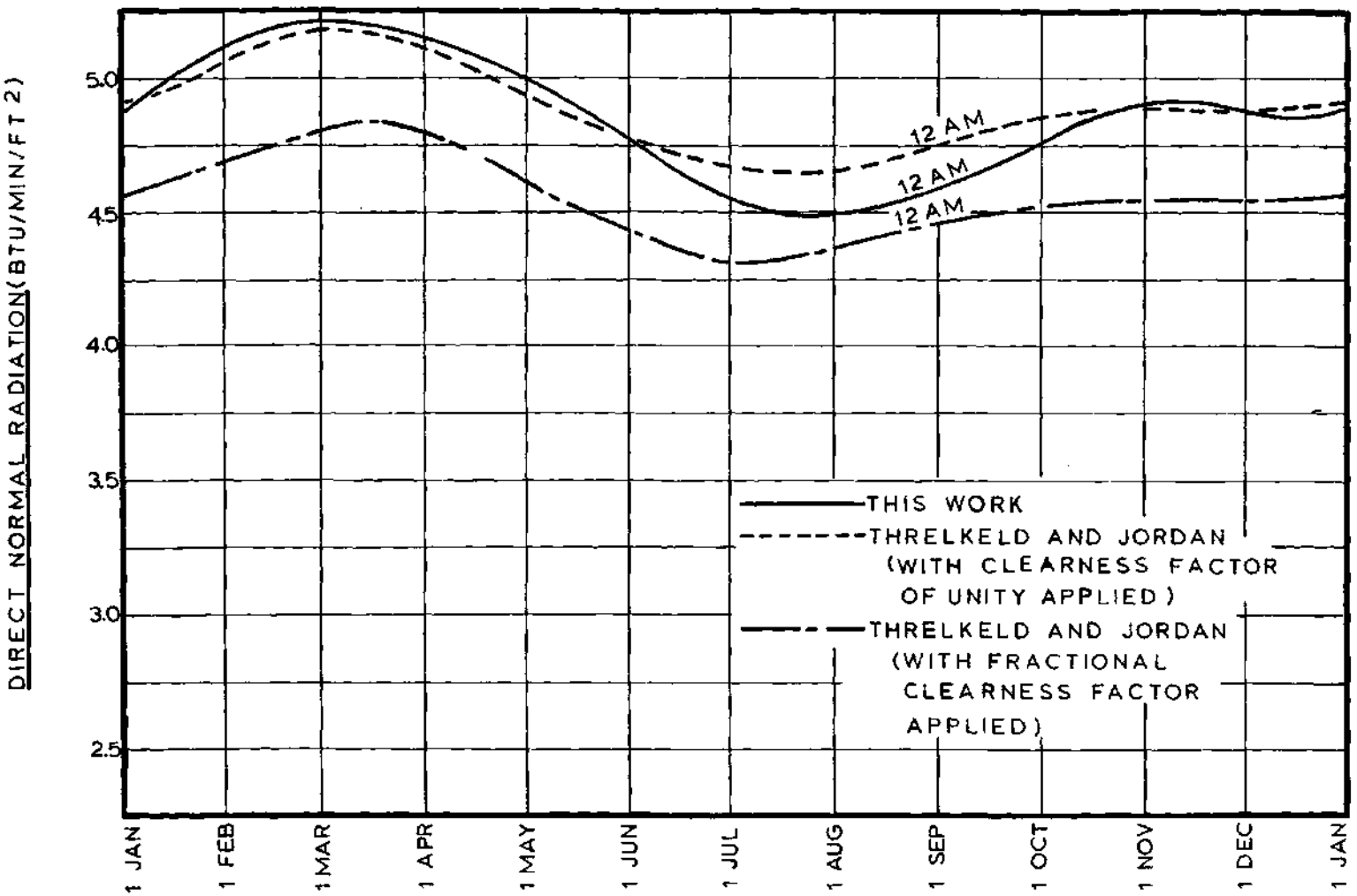

Figure 36. Comparison of Procedures for Calculating Solar Radiation Intensity

Figure 34 where it is seen that the general water vapor distribution assumed by Threlkeld and Jordan[28] agrees very closely with that of Atlanta for the months of January through June. As a result, essentially no clearness factor for those months need be applied to their unity curve. Similarly, for the months of October through December, only a small clearness factor need be applied. However, for the months of July through September, there is a large difference in the two water vapor distributions, and accordingly, a clearness factor of approximately .97 is required. In arriving at their curve for unity clearness factor, Threlkeld and Jordan[28] assumed a basic atmospheric pollution condition of 200 dust particles per cubic centimeter, whereas a value of 150 particles per cubic centimeter was used in this work. Reference to Figure 36 for the months of January through May, when the water vapor distribution was almost identical, shows that the difference in the value of d does not make a large difference, especially in comparison with the effect of variation in atmospheric moisture as demonstrated by consideration of Figure 34 and 35 for the months of July through September.

The accuracy of the curves of Figure 35 cannot be verified without comparison with the actual observed values of direct normal radiation intensity for Atlanta, which are not available. However, Threlkeld and Jordan[28] have demonstrated by comparisons of actual and calculated data for

other localities that use of the atmospheric moisture distribution of a given locality in calculating intensities, as was done in this work, yields a good correlation between actual and calculated values. Thus, it is reasonable to expect Figure 35 to give a good indication of the direct normal radiation intensity in Atlanta on clear days.

Application of Intensity Curves

Basic Relationships

In order to utilize Figure 35, certain basic relationships must be examined. This section includes a brief discussion of the most essential of these.

Calculation of Solar Time. Local standard time, T_L, must have two correction factors applied to it in order to arrive at solar time, T_S. This relationship may be expressed as

$$T_S = T_L - T_{Lo} - T_{vo}, \tag{22}$$

where T_{Lo} is a correction for the difference in the longitude of the specified location and the longitude for which local standard time is established, and T_{vo} is a correction for the variation in the velocity of the earth relative to the sun and the eccentricity of the earth's orbit. An additional hour must be subtracted from local time if daylight savings time is in effect. The longitude of Atlanta is 84°23', and

eastern standard time is measured from 75°-0'. And since each time zone spans 15° longitude, T_{Lo} for Atlanta is given as

$$T_{Lo} = \left(\frac{84°23'-75°0'}{15°}\right)(1 \text{ hr}) = .625 \text{ hrs.}$$

The correction for the speed and orbit of the earth can be determined by linear interpolation from Table 6.[41] Thus, solar time in Atlanta, T_{SA}, can be expressed in terms of Eastern Standard Time, T_{EST}, as

$$T_{SA} = T_{EST} - .625 - T_{vo}, \tag{23}$$

or in terms of Eastern Daylight Saving Time, T_{EDST}, as

$$T_{SA} = T_{EDST} - 1.625 - T_{vo}, \tag{24}$$

where T_{vo} is taken from Table 6.

Solar Angle Definitions

The direct solar radiation intensity incident upon a wall, I_D, is related to the direct normal radiation intensity, I_{DN}, by the relationship

$$I_D = I_{DN} \cos \kappa_T, \tag{25}$$

where κ_T is the angle formed between a solar flux line and the normal to the wall as shown in Figure 37. Cos κ_T can be

Table 6. Correction Factor, T_{vo}*

Month	T_{vo} (1st day of month)	T_{vo} (11th day of month)	T_{vo} (21st day of month)
January	+.060	+.133	+.190
February	+.228	+.240	+.230
March	+.208	+.170	+.123
April	+.067	+.018	-.020
May	-.048	-.062	-.060
June	-.040	-.010	+.025
July	+.060	+.088	+.103
August	+.103	+.085	+.052
September	.000	-.055	-.113
October	-.170	-.218	-.255
November	-.272	-.265	-.235
December	-.184	-.113	-.030

*Expressed in hours

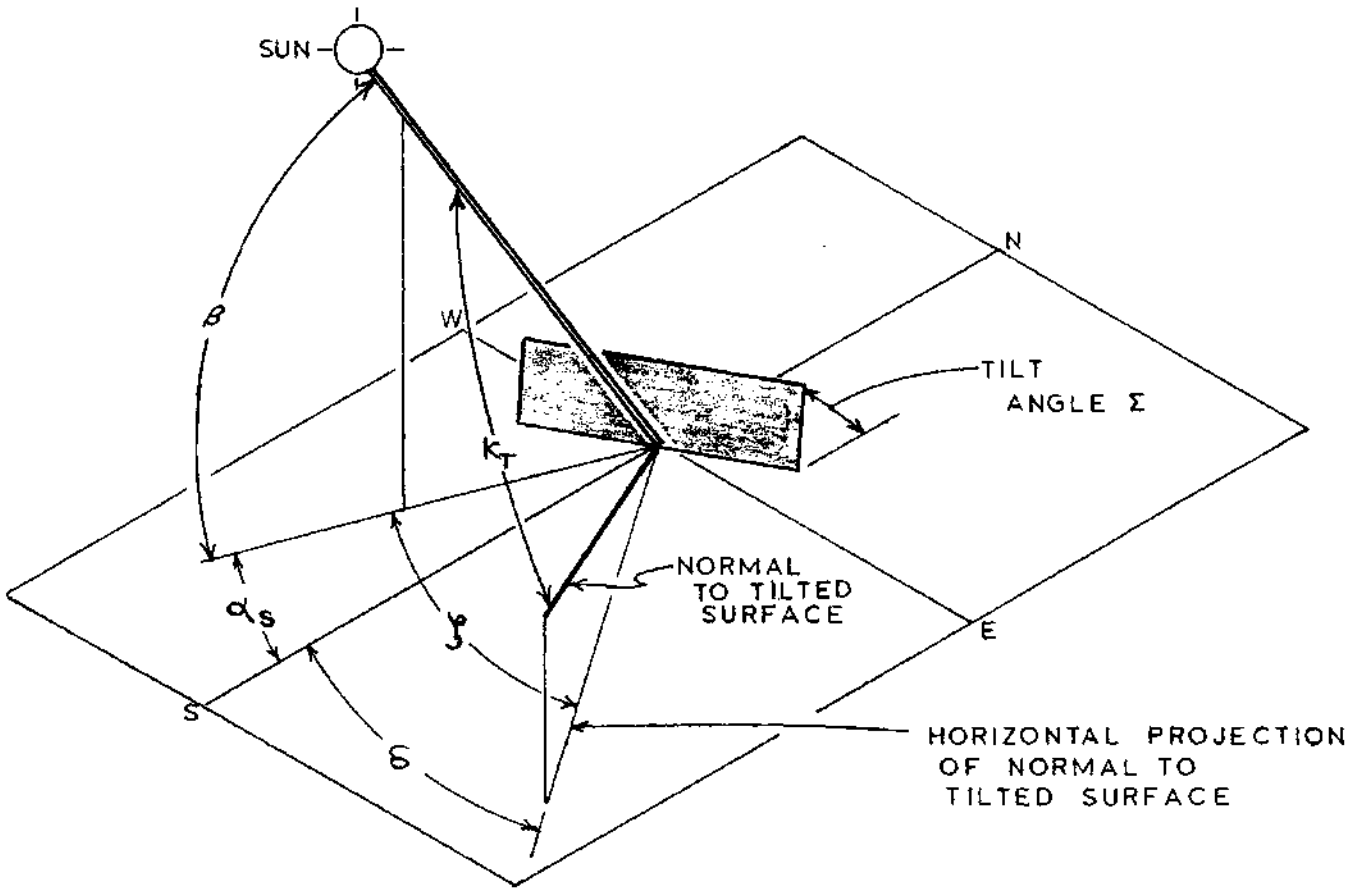

β - SOLAR ALTITUDE

α_s - SOUTH SOLAR AZIMUTH

K_T - INCIDENCE ANGLE FOR TILTED SURFACE

δ - WALL AZIMUTH

ϑ - WALL SOLAR AZIMUTH

Σ - ANGLE OF TILT

Figure 37. Definitions of Solar Angular Relations

determined from the relationship

$$\cos \kappa_T = \cos\beta\cos\delta\sin\Sigma+\sin\beta\cos\Sigma, \tag{26}$$

where β, δ, and Σ are defined in Figure 37 as solar altitude, solar wall azimuth, and tilt angle, respectively. The solar wall azimuth, ζ, is related to the south solar azimuth, α_s, by the relationships

$$\zeta = \alpha_s-\delta, \tag{27}$$

for walls facing east of south in the morning, and for walls facing west of south in the afternoon, and by the relation

$$\zeta = \alpha_s+\delta, \tag{28}$$

for walls facing east of south in the afternoon, and for walls facing west of south in the morning, where δ is the wall azimuth. For the case of a horizontal surface, equation (25) can be written as

$$I_{DH} = I_{DN} \sin\beta. \tag{29}$$

In order to solve equations (25) through (29), β, α_s, Σ, and δ must be known. Σ and δ are physical constants for a given situation. The solar altitude and azimuth, however, are

dependent upon the motion of the earth, and the latitude of the surface on the earth. Tabulated values of solar altitude and azimuth can be found in numerous sources. Figures 38 and 39, giving values of solar altitude and azimuth for Atlanta, were developed by linear interpolation from the tables published in the ASHRAE Handbook of Fundamentals.[26]

Sample Calculations

Three example problems which illustrate the use of the preceding analysis are presented here for clarity. The first example illustrates the derivation of Figure 35, and the remaining two demonstrate the application of Figure 35 for horizontal and tilted concentrators.

Example 1: Calculate the direct normal solar radiation intensity in Atlanta, Georgia, on a clear 21st day of February at 1 p.m. solar time. The dust concentration may be taken as 150 particles per cubic centimeter, and the atmospheric moisture is as given in Figure 34.

Solution: From Figure 38, for the given data, the solar altitude is 43.5°. The air mass, m, equals the cosecant of the solar altitude, except for early morning and late afternoon hours. Thus,

$$m = \text{cosecant } 43.5^\circ = 1.44.$$

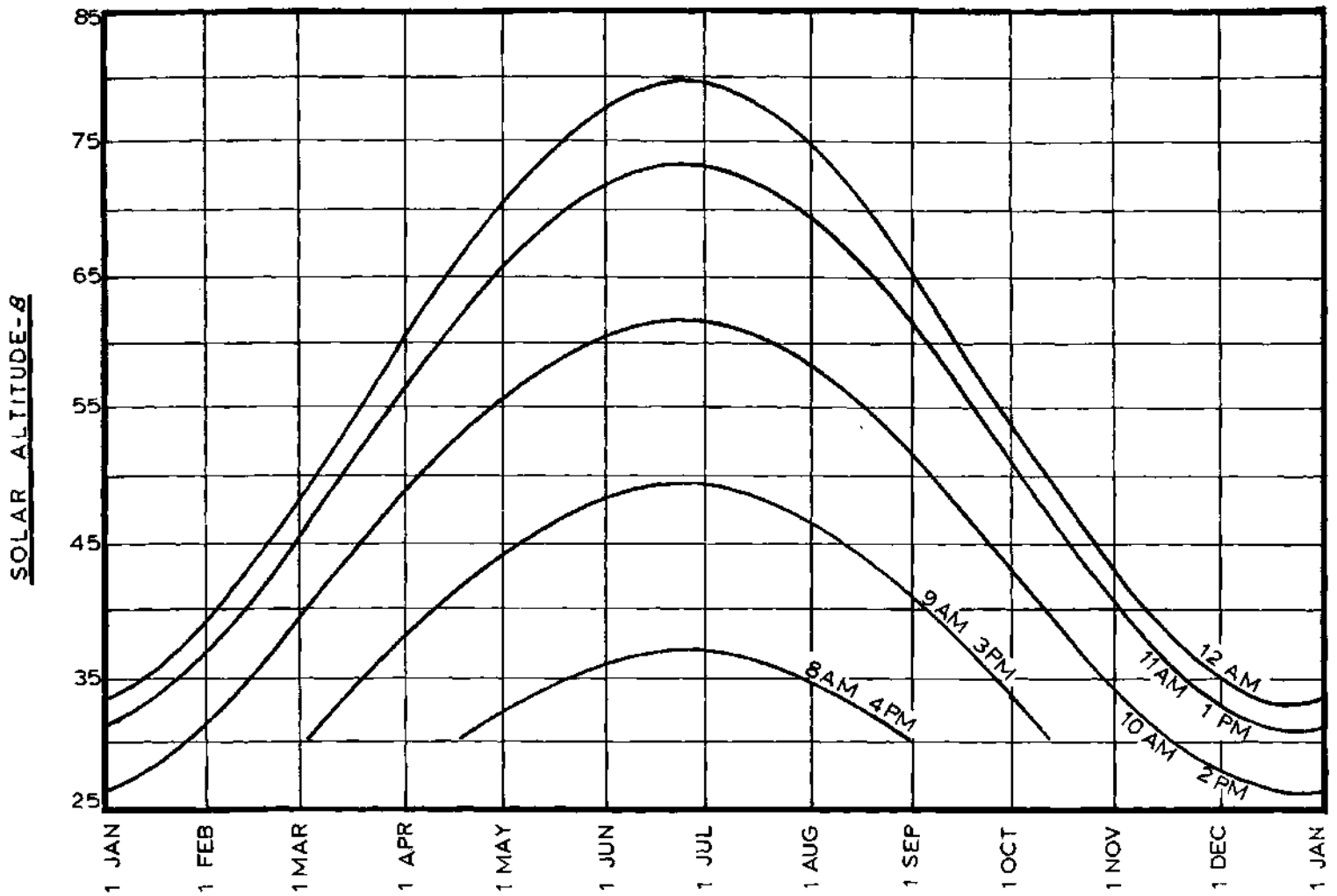

Figure 38. Variation of the Solar Altitude for 33°-45'N Latitude

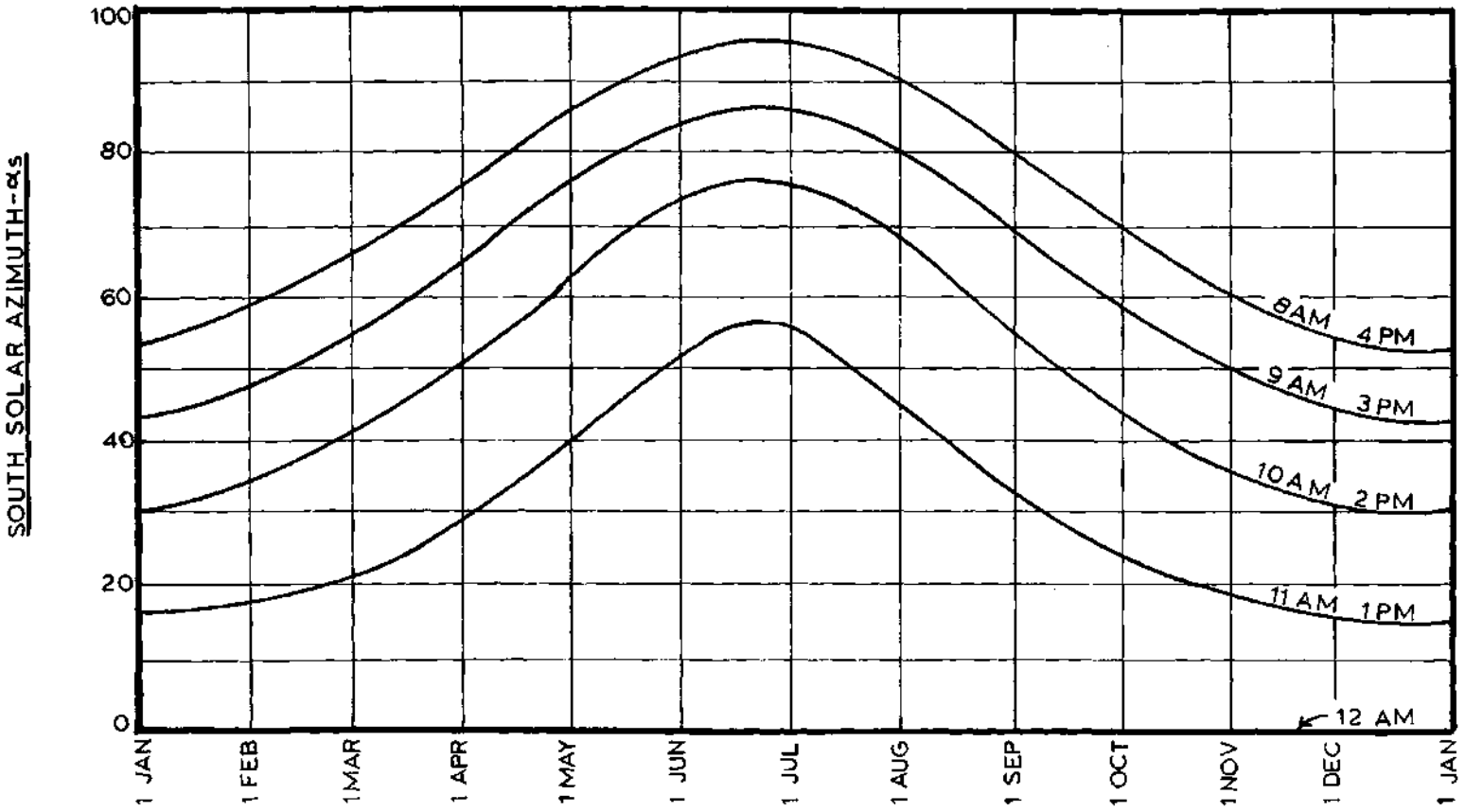

Figure 39. Variation of the South Solar Azimuth for 33°-45'N Latitude

From Figure 34, for the given date, the atmospheric moisture is taken as .41 inches of precipitable water. Entry into Figure 33 at an atmospheric moisture level of .41 inches and an air mass value of 1.44 yields an atmospheric transmissivity of .68. From Figure 29, R_s, as used in equation (18) is seen to be 1.02. If I_o, the solar constant, is taken as 7.37 Btu/min/ft^2, equation (18) may be solved as

$$I_A = 1.02 \times 7.37$$

$$I_A = 7.52 \text{ Btu/min/ft}^2.$$

Thus, equation (17) gives

$$\text{Ans.} \quad I_{DN} = (7.52)\times(.68) = 5.11 \text{ Btu/min/ft}^2.$$

It is seen that the same answer may be obtained by direct entry into Figure 35.

Example 2: Calculate the amount of radiation incident upon a horizontal solar energy concentrator at 3 p.m. Eastern Daylight Saving Time in Atlanta, Georgia, on March 21st.

Solution: From Table 6, T_{vo} is found to be .123 hours. From equation (24) actual solar time is thus found to be

$$T_{SA} = (3-1.625-.123) \approx 1:45 \text{ p.m.}$$

By entry into Figure 35, I_{DN} at 1:45 p.m. solar time on March 21st is 5.0 Btu/min/ft^2. Similarly, Figure 38 reveals that $\beta = 46.5°$. Equation (29) thus yields

$$I_{DH} = 5.0 \sin(46.5) = 3.62 \text{ Btu/min/ft}^2,$$

which for an area of 100 ft^2 gives

Ans. $$\dot{Q}_{in} = 3.62 \times 100 = 362 \text{ Btu/min.}$$

Example 3: For the same date and time as Example 2, calculate the amount of radiation incident upon a 100 ft^2 concentrator which is oriented linearly east to west and which is tilted at 45° with the horizontal, toward the south sky.

Solution: From Example 2, $I_{DN} = 5.0$ Btu/min/ft^2 since the concentrator is oriented east to west, δ=o, and $\zeta = \alpha_s$. From Figures 38 and 39, the solar altitude and azimuth are 46.5° and 40.0°, respectively. Thus, by equation (26),

$$\cos \kappa_T = \cos 46.5° \cos 40° \sin 45° + \sin 46.5° \cos 45°$$

$$\cos \kappa_T = .884$$

Therefore, by equation (25),

$$I_D = 5(.884) = 4.41 \text{ Btu/min/ft}^2,$$

or for a 100 ft^2 concentrator,

Ans. $\dot{Q}_{in} = 4.41 \times 100 = 441$ Btu/min.

Summary

Figure 35 provides a convenient means of determining direct normal solar radiation intensity for Atlanta, Georgia, on clear days. The procedure followed in this work is essentially that of Threlkeld and Jordan.[28] They have demonstrated that its application agrees well with observed radiation data in localities where such data exists. It should be noted, however, that on a clear day, if the atmospheric moisture and/or suspended particulate pollution varies significantly from the assumed mean values, the accuracy of the predicted values of intensity of Figure 35 will vary accordingly.

The procedure followed in obtaining a particle count for Atlanta, which is not actually a particle count, but rather a measure of atmospheric soiling relative to that of Washington, D. C., in the 1920's, is an adequate approximation. However, its accuracy is limited by the fact that Moon[29] developed his transmissivity curve for the standard dust layer on a particle count per unit volume basis, and suspended particulate pollution is today monitored almost entirely on

a mass per unit volume basis. It would be desirable to determine if sufficient correlation exists between the amount of scattering due to dust in the atmosphere and surface measurements of suspended particulate pollution on a mass per unit volume basis. If sufficient correlation exists, Moon's[29] and Threlkeld and Jordan's[28] work could be repeated with the exception of treating the scattering by atmospheric dust on a mass per unit volume basis.

APPENDIX C

HEAT LOSS CALCULATIONS

Bare Pipe Analysis

The bare pipe analysis presented here is based on the data taken at 12:05 p.m. solar time on February 20, 1974. At that time the following conditions existed:

T_a = ambient temperature = 57°F,
T_o = outlet temperature = 153°F,
wind speed = 6.2 ft/sec, and
wind direction from the north-northwest.

Taking the average surface temperature of the pipe, T_s, as being equal to T_o as explained in Chapter IV, the fluid properties evaluated at the film temperature, T_f, equal to 105°F are:

k_f = conductivity of the air = 1.55×10^{-7} (Btu/hr/ft/°F), and
ν_f = 1.83×10^{-4} (ft^2/sec),

The axial component of the wind was 2.4 ft/sec. If the convective heat transfer due to the axial component is

taken as being equal to that of a flat plate of equal length and a width equal to the circumference of the pipe, then the average axial convective heat transfer coefficient, $\bar{h}_{c-a}$, is found to be .937 Btu/hr/ft^2/°F.

The Reynolds Number, Re, for the crossflow is

$$Re = \frac{vD}{\nu_f} = 5.55 \times 10^3,$$

where

v = crossflow velocity = 6.2 cos 22.5° = 5.7 ft/sec,

D = outside pipe diameter = 1.78×10^{-1} ft, and

$\nu_f = 1.83 \times 10^{-4}$ ft^2/sec.

The experimental relationship developed by Hilpert, as presented by Kreith,[42] relating the forced convective losses from a circular cylinder in a steady crossflow to the Reynolds number is

$$\frac{\bar{h}_{c-c}D}{k} = c\left(\frac{vD}{\nu_f}\right)^n, \tag{30}$$

where $\bar{h}_{c-c}$ is the average crossflow convective heat transfer coefficient, and c and n are empirical constants respectively equal to .174 and .618, for a Reynolds number in the range 4,000 < Re < 40,000. Kreith[42] points out that if homogeneous turbulence is caused upstream of the cylinder by a grid or other turbulence promoter, the convective

coefficient may be increased by as much as 50 percent. However, he does not indicate the effect of free stream or isentropic turbulence, such as is caused by the wind in this program, upon the convective coefficient. It is reasonable that the effect would be similar to that of homogeneous turbulence; therefore, it is assumed that the convective coefficient for the condition under study would be 50 percent higher than that given by equation 30. Hence, the average crossflow convective heat transfer coefficient for this work is given by the relation

$$\bar{h}_{c\text{-}c} = \frac{1.5\ kc}{D} \left(\frac{vD}{\nu}\right)^n, \tag{31}$$

or for the specific data under study,

$$\bar{h}_{c\text{-}c} = 4.76\ \text{Btu/hr/ft}^2/^\circ\text{F}.$$

Thus, combining the axial and crossflow coefficients yields

$$\underline{\bar{h}_c = 5.7\ \text{Btu/hr/ft}^2/^\circ\text{F},}$$

where $\bar{h}_c$ is the average convective heat transfer coefficient.

It is assumed that the bare pipe at a mean surface temperature T_s, radiates to surfaces at the ambient temperature, T_a; that the average emissivity of the pipe surface, which is half tarnished copper and half carbon black, is .9; and that

the shape factor equals unity. Therefore, the radiation heat transfer coefficient, $\bar{h}_r$ =, may be expressed as

$$\bar{h}_r = .9\ F_T, \tag{32}$$

where F_T is the temperature factor as defined by Kreith.[42] The value of F_T for the specified conditions is given by Kreith[42] as 1.3. Thus,

$$\bar{h}_r = 1.17 \text{ Btu/hr/ft}^2/^\circ\text{F}.$$

The combined unit surface conductance, h, is given by the relation

$$\bar{h} = \bar{h}_c + \bar{h}_r. \tag{33}$$

Therefore, for the specified conditions,

$$\bar{h} = 6.87 \text{ Btu/hr/ft}^2/^\circ\text{F, or } .114 \text{ Btu/min/ft}^2/^\circ\text{F}.$$

Unevacuated Acrylic Tube Receiver Analysis

The acrylic tube receiver is evaluated here at the conditions which existed at 12:05 p.m. on April 16, 1974, which are

T_o = outlet temperature = 182°F,

T_a = ambient temperature = 68°F,
wind speed = 7.35 ft/sec, and
wind direction: from the north-northwest.

Figure 40 shows the temperature profile across the acrylic tube receiver and defines the various temperatures and physical constants pertinent to the analysis. As explained in Chapter IV, the average surface temperature of the copper pipe, T_s, is assumed to be equal to the outlet temperature. Figure 41 is the electrical analogy of the thermal circuit for the acrylic tube receiver, where

R_{r1} = resistance to radiation from T_s to T_{w1},
R_{r2} = resistance to radiation from T_{w2} to T_a,
R_A = resistance to conduction by the air between r_1 and r_2,
R_p = resistance to conduction by the acrylic pipe, and
R_f = resistance to heat transfer by the air film.

It is assumed that T_{w2} is sufficiently close to T_a to render R_{r2} to approach infinity.

The object of this analysis to to determine the value of the product UA for the specified conditions where U is the overall heat transfer coefficient, and A is any pertinent heat transfer surface area. Since the product UA is equal to $1/R_{eq}$, where R_{eq} is the equivalent resistance of the thermal circuit of Figure 41, it is necessary to determine

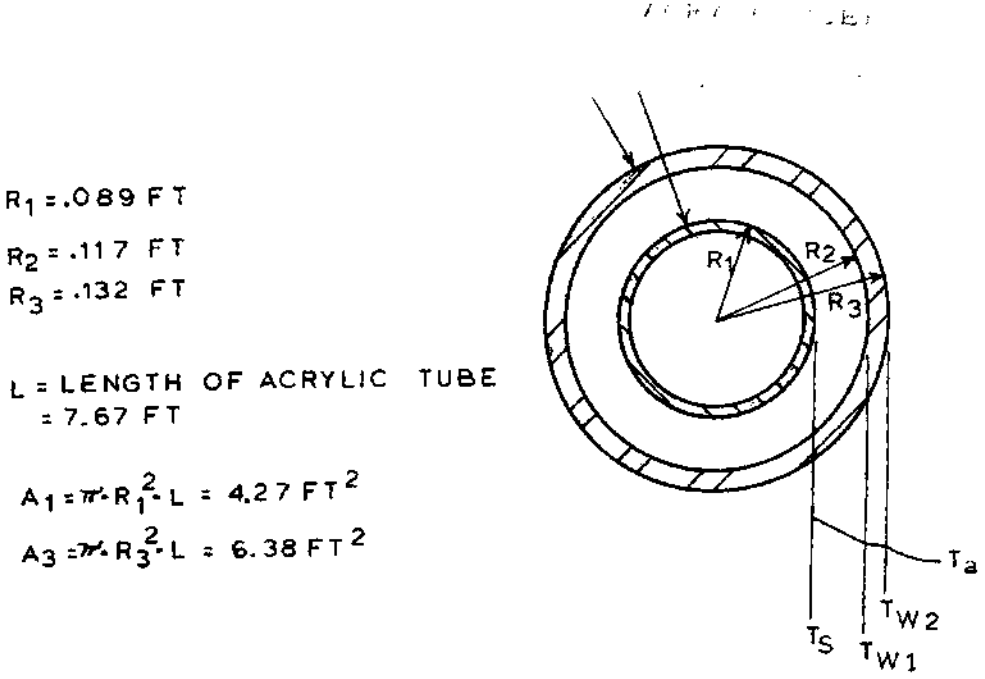

Figure 40. Temperature Profile Across the Acrylic Tube Receiver Section

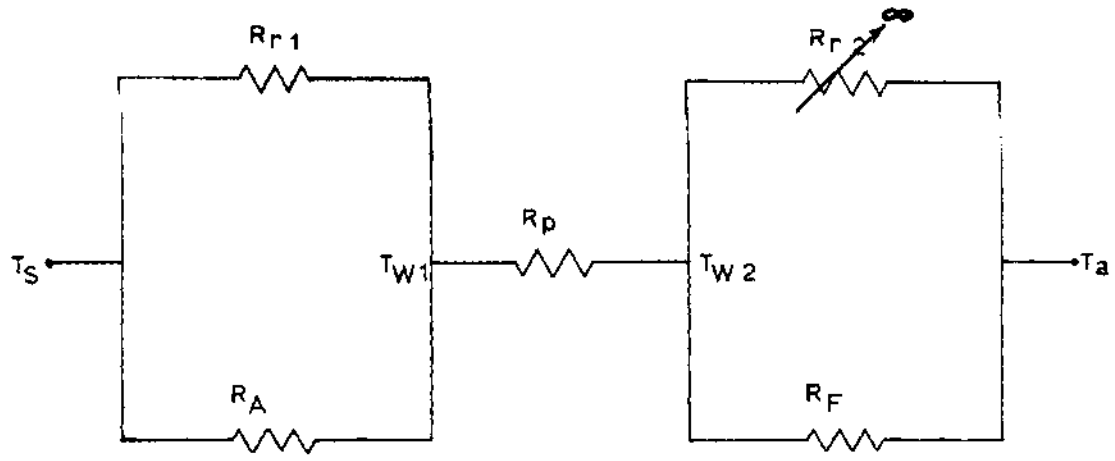

Figure 41. Electrical Analogy of the Thermal Circuit

the values of the individual resistances. Values of T_{w1} are assumed until the flow of heat from R_s to T_{w1} equals that from T_{w1} to T_a. By trial and error, T_{w1} for the specified conditions is found to be approximately 107°F. The thermal resistance and the product UA are evaluated in what follows.

R_{r1}, Resistance To Radiation from T_s to T_{w1}

The resistance to radiation from T_s to T_{w1} is given by the relation

$$R_{r1} = \frac{1}{A_1 \bar{h}_r} .$$

$A_1 = 4.27$ ft^2, and $\bar{h}_r$ for the specified conditions is 1.35 as determined by the procedure in the preceding section. Therefore,

$$R_{r1} = .174°F\text{-hr/Btu}.$$

R_A, Resistance to Heat Transfer by the Air Gap

The resistance to heat transfer by the air gap is given by the relation

$$R_A = \frac{\ln (\frac{r_2}{r_1})}{2\pi k_{ec} \ell} ,$$

where k_{ec} is the effective conductivity of the air which includes both the conductive and convective effects of the air. Jakobs[43] presents the empirical curve developed by

Beckman for evaluating the value of k_{ec} for air between two coaxial horizontal cylinders. Beckman's curve is a plot of log (k_{ec}/k) versus log G_r for various values of diameter ratios where G_r is the Grashof number with the diameter of the inside cylinder taken as the characteristic length. For the specified conditions, $G_r = 5.7 \times 10^5$. From Beckman's curves this gives

$$\log (k_{ec}/k) = .05, \text{ thus}$$

$$k_{ec} = 1.2\ k = 1.95 \times 10^{-2} \text{ Btu/hr/ft/°F, and}$$

$$\underline{R_A = .313 \text{ hr-°F/Btu}}$$

$\underline{R_p}$ Resistance to Conduction by the Acrylic Pipe

The resistance to conduction by the acrylic pipe is given by the relation

$$R_p = \frac{\ln (\frac{r_2}{r_3})}{2\pi\ k_p\ \ell} = .0104 \text{ hr-°F/Btu,}$$

where k_p is the conductivity of the acrylic pipe which is given by the manufacturer[23] as .192 Btu/hr/ft/°F.

$\underline{R_f}$, Resistance to Heat Transfer by the Air Film

The thermal resistance of the film is given by the relation

$$R_f = \frac{1}{\bar{h}_c A_3} = .0341 \text{ hr-°F/Btu},$$

where, by the same procedure used in the bare pipe analysis, $\bar{h}_c$ is determined to be 4.6 Btu/hr/ft/°F for the specified conditions.

Determination of the Product UA

The equivalent resistance of the circuit shown in Figure 41 is thus

$$R_{eq} = .156 \text{ hr-°F/Btu}.$$

This gives

$$UA = 1/R_{eq} = \underline{6.4 \text{ Btu/hr/°F} = .107 \text{ Btu/min/°F}}$$

Conductivity of Air in an Evacuated Gap

The conductivity of air is independent of pressure as long as the mean free path of the air molecules, λ, is small in comparison with the gap width. However, as the pressure is reduced so that the mean free path approaches the same order of magnitude as the gap width, the conductivity becomes increasingly a function of the pressure. And as the pressure is reduced beyond that pressure at which λ equals the gap width, the conductivity is proportional to the pressure. This relationship may be best understood from a

microscopic point of view. At pressures large in comparison with the critical pressure, a reduction in pressure does reduce the number of molecules which can transport energy, but this effect is offset by the fact that fewer molecules are required to transport the same energy at lower pressures because fewer collisions are encountered. Thus the conductivity remains relatively constant. However, at pressures small in comparison with the critical pressure, the molecules, on an average, can pass directly from one wall to the other without collision, so that the only effect of lowering the pressure is to reduce the number of molecules available to transport energy. This reduces the conductivity of the air space proportionately.

The approximate mean free path of molecules of air is given by Dushman[44] as

$$\lambda = \frac{1.58 \times 10^{-8}}{\rho} \text{ ft}, \tag{34}$$

where ρ is the density of air under the specified conditions in lbm/ft^3. For the gap width of the acrylic tube receiver, .34 inches, and the temperature corresponding to that of the air in the gap when the best vacuum was obtained, 82°F, the critical vacuum pressure is 5.8 microns of mercury. Therefore, in order to have significantly reduced the conductivity of the air gap during the experimental program, the vacuum pressure would have to have been reduced beyond

5.8 microns. Since the lowest vacuum attained was only 21 microns, the conductivity of the air was never significantly affected.

Wilkes[45] and Dushman[44] present good discussions of the effect of high vacuum on the conductivity of air. And a description of a successful attempt to utilize a high vacuum as an insulator for a solar flat plate collector is given by Sprayer.[46]

APPENDIX D

RAW DATA AND PERTINENT CALCULATED VALUES

Table 7. Raw Data for the Bare Pipe Configuration Tested at the Standard Height on February 20, 1974

Solar Time	T_a (°F)	Wind Velocity (ft/min)	Wind Direction	T_1 (°F)	T_o (°F)	T_i (°F)	$\dot{m}$ (lbm/min)	Number of Segments Shaded
1205	57.0	370	NNW	158.0	153.0	63.0	.28	0
1300	61.0	0	--	133.0	132.0	69.5	.56	0
1330	63.5	0	--	110.5	109.5	68.0	1.02	0
1355	65.5	120	NNW	96.0	96.0	65.0	1.39	0
1435	64.0	125	NW	85.5	83.0	62.0	1.66	0

Table 8. Raw Data for the Shrouded Pipe Configuration Tested at the Standard Height on February 26, 1974

Solar Time	T_a (°F)	Wind Velocity (ft/min)	Wind Direction	T_1 (°F)	T_o (°F)	T_i (°F)	$\dot{m}$ (lbm/min)	Number of Segments Shaded
1215	40	310	NW	202.5	189.0	51.0	.09	5.00
1315	43	610	NNW	167.5	162.0	56.5	.19	3.00
1350	44	615	NNW	114.0	112.0	53.0	.65	2.25
1415	45	515	NNW	90.5	88.5	54.5	1.02	1.50
1440	46	590	NNW	76.0	75.0	54.5	1.67	.75
1505	47	610	NNW	70.0	69.0	54.5	2.04	0.00

Table 9. Raw Data for the Shrouded Pipe with One Layer of Tedlar Tested at the Standard Height

Date	Solar Time	T_a (°F)	Wind Velocity (ft/min)	Wind Direction	T_1 (°F)	T_o (°F)	T_i (°F)	$\dot{m}$ (lbm/min)	Number of Segments Shaded
27/2/74	1215	59.0	0	--	217.5	213.0	75.0	.185	4.5
27/2/74	1300	60.0	0	--	158.5	157.0	69.0	.416	3.0
27/2/74	1355	62.0	540	S	115.0	115.0	67.0	.647	2.0
27/2/74	1415	62.0	460	SW	104.5	104.0	67.0	.925	1.5
27/2/74	1500	64.0	445	SW	80.6	85.0	65.5	1.295	0.0
28/2/74	1200	64.0	685	WSW	191.5	187.0	71.5	.250	5.5
28/2/74	1245	67.0	605	SW	182.0	179.0	77.0	.290	4.5

Table 10. Raw Data for the Shrouded Pipe with Two Layers of Tedlar Tested at the Standard Height on March 4, 1974

Solar Time	T_a (°F)	Wind Velocity (ft/min)	Wind Direction	T_1 (°F)	T_o (°F)	T_i (°F)	$\dot{m}$ (lbm/min)	Number of Segments Shaded
1225	76	420	S	187.5	191.0	83.0	.25	7
1300	78	695	SSW	174.5	170.0	84.5	.35	6
1330	78	790	S	159.0	156.0	84.5	.45	5
1355	79	438	S	136.5	134.0	86.5	.57	4
1425	79	505	WSW	124.5	123.0	84.0	.70	3
1445	80	620	SW	111.5	110.0	82.5	.95	2

Table 11. Raw Data for the Evacuated Acrylic Tube Configuration Tested at the Standard Height on March 14, 1974

Solar Time	T_a (°F)	Wind Velocity (ft/min)	Wind Direction	T_1 (°F)	T_o (°F)	T_i (°F)	T_4 (°F)	$\dot{m}$ (lbm/min)	P_v*	Number of Segments Shaded
1255	66	0	--	194.0	202.5	78.0	94.5	.25	58	6.0
1320	68	125	S	172.0	180.5	82.0	93.0	.38	43	5.0
1345	68	290	SE	151.5	158.5	77.0	88.5	.47	38	4.0
1410	69	170	NW	131.0	134.0	74.5	85.5	.61	29	3.0
1430	73	0	--	118.5	120.0	72.5	84.5	.80	25	2.5
1455	70	0	--	95.0	97.5	70.0	78.0	1.21	21	2.0

*P_v is vacuum pressure measured in microns of mercury.

Table 12. Raw Data for the Unevacuated Acrylic Tube Configuration Tested at the Increased Height on April 7, 1974

Solar Time	T_a (°F)	Wind Velocity (ft/min)	Wind Direction	T_1 (°F)	T_o (°F)	T_i (°F)	T_4 (°F)	$\dot{m}$ (lbm/min)	Number of Segments Shaded
1145	69	540	SSE	204.5	211.0	68	97.0	.24	0.0
1230	70	390	SSW	172.5	176.0	68	94.0	.32	0.0
1255	70	545	SSW	138.0	142.5	67	86.0	.62	0.0
1320	71	450	SE	115.0	116.0	66	82.0	.91	0.0
1340	72	580	S	93.5	95.0	65	79.0	1.38	0.0

Table 13. Raw Data for the Unevacuated Acrylic Tube Configuration Tested with the Concentrator Tilted on April 16, 1974

Solar Time	T_a (°F)	Wind Velocity (ft/min)	Wind Direction	T_1 (°F)	T_o (°F)	T_i (°F)	T_4 (°F)	$\dot{m}$ (lbm/min)	Number of Segments Shaded
1115	67	150	W	193.0	201.5	69.5	109.5	.24	7
1205	68	440	NNW	174.5	182.0	67.0	103.0	.34	7
1250	70	410	NW	150.5	157.0	65.0	95.0	.47	7
1310	72	0	--	132.0	138.0	65.5	97.0	.60	6
1330	70	0	--	119.0	122.0	64.0	89.0	.78	6
1350	71	200	N	106.5	109.5	63.0	85.0	.90	6
1420	71	0	--	86.0	88.5	61.5	84.0	1.45	6

Table 14. Values of Incident Radiation, Thermal Output, and Thermal Efficiency Calculated from the Bare Pipe Data for the Standard Height Test*

Solar Time	I_{DN} **	Solar Altitude	I_D **	A_c (ft^2)	$\dot{Q}_{in}$ (Btu/min)	$T_o - T_i$ (°F)	$\dot{m}$ (lbm/min)	$\dot{Q}_{out}$ (Btu/min)	η_T	$T_o - T_a$ (°F)
1205	5.20	45.6	3.72	28.4	105.5	90.0	.28	25.2	23.9	96.0
1300	5.13	43.0	3.50	28.4	99.5	62.5	.56	35.0	35.2	71.0
1330	5.07	40.0	3.26	28.4	92.5	41.5	1.02	42.4	45.8	46.0
1355	5.00	37.5	3.04	28.4	86.4	31.0	1.39	43.1	50.0	30.5
1435	4.80	32.5	2.58	28.4	73.3	21.0	1.66	34.8	47.5	19.0

*See Table 7 for raw data.

**Btu/min/ft^2

Table 15. Values of Incident Radiation, Thermal Output, and Thermal Efficiency Calculated from the Shrouded Pipe Data for the Standard Height Tests*

Solar Time	I_{DN}**	Solar Altitude	I_D**	A_c (ft^2)	$\dot{Q}_{in}$ (Btu/min)	T_o-T_i (°F)	$\dot{m}$ (lbm/min)	$\dot{Q}_{out}$ (Btu/min)	η_T	T_o-T_a (°F)
1215	5.18	47.5	3.82	26.02	99.5	138.0	.09	12.4	12.5	149.0
1315	5.10	44.0	3.54	26.97	95.5	105.5	.19	20.0	21.0	119.0
1350	5.01	40.5	3.26	27.33	89.0	59.0	.65	38.3	42.7	68.0
1415	4.90	36.0	2.88	27.69	79.7	34.0	1.02	34.7	42.0	43.5
1440	4.75	32.5	2.55	28.04	71.6	20.5	1.67	34.2	47.8	29.0
1505	4.55	29.0	2.21	28.40	62.6	14.5	2.04	29.6	47.3	22.0

*See Table 8 for raw data.

**Btu/min/ft^2

Table 16. Values of Incident Radiation, Thermal Output, and Thermal Efficiency Calculated from the Raw Data for the Shrouded Pipe with One Layer of Tedlar Tested at the Standard Height*

Solar Time	I_{DN} **	Solar Altitude	I_D **	A_c (ft^2)	$\dot{Q}_{in}$ (Btu/min)	T_o-T_i (°F)	$\dot{m}$ (lbm/min)	$\dot{Q}_{out}$ (Btu/min)	η_T	T_o-T_a (°F)
1215	5.18	48.5	3.88	26.26	102.0	138.0	.185	25.5	25.0	154.0
1300	5.13	46.5	3.72	26.97	100.0	88.0	.416	36.6	36.6	97.0
1355	5.00	40.0	3.22	27.45	88.5	48.0	.647	31.1	35.2	53.0
1415	4.90	37.5	2.98	27.69	82.5	37.0	.925	34.2	41.5	42.0
1500	4.65	30.0	2.32	28.40	55.9	19.5	1.295	25.2	45.1	21.0
1200	5.20	49.0	3.92	25.78	101.0	115.5	.250	28.9	28.6	123.0
1245	5.15	47.0	3.76	26.26	98.9	102.0	.290	29.6	29.9	112.0

*See Table 9 for raw data.

**Btu/min/ft^2

Table 17. Values of Incident Radiation, Thermal Output, and Thermal Efficiency Calculated from the Raw Data for the Shrouded Pipe with Two Layers of Tedlar Tested at the Standard Height*

Solar Time	I_{DN} **	Solar Altitude	I_D **	A_c (ft^2)	$\dot{Q}_{in}$ (Btu/min)	$T_o - T_i$ (°F)	$\dot{m}$ (lbm/min)	$\dot{Q}_{out}$ (Btu/min)	η_T	$T_o - T_a$ (°F)
1225	5.17	49.0	3.90	25.07	97.7	108.0	.25	27.0	27.6	115
1300	5.12	47.5	3.78	25.54	96.5	85.5	.35	29.9	31.0	92
1330	5.07	44.0	3.52	26.02	91.6	71.5	.45	32.2	35.1	78
1355	5.02	42.0	3.36	26.50	89.0	47.5	.57	27.1	30.4	55
1425	4.85	37.5	2.96	26.97	79.7	39.0	.70	27.3	34.2	44
1445	4.75	34.0	2.66	27.45	73.0	27.5	.95	26.1	35.8	30

*See Table 10 for raw data.

**$Btu/min/ft^2$

Table 18. Values of Incident Radiation, Thermal Output, and Thermal Efficiency Calculated from the Raw Data for the Evacuated Acrylic Tube Tested at the Standard Height*

Solar Time	I_{DN} **	Solar Altitude	I_D **	A_c (ft^2)	$\dot{Q}_{in}$ (Btu/min)	$T_o - T_i$ (°F)	$\dot{m}$ (lbm/min)	$\dot{Q}_{out}$ (Btu/min)	η_T	$T_o - T_a$ (°F)
1255	5.12	52.0	4.20	25.54	107.0	124.5	.25	31.10	30.8	136.5
1320	5.08	49.0	3.83	26.02	99.8	98.5	.38	37.40	37.5	112.5
1345	5.00	46.5	3.63	26.50	96.2	81.5	.47	38.20	39.7	90.5
1410	4.95	43.0	3.38	26.97	91.0	59.5	.61	36.30	39.9	65.0
1430	4.85	40.0	3.12	27.21	85.0	47.5	.80	38.00	44.7	47.0
1455	4.77	36.0	2.80	27.45	77.0	27.5	1.21	33.20	43.0	27.5

*See Table 11 for raw data.

**Btu/min/ft^2

Table 19. Values of Incident Radiation, Thermal Output, and Thermal Efficiency Calculated from the Raw Data for the Unevacuated Acrylic Tube Receiver Tested at an Increased Height*

Solar Time	I_{DN} **	Solar Altitude	I_D **	A_c (ft^2)	$\dot{Q}_{in}$ (Btu/min)	$T_o - T_i$ (°F)	$\dot{m}$ (lbm/min)	$\dot{Q}_{out}$ (Btu/min)	η_T	$T_o - T_a$ (°F)
1145	5.10	62.5	4.52	28.4	128.4	143.0	.24	34.3	26.7	142.0
1230	5.07	61.5	4.45	28.4	126.3	108.0	.32	34.5	32.0	106.0
1255	5.05	60.0	4.37	28.4	124.0	75.5	.62	46.8	37.7	72.5
1320	5.00	57.5	4.22	28.4	120.0	50.0	.91	45.5	37.9	45.0
1340	4.95	54.0	4.00	28.4	114.0	30.0	1.38	41.4	36.3	23.0

*See Table 12 for raw data.

**Btu/min/ft^2

Table 20. Values of Incident Radiation, Thermal Output, and Thermal Efficiency Calculated from the Raw Data for the Unevacuated Acrylic Tube Receiver Tested with a Tilted Concentrator*

Solar Time	I_{DN}**	$\cos\theta_T$	I_D**	A_c (ft^2)	$\dot{Q}_{in}$ (Btu/min)	T_o-T_i (°F)	$\dot{m}$ (lbm/min)	$\dot{Q}_{out}$ (Btu/min)	η_T	T_o-T_a
1115	5.03	.986	4.96	25.07	124.5	132.0	.24	31.65	25.3	134.5
1205	5.07	.992	5.03	25.07	126.0	115.0	.34	39.10	31.0	114.0
1250	5.03	.986	4.96	25.07	124.5	92.0	.47	43.30	34.8	87.0
1310	5.00	.967	4.84	25.54	123.5	72.5	.60	43.50	35.2	66.0
1330	4.95	.934	4.62	25.54	118.0	58.0	.78	45.30	38.4	52.0
1350	4.85	.901	4.37	25.54	111.5	46.5	.90	41.80	37.4	38.5
1420	4.83	.829	4.00	25.54	102.0	27.0	1.45	39.20	38.4	17.5

*See Table 13 for raw data.

**Btu/min/ft^2

Table 21. Analysis of Data from Testing the Shrouded Pipe at the Standard Height

Solar Time	$\dot{Q}_{in}$* (Btu/min)	$\dot{Q}_{out}$* (Btu/min)	L_q** (Btu/min)	$T_o - T_a$* (°F)
1215	99.5	12.4	49.1	149.0
1315	95.5	20.0	38.9	119.0
1350	89.0	38.3	16.7	68.0
1415	79.7	34.7	14.5	43.5
1440	71.6	34.2	10.0	29.0
1505	62.6	29.6	9.0	22.0

*From Table 15.

**Thermal losses determined by equation (7).

Table 22. Analysis of Data from Testing the Shrouded Pipe with One Layer of Tedlar at the Standard Height

Solar Time	$\dot{Q}_{in}$* (Btu/min)	$\dot{Q}_{out}$* (Btu/min)	L_q** (Btu/min)	$T_o - T_a$* (°F)
1215	102.0	25.5	24.2	154.0
1300	100.0	36.6	12.1	97.0
1355	88.5	31.1	12.0	53.0
1415	82.5	34.2	5.9	42.0
1500	55.9	25.2	2.0	21.0
1200	101.0	28.9	20.3	123.0
1245	98.9	29.6	18.5	112.0

*From Table 16.

**Thermal losses determined by equation (8).

Table 23. Analysis of Data from Testing the Shrouded Pipe with Two Layers of Tedlar at the Standard Height

Solar Time	$\dot{Q}_{in}$* (Btu/min)	$\dot{Q}_{out}$* (Btu/min)	L_q** (Btu/min)	$T_o - T_a$ (°F)
1225	97.7	27.0	12.4	115
1300	96.5	29.9	9.0	92
1330	91.6	32.2	4.7	78
1355	89.0	27.1	8.6	55
1425	79.7	27.3	4.8	44
1445	73.0	26.1	3.3	30

*From Table 17.

**Thermal losses determined by equation (8).

Table 24. Analysis of Data from Testing the Unevacuated Acrylic Tube Receiver at the Standard Height

Solar Time	$\dot{Q}_{in}$* (Btu/min)	$\dot{Q}_{out}$* (Btu/min)	L_q** (Btu/min)	$T_o - T_a$* (°F)
1115	124.5	31.7	23.1	134.5
1205	126.0	39.1	16.3	114.0
1250	124.5	43.3	11.5	87.0
1310	123.5	43.5	10.8	66.0
1330	118.0	45.3	6.6	52.0
1350	111.5	41.8	7.2	38.5
1420	102.0	39.2	5.7	17.5

*From Table 20.

**Thermal losses determined by equation (8), except G=.9.

Table 25. Analysis of the Data from Testing the Evacuated Acrylic Tube Receiver at the Standard Height

Solar Time	$\dot{Q}_{in}$* (Btu/min)	$\dot{Q}_{out}$* (Btu/min)	L_q** (Btu/min)	$T_o - T_a$* (°F)
1255	107.0	31.1	21.1	136.5
1320	99.8	37.4	11.4	112.5
1345	96.2	38.2	8.7	90.5
1410	91.0	36.3	8.1	65.0
1430	85.0	38.0	3.5	47.0
1455	77.0	33.2	4.4	27.5

*From Table 18.

**Thermal losses determined by equation (8).

Table 26. Analysis of Data from Testing the Unevacuated Acrylic Tube at an Increased Height

Solar Time	$\dot{Q}_{in}$* (Btu/min)	$\dot{Q}_{out}$* (Btu/min)	L_q** (Btu/min)
1145	128.4	34.3	22.6
1230	126.3	34.5	21.5
1255	124.0	46.8	8.2
1320	120.0	45.5	7.6
1340	114.0	41.4	9.6

*From Table 19.

**Thermal losses = $(.91)(.65)(.75) - \dot{Q}_{out}$.

Table 27. Predicted Performance of the Unevacuated Acrylic Tube at the Standard Height

Solar Time	$\dot{Q}_{in}$* (Btu/min)	L_q** (Btu/min)	$\dot{Q}_{out}$* (Btu/min)
1145	128.4	22.6	36.2
1230	126.3	21.5	36.4
1255	124.0	8.2	48.6
1320	120.0	7.6	47.4
1340	114.0	9.6	43.0

*From Table 19.

**From Table 26.

Table 28. Analysis of the Data from Testing the Acrylic Tube Receiver with a Tilted Concentrator

Solar Time	$\dot{Q}_{in}$* (Btu/min)	$\dot{Q}_{out}$* (Btu/min)	L_q* (Btu/min)
1115	124.5	31.7	22.9
1205	126.0	39.1	16.2
1250	124.5	43.3	10.9
1310	123.5	43.5	10.6
1330	118.0	45.3	6.4
1350	111.5	41.8	7.0
1420	102.0	39.2	5.5

*From Table 20.

**From Equation (8) with G=.9.

Table 29. Predicted Performance for the Acrylic Tube Receiver Tested with a Horizontal Concentrator

Solar Time	$\dot{Q}_{in}$* (Btu/min)	L_q** (Btu/min)	$\dot{Q}_{out}$*** (Btu/min)
1115	111.5	22.9	28.2
1205	112.0	16.2	35.1
1250	111.5	10.9	40.2
1310	111.0	10.6	40.3
1330	109.0	6.4	43.6
1350	105.0	7.0	41.1
1420	98.0	5.5	39.5

*From procedure of Appendix B.
**From Table 28.
***From equation (10).

Table 30. Predicted Performance for the Acrylic Tube Receiver, Same Conditions as Tilted Concentrator Tests

Solar Time	$\dot{Q}_{in}$* (Btu/min)	L_q* (Btu/min)	$\dot{Q}_{out}$** (Btu/min)
1115	124.5	22.9	34.1
1205	126.0	16.2	41.4
1250	124.5	10.9	46.1
1310	123.5	10.6	45.9
1330	118.0	6.4	47.6
1350	111.5	7.0	44.0
1420	102.0	5.5	41.1

*From Table 28.
**Calculated by equation (10) with geometric ratio equal to .94.

Table 31. Predicted Performance of the Experimental Concentrator Receiver Systems for Solar Noon on the 21st of February

Configuration	$T_o - T_a$	$\dot{Q}_{in}$ (Btu/min)	$\alpha\tau_r$ *	L_q (Btu/min)	$\dot{Q}_{out}$ (Btu/min)	η_T **
Bare Pipe	10	106	.95	4.0	61.5	58.0
	100	106	.95	40.0	25.5	24.0
Shrouded Pipe	10	106	.95	3.3	62.2	58.6
	100	106	.95	33.0	32.5	30.6
Shrouded Pipe with one Layer of Tedlar	10	106	.75	1.6	50.0	47.1
	100	106	.75	16.3	35.3	33.3
Shrouded Pipe with two Layers of Tedlar	10	106	.62	1.1	41.7	39.4
	100	106	.62	10.8	32.0	30.2
Acrylic Tube	10	106	.75	1.6	50.0	47.1
	100	106	.75	15.8	35.8	33.8

*From Table 4.

**From equation (5).

Table 32. Predicted Thermal Output of the Acrylic Tube Receiver at Various Hours on the 21st of February

Solar Time	$\dot{Q}_{in}$ (Btu/min)	$T_o - T_a$ (°F)	L_q (Btu/min)	$\dot{Q}_{out}$ (Btu/min)
12	104.0	10.0	1.6	49.0
12	104.0	100.0	15.8	34.8
11-1	100.0	10.0	1.6	47.1
11-1	100.0	100.0	15.8	32.9
10-2	84.5	10.0	1.6	39.6
10-2	84.5	100.0	15.8	25.4
9-3	61.4	10.0	1.6	28.3
9-3	61.4	100.0	15.8	14.1

Table 33. Predicted Performance of the Shrouded Pipe and Acrylic Tube Receivers for a Concentrator Having a Primary Surface Reflectivity of .85

Configuration	$T_o - T_a$	$\dot{Q}_{in}$ (Btu/min)	O_r	R	L_q	$\dot{Q}_{out}$	η_T **
Shrouded Pipe	10	106	.95	.85	4.0	82.3	77.6
Shrouded Pipe	100	106	.95	.85	40.0	52.6	49.7
Acrylic Tube	10	106	.75	.85	1.6	66.0	62.3
Acrylic Tube	100	106	.75	.85	15.8	51.8	49.0

BIBLIOGRAPHY

1. National Academy of Sciences, National Research Council, Committee on Resources and Man, Resources and Man, San Francisco: W. H. Freeman and Company, 1969, p. 158.

2. National Science Foundation and National Aeronautics and Space Administration, Solar Energy Panel, "An Assessment of Solar Energy as a National Resource," N73-26818, December, 1972.

3. S. G. Talbert, J. A. Eibling, G. O. F. Lof, C. M. Wong and E. N. Sieder, "Manual on Solar Distillation of Saline Water," U. S. Department of the Interior, Research and Development Progress Report Number 546, April, 1970.

4. M. J. O'Neill, A. J. McDonald and L. H. Sims, "The Development of a Residential Heating and Cooling System Using NASA Derived Technology," N-73-17911, November, 1972.

5. R. K. Swartman and C. Swaminathan, "Solar Powered Refrigeration," Mechanical Engineering, Vol. 93, No. 6, June, 1971, pp. 22-24.

6. E. B. Penrod and K. V. Prasanna, "Procedure for Designing Solar Earth Heat Pumps," Heating, Piping, and Air Conditioning, Vol. 41, No. 6, June, 1969, pp. 97-100.

7. W. I. Berks and W. Luft, "Photovoltaic Solar Arrays for Communications Satellites," Proceedings of the IEEE, Vol. 59, No. 2, February, 1971, pp. 263-271.

8. P. A. Berman, "Design of Solar Cells for Terrestrial Use," Solar Energy, Vol. 11, July, 1967, pp. 180-185.

9. P. E. Glaser, "Power Without Pollution," Journal of Microwave Power, Vol. 5, No. 4, December, 1970, pp. 211-222.

10. F. Trombe, "Solar Furnaces and Their Applications," Solar Energy, Vol. 1, April, 1957, pp. 9-15.

11. H. Walton, "Amazing No-Fuel Space Engine You Can Build Yourself," Popular Science, July, 1965, pp. 107-110.

12. A. F. Hildebrandt, G. M. Hass, W. R. Jenkins, and J. P. Colaco, "Large Scale Concentration and Conversion of Solar Energy," Transactions of the American Geophysical Union, Vol. 53, July, 1972, pp. 684-692.

13. 'Energy From the Sun," Scientific American, Vol. 55, April, 1936, p. 195.

14. J. I. Yellott, "Power from the Sun," ASME Transactions, Vol. 79, No. 6, August, 1957, p. 1349.

15. G. Francia, "Pilot Plants of Solar Steam Generating Stations," Solar Energy, Vol. 12, pp. 51-64.

16. W. Szulmayer, "Solar Strip Concentrator," Solar Energy, Vol. 14, No. 3, February, 1973, pp. 327-335.

17. C. Guntner, "The Utilization of Solar Heat for Industrial Purposes by Means of a New Plane Mirror Reflector," Scientific American, Supplement number 1586, May 26, 1906, pp. 25409-25412.

18. C. McCrary, "The Design and Construction of Three Receivers for a Solar Energy Concentrator," Report on a Senior Special Problem Course, School of Mechanical Engineering, Georgia Institute of Technology, March, 1974.

19. H. P. Garg, " Measurement of Absorptivity of Black Paints," Journal, Institute of Engineers, (India), Chemical Engineering Division, Vol. 51, No. 2, Pt. C4, October, 1970, pp. 15-17.

20. Thermophysical Properties Research Center (TPRC), Purdue University, Thermophysical Properties of Matter, IFI/PLENUM, New York, Washington, 1970, Vol. 7, pp. 1287-1289.

21. E. W. Spisz, A. J. Weigand, R. L. Bowman, and J. R. Jack, "Solar Absorptances and Spectral Reflectances of Twelve Metals for Temperatures Ranging from 300 to 500°K," NASA Technical Note: NASA TN D 5353, N69-31895, August, 1969.

22. G. G. Gubareff, J. E. Janssen, and R. H. Torborg, Honeywell Research Center, Thermal Radiation Properties Survey, Minneapolis-Honeywell Regulator Company, Minneapolis, Minnesota, 1960, p. 256.

23. Cadillac Plastic and Chemical Company, "The Creative Approach to Cast Acrylics," Detroit, Michigan, 1973.

24. E. I. Dupont De Nemours and Company, Inc., Special Market Division, Films Department, "Optical Properties," Technical Information Bulletin, No. TD-5, Wilmington, Deleware, 1971.

25. P. Van De Kamp, Principles of Astronomy, San Francisco, W. H. Freeman Company, 1967.

26. American Society of Heating, Refrigerating, and Air Conditioning Engineers (ASHRAE), Handbook of Fundamentals, New York, ASHRAE, Inc., 1972.

27. J. Russel, Jr., "Investigation of a Central Station Solar Power Plant," Preprint of a paper presented at the Solar Thermal Workshop of January, 1973, Washington, D. C.

28. J. L. Threlkeld and R. C. Jordan, "Direct Solar Radiation Available on Clear Days," Transactions of the American Society of Heating and Air Conditioning Engineers, Vol. 64, 1958, pp. 45-68.

29. P. Moon, "Proposed Standard Solar Radiation Curves for Engineering Use," Journal of the Franklin Institute, Vol. 230, November, 1940, pp. 583-617.

30. F. S. Johnson, "The Solar Constant," Journal of Meteorology, Vol. 11, December, 1954, pp. 431-439.

31. W. J. Humphreys, Physics of the Air, McGraw-Hill Publishing Company, New York, 1940, pp. 89-97.

32. S. T. Henderson, Daylight, American Elsevier Publishing Company, New York, 1970, p. 36.

33. S. Fritz, "Solar Energy on Clear and Cloudy Days," The Scientific Monthly, Vol. 84, February, 1957, pp. 55-56.

34. I. F. Hand, "Review of United States Weather Bureau Solar Radiation Investigations," Monthly Weather Review, Vol. 65, December, 1937, pp. 434-441.

35. U. S. Department of Commerce, Weather Bureau, Climatological Data--National Summary, Vols. 5-12, 1958-1961.

36. U. S. Department of Health, Education and Welfare, Public Health Service, Division of Air Pollution, Air Pollution Measurements of the National Air Sampling Network, Washington, D. C., 1962.

37. A. C. Stern, "Changes in Indentity and Quality of Pollutants, Past, Present, and Future," Proceedings, National Conference on Air Pollution, Washington, D. C., U. S. Department of Health, Education, and Welfare, Public Health Service, 1958, p. 92.

38. Fulton County Health Department, Office of Air Pollution Control, Atlanta, Georgia.

39. U. S. Department of Commerce, Weather Bureau, "Mean Precipitable Water in the United States," Technical Paper Number 10, Washington, D. C., 1949, p. 8.

40. S. Fritz, "Solar Radiation During Cloudless Days," Heating and Ventilating, Vol. 46, January, 1949, pp. 67-74.

41. A. Olgyay, Solar Control and Shading Devices, Princeton University Press, 1957, p. 36.

42. F. Kreith, Principles of Heat Transfer, Third Edition, New York, Intext Educational Publishers, 1973.

43. M. Jakob, Heat Transfer, Vol. I, New York, John Wiley and Son, Inc., 1949, pp. 539-542.

44. S. Dushman, Scientific Foundations of Vacuum Technique, New York, John Wiley and Sons, Second Edition, 1962.

45. G. B. Wilkes, Heat Insulation, New York, John Wiley and Sons, 1950, pp. 94-98.

46. E. Sprayer, "Solar Energy Collection with Evacuated Tubes," ASME Transactions, Journal of Engineering for Power, Vol. 87, No. 3, July, 1965, pp. 270-276.